POLYTECHNIC OF TURIN

Faculty of Engineering
Master's Degree in Aerospace Engineering

Master Thesis

Structural Modelling and Aeroelastic Analysis of the DANAERO Wind Turbine Rotor

Advisors:
Prof. Erasmo Carrera
M.Sc. Giorgia Guma

Candidate:
Simone Ferrari

October 2019

Acknowledgement

First of all I would like to thank Professor Erasmo Carrera and the PhD student of the University of Stuttgart Giorgia Guma for giving me the opportunity to do this master thesis during my Erasmus program in Germany.
In the course of this 5 months in Stuttgart I was able to expand my knowledge and my interests mainly thanks to people available to follow me and to be careful towards my work.
A special thanks to my parents for the unconditional support they gave me during my university years (and not only) and to my family for affection and constant closeness.
I thank my friends and university colleagues for having contributed in their way to achieving this goal.
Finally a heartfelt thanks to my significant other for having supported me in the difficult moments of this journey and for sharing with me the joys of life.

Summary

The objective of this thesis is to carry out an aeroelastic analysis of the DANAERO wind turbine within a new project called MEXNEXT that aims to achieve greater accuracy and precision in simulation methods.
To achieve this goal it was initially necessary to retrace the history of the wind energy, understanding the trend of bigger wind turbines and to understand which tools are currently available for the aeroelastic analysis and how they can be improved.
A first conclusion based on the theoretical study was that of being able to improve the coupling between structural response and aerodynamic loads by using a CFD code (FLOWer [70]) instead of the BEM method.
Regarding the structural component of the simulation was decided to represents the wind turbine through a 1D FEM model by using an open source code named KRATOS MULTIPHYSICS [52] whose utilization and reliability represent an additional object of evaluation within this thesis.
Once the tools to be used were defined, the analysis of structural and geometrical data of the wind turbine obtained from the project have been performed and the conclusion was that for the generation of the FEM model a more appropriate and accurate study of the received information is necessary.
In the next step the FEM code (Kratos [52]) has been validated by comparing its results with the analytical one whereupon the frequencies of the tower and of the blade were calculated through various combinations of meshes and structural properties with the aim of identifying which combination came close to the data provided by the project.
At this point it was necessary to create or modify the CFD model of the wind turbine.
The choice was to make first the aeroelastic simulation of the tower in order to approach the coupling between the codes with a simple case.
The mesh of the tower was generated with POINTWISE [68] and, once the unsteady CFD simulation was brought to convergence, the aerodynamic loads acting on it were analysed and the consequent deformations were evaluated using the corresponding FEM model (ONE WAY COUPLING).
The next step was the aeroelastic analysis of the wind turbine that was carried out considering two different and already developed models.
The first one is a 1/3 rotor model that considers a single blade (120 ° model) while the second one is a complete and full rotor model (rotor, nacelle, tower).
For both of them the unsteady CFD simulations were performed and the resulting aerodynamic loads were applied to the FEM model to evaluate and compare the deformations (ONE WAY COUPLING).

The second and more complex phase consists of a TWO WAY COUPLING study on the 1/3 model in which the CFD and FEM code exchange forces and deformations iteratively at every TIMESTEP until they reach a stable and stationary aerodynamic and structural solution.
Subsequently various analyses and numerous comparisons were conducted over the obtained results in terms of forces and displacements.
Furthermore, the aeroelastic stability of the turbine was investigated through a comparison between the frequencies of the exciting forces acting on the blade and the natural frequencies of the structure.
Finally, the power generation of the turbine under various working conditions was calculated.

Sommario

L'obiettivo di questa tesi è svolgere un'analisi aeroelastica della turbina eolica del progetto DANAERO all'interno di un nuovo progetto chiamato MEXNEXT che si prefigge come obiettivi una maggiore accuratezza e precisione nei metodi di simulazione.
Per raggiungere tale obiettivo è stato inizialmente necessario ripercorrere la storia dell'energia eolica, comprendere il trend di pale eoliche di dimensioni sempre maggiori e capire quali strumenti sono attualmente disponibili per effettuare analisi aeroelastiche e come possono essere migliorati.
Una prima conclusione basata sullo studio teorico è stata quella di poter migliorare l'accoppiamento tra risposta strutturale e carichi aerodinamici utilizzando un codice CFD (FLOWer [70]) al posto del metodo BEM.
Per quanto riguarda la componente strutturale della simulazione si è deciso di modellizzare la turbina eolica come FEM 1D attraverso un codice open source di nome KRATOS MULTIPHYSICS [52] il cui impiego e la cui affidabilità costituiscono un ulteriore oggetto di valutazione all'interno di questa tesi.
Una volta definiti gli strumenti che si andranno ad utilizzare, si sono analizzati i dati strutturali e geometrici della turbina eolica ottenuti dal progetto concludendo che per la generazione del modello FEM è necessaria una più approfondita analisi delle informazioni.
Una volta validato il codice FEM (Kratos [52]) confrontando i suoi risultati con risultati analitici, si sono calcolate le frequenze proprie della torre e della pala attraverso varie combinazioni di mesh e proprietà strutturali al fine di indentificare quale più si avvicinasse ai dati forniti dal progetto.
Arrivati a questo punto è stato necessario creare parte del modello CFD della turbina eolica.
La scelta è stata quella di effettuare come prima simulazione un'analisi aeroelastica della sola torre di modo da prendere confidenza con i software per un caso semplice.
La mesh della torre è stata generata con POINTWISE [68] e, una volta portata a convergenza la simulazione CFD instazionaria, si sono analizzati i carichi aerodinamici agenti su di essa e le conseguenti deformazioni tramite il modello FEM (ONE WAY COUPLING).
Il passo successivo è stato l'analisi aeroelastica della turbina eolica che è stata svolta considerando due modelli differenti già sviluppati.
Il primo è un modello ad 1/3 del rotore che considera una sola pala (modello a 120°) mentre il secondo è un modello completo (rotore, navicella, torre).

Per entrambi si sono svolte le simulazioni CFD instazionarie e si sono applicati i carichi risultanti al modello FEM per valutare e comparare le deformazioni (ONE WAY COUPLING).
La seconda e più complessa fase è stata svolta effettuando uno studio aeroelastico TWO WAY COUPLING sul modello a 1/3 in cui iterativamente il codice CFD e FEM si sono scambiati forze e deformazioni ad ogni TIMESTEP fino a raggiungere una soluzione aerodinamica e strutturale stabile e stazionaria.
In seguito sono state condotte varie analisi e numerosi confronti tra i vari risultati ottenuti in termini di forze e spostamenti.
Inoltre la stabilità aeroelastica della turbina è stata analizzata attraverso un confronto tra le frequenze delle forze eccitanti la struttura e le frequenze proprie di quest'ultima.
Infine è stata calcolata la generazione di potenza della turbina nelle varie condizioni di utilizzo e per le diverse configurazioni simulate.

Contents

List of Figures

List of Tables

Chapter 1

Introduction

1.1 Wind Energy

Renewable energy resources such as wind and solar have received great attention in recent years due to the depletion of fossil fuel resources and the growing demand for energy consumption.
Most renewable energy resources (such as wind and solar) are inexhaustible and environmentally friendly compared to fossil fuel resources.
Among them, wind power is the most promising resource for renewable energy and can provide a competitive solution to the global climate change and energy crisis.
For the previous reasons, wind energy is one of the technologies with the highest amount of investments and the next dashboard provides an overview about that.

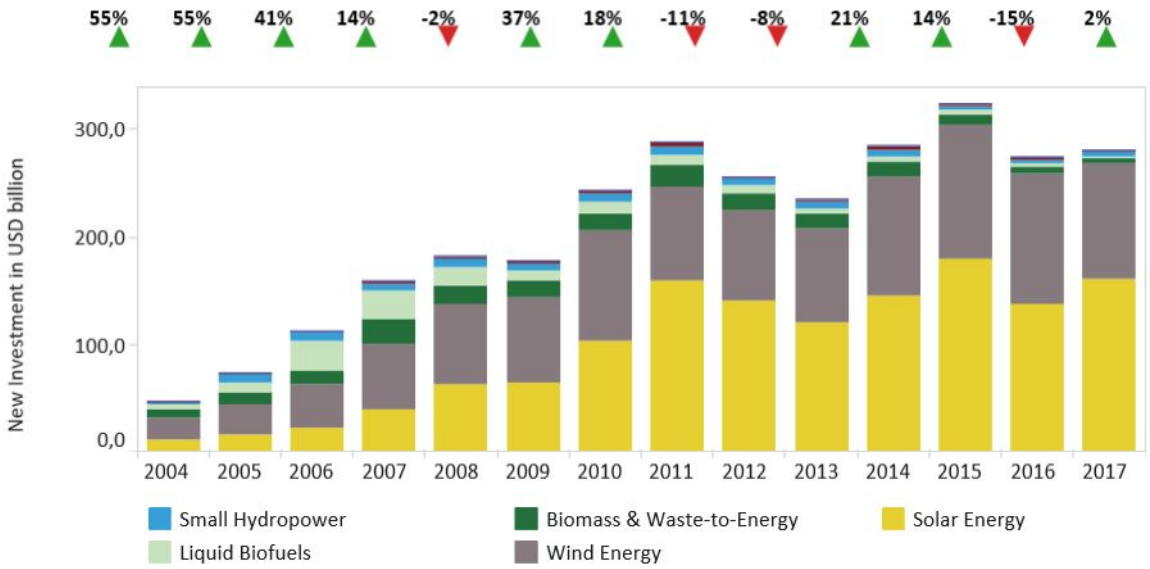

Figure 1.1: Global Trends in Renewable Energy Investments [1]

Wind power is currently one of the fastest growing renewable energy industries and from FIGURE 1.2 we can see that the cumulative capacity of global wind power has dramatically increased over the past decades.

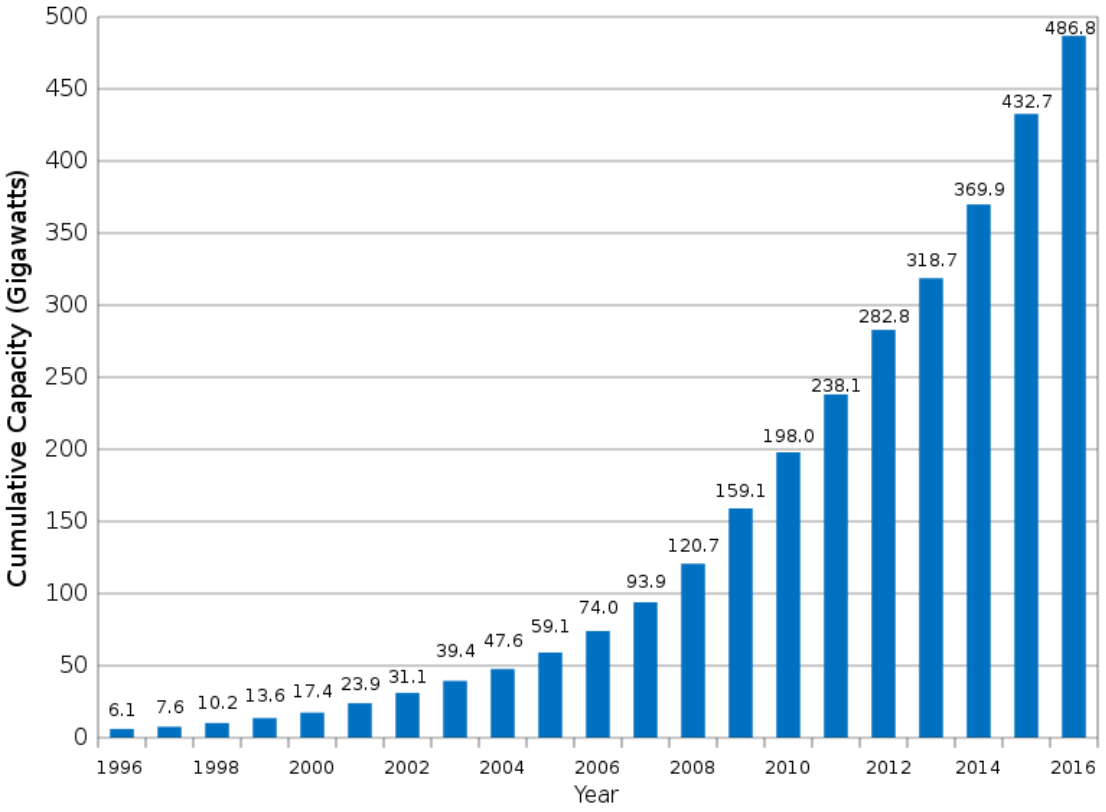

Figure 1.2: Global wind power cumulative installed capacity in gigawatts [2]

Wind power technology itself has also moved rapidly towards new dimensions with the increase in wind power capacity due to the size of wind turbines getting larger and larger.
This increment in the size of the rotor is possible due to the higher altitudes necessary to catch the wind as faster as possible.
Another important reason for wind turbine size growth is the offshore location of wind turbines at sea where there is more space available and of course the wind is steadier and stronger.
Another considerable effect of increasing the size of wind turbines is that the maintenance cost for offshore located devices is lower than for more but smaller wind turbines.

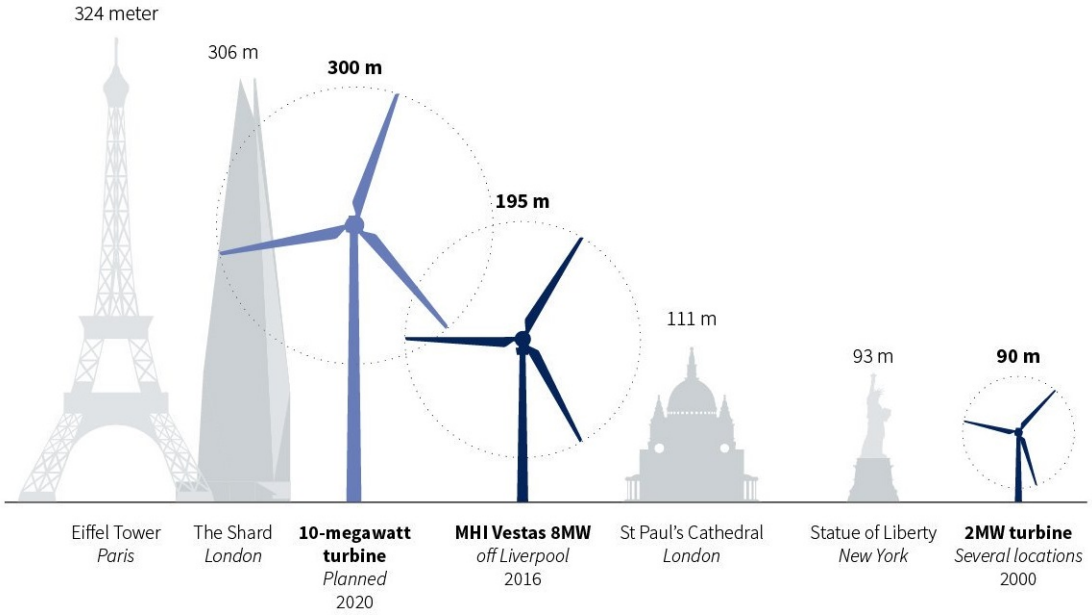

Figure 1.3: Wind turbines size development [3]

Increasing the size of wind turbines does not only cut the maintenance costs but lowers the cost of wind power per kWh and makes this energy resource more competitive on the market.

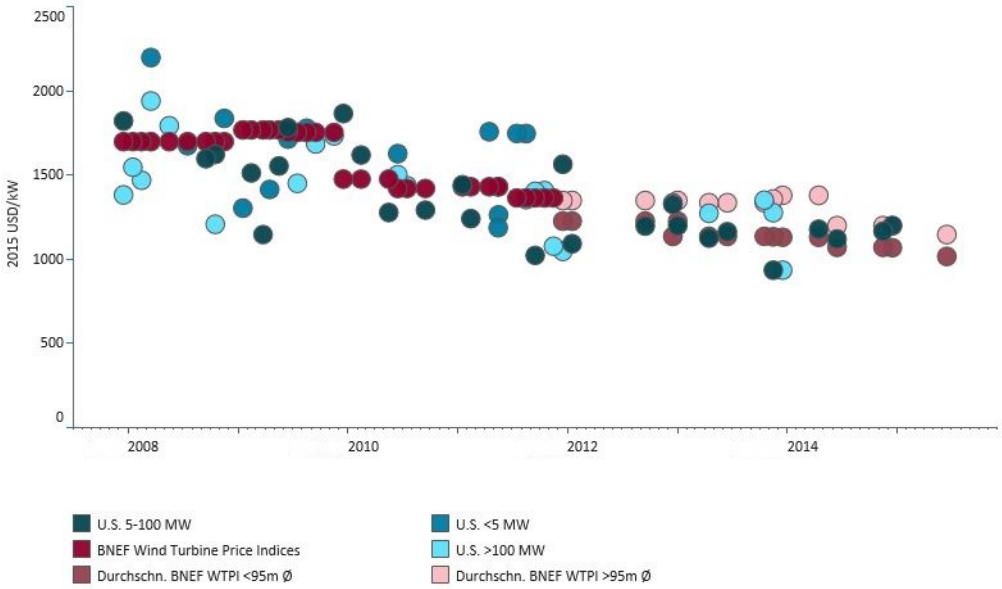

Figure 1.4: Wind turbine prices [4]

The last point I would like to introduce is that the increasing size in wind rotor has benefits from the economic and efficiency point of view but the trend to upscaling wind turbine results in larger, slender and flexible blades which could lead to aerodynamic instabilities as we will see in the next sections.

1.2 MEXNEXT Project

The International Energy Agency Wind Technology Collaboration Program (IEA Wind TCP) is an international collaboration that shares information and research activities to promote development and deployment of wind energy in member countries.
The IEA Wind TCP has been developing and deploying wind energy technology through vigorous national programs and international cooperative efforts since its founding in 1977.
Participants exchange the latest information about their current and future activities and participate in selected research tasks for IEA Wind TCP [5].
The IEA Wind Task MEXNEX(T) can be considered the successor of IEA Wind Task XX and is a joint project in which 20 parties from 11 different countries cooperate.
Mexnext's 1st phase (Mexnext-I) ran from 1 June 2008 to the end of 2011 for 3 year and its main objective was to analyse measurements from the MEXICO project in order to validate computational codes not only in terms of loads but also in terms of underlying flow field.
In this MEXICO project, 9 European institutes conducted a wind tunnel experiment on a rotor with a diameter of 4.5 m in the Large Low Speed Facility (LLF) of the German Dutch Wind Facilities DNW [6].

Figure 1.5: Wind Tunnel measurements of the EU project MEXICO

In addition, a second set of measurements on the Mexico rotor in the same facility was performed in Mexnext-II and these so-called ' New Mexico ' measurements were found to be even more useful than the first database, leading to the third phase of Mexnext running from 1 January 2015 to 31 December [5].
The main impact of the Mexnext-III project is the insights offered in the accuracy of design models that allow for a more thorough evaluation of design calculations with reduced uncertaintes [7].

This thesis is involved in the fourth phase of Task 29 that started on January 1, 2018 and will end on December 31, 2020.
Although the basic goal of Phase IV appears similar to the goal of the previous phases at first sight, i.e. improvement of aerodynamic models for wind turbine design codes, the goal is now achieved through full-scale field measurements from the Danish Danaero experiment on a 2MW turbine [5].
The fourth phase focuses on aeroelastic and turbulent inflow effects as we will discuss in detail later.

Figure 1.6: NM 80 turbine at Tjæreborg Enge

1.3 Wind Turbine Aeroelasticity

Aeroelasticity is the study of the interaction of aerodynamic, inertial, and elastic forces and can be clearly illustrated by the Collar aeroelastic triangle as shown in Fig. 1.7.

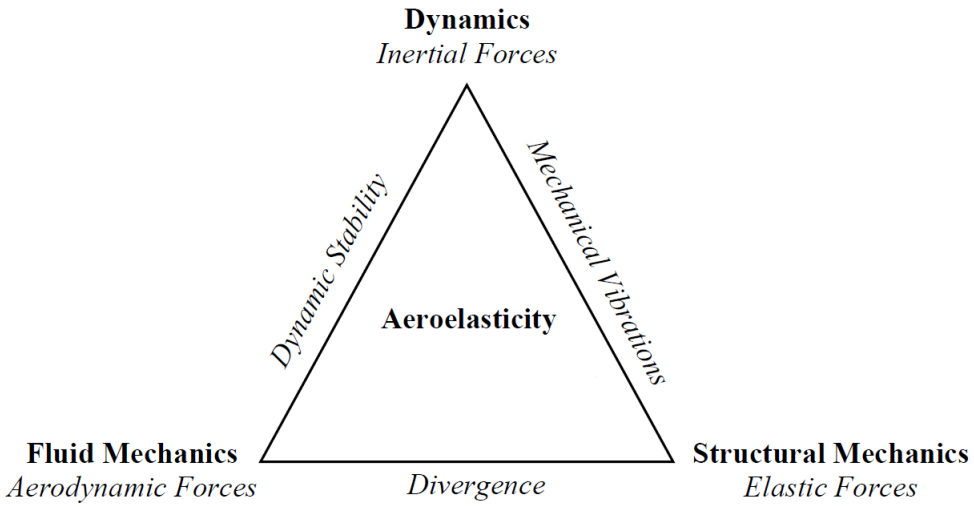

Figure 1.7: Collar aeroelastic triangle

Consider air passing over a wind rotor where the aerodynamic force on the blade causes a small elastic deformation that changes the blade's orientation in the air stream, which changes the aerodynamic force on the blade in turn.
Inertia dynamics play a major role in the correlation of aerodynamic loads and elastic deflections with the resulting accelerations.
This interactions either reach a new state of equilibrium or catastrophically diverge resulting in structural failure.
Wind turbine designers use aeroelastic analyses to maximize the damping of the system components and keeping the modal frequencies of the system components separated in order to damp vibrations and to ensure safe structure with minimized fatigue loads [8].
It is possible to classify aeroelasticity phenomena into static or dynamic problems.

1.3.1 Steady Aeroelasticity

The study of steady aeroelasticity mainly focuses on the divergence, which occurs when the torsional moment introduced by aerodynamic loads is higher than the restoring moments due to structural stiffness [9].
We can examine the steady aeroelasticity through a divergence analysis with 1 DOF. Let us consider a generic airfoil having a torsional spring placed at the shear centre and for which c is the chord, x_{ac} is the aerodynamic centre, U is the free stream velocity, α is the angle of attack, C_{L_α} is the lift coefficient, G is the shear modulus of the considered material and k is the stiffness of the spring.

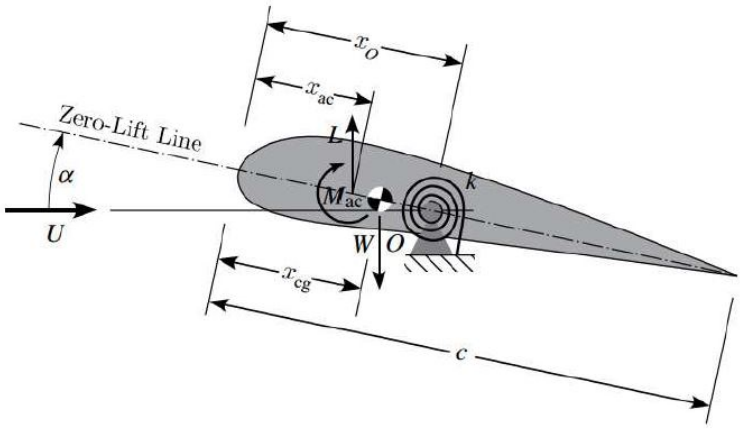

Figure 1.8: Airfoil with 1 DOF [10]

In order to get the divergence velocity, we first write the momentum equilibrium equation around the spring axis:

$$M_{ac} + L(x_0 - x_{ac}) - W(x_0 - x_{cg}) - k\theta = 0 \tag{1.1}$$

We can define:

$$L = q_\infty S C_{L_\alpha}(\alpha_R + \theta) \tag{1.2}$$

$$M_{ac} = q_\infty S c C_{M_{ac}} \tag{1.3}$$

and by substituting equation (1.2) and (1.3) into (1.1) we get:

$$\theta = \frac{q_\infty S c C_{M_{ac}} + q_\infty S C_{L_\alpha} \alpha_R (x_0 - x_{ac}) - W(x_0 - x_{cg})}{k - q_\infty S C_{L_\alpha}(x_0 - x_{ac})} \tag{1.4}$$

We have divergence when the torsional angle θ tends to ∞ and this is true when the denominator is equal to 0 and we get:

$$q_\infty = q_D = \frac{k}{S C_{L_\alpha}(x_0 - x_{ac})} \tag{1.5}$$

k is the torsional stiffness of the spring that can be calculated from the geometrical and material properties of the wing as follows:

$$k = \frac{GJ}{L} \tag{1.6}$$

The divergence velocity is then:

$$V_D = \sqrt{\frac{2q_D}{\rho_\infty}} \tag{1.7}$$

We found out that there is a divergence velocity for a general wing.
Aircraft wings have experienced divergence in the past, but the divergence phenomenon has not been observed for commercial wind turbines and is unlikely to occur in the future.
This is mainly due to the fact that the torsional moments on wind turbine blades are generally small and not high enough for the onset of divergence even when the blade is pitching [11] .
In the static aeroelasticity analysis of wind turbine blades, aeroelastic models are mainly used to calculate the steady-state blade tip deflection in order to determine the blade tip clearance. The wind turbine's blade tip clearance is a critical operating parameter necessary to prevent a catastrophic failure caused by the blade striking the tower and is therefore necessary to have a reliable aeroelastic model.

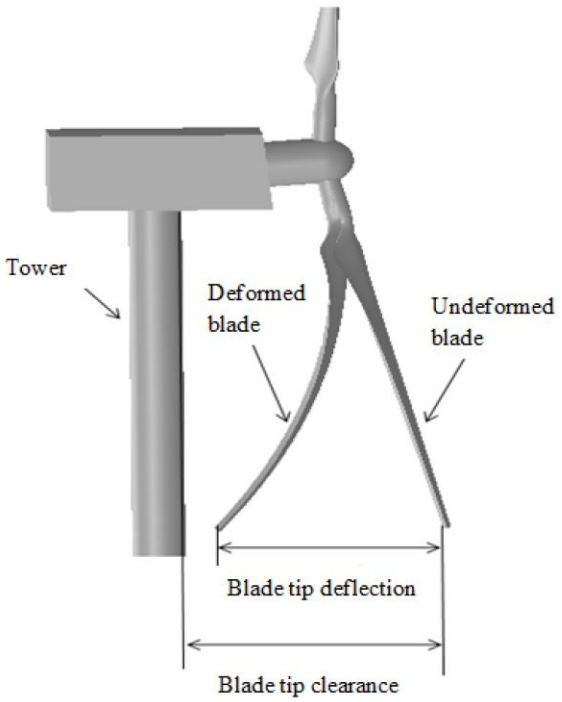

Figure 1.9: Blade tip deflection and clearance [11]

1.3.2 Dynamic Aeroelasticity

In this section we are going to study the oscillatory effects of aeroelastic interactions and the wind turbine blade aeroelastic instabilities such as flapwise and edgewise instability, flutter instability and coupled rotor/tower instabilities.
Let's first introduce the degrees of freedom(DOF) associated with the wind turbine.

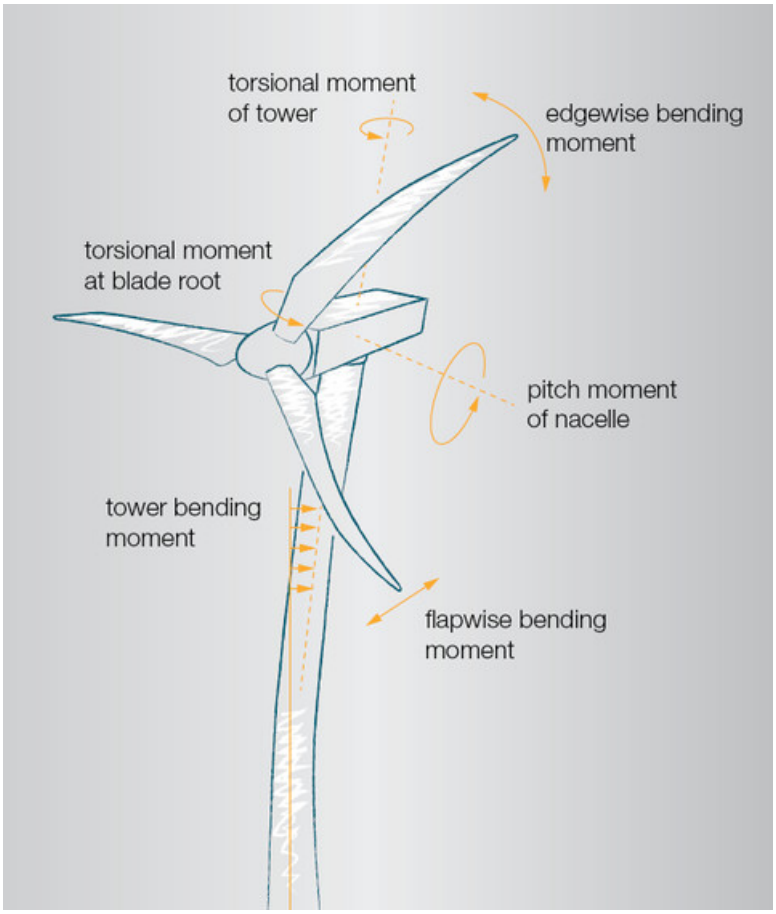

Figure 1.10: Degrees of freedom of a wind turbine [12]

1.3.3 Flapwise and edgewise instability

In modern wind turbine the flapwise motion has a positive dumping and then this degree of freedom doesn't suffer of instability except at very high wind speeds as showed by the analysis of Petersen [13].
On the other side there is a relatively smaller, even negative aerodynamic damping for edgewise modes and therefore is considered the most important instability problem for wind turbines [14].
Some commercial wind turbine blades have suffered from blade edgewise instability because of the increasing size of the rotor.
Stiesdal reported edgewise vibrations on a 37 meter diameter rotor in 1994 [15].
The APX40 T blade, which was installed on a 600kW wind turbine with a 37m-diameter rotor, is another example of the blades suffering from this instability problem [16].
As you can see from Fig. 1.11, violent oscillations of the edgewise DOF occur between 35s and 55s and the instability was caused by the first edgewise mode's negative aerodynamic damping.

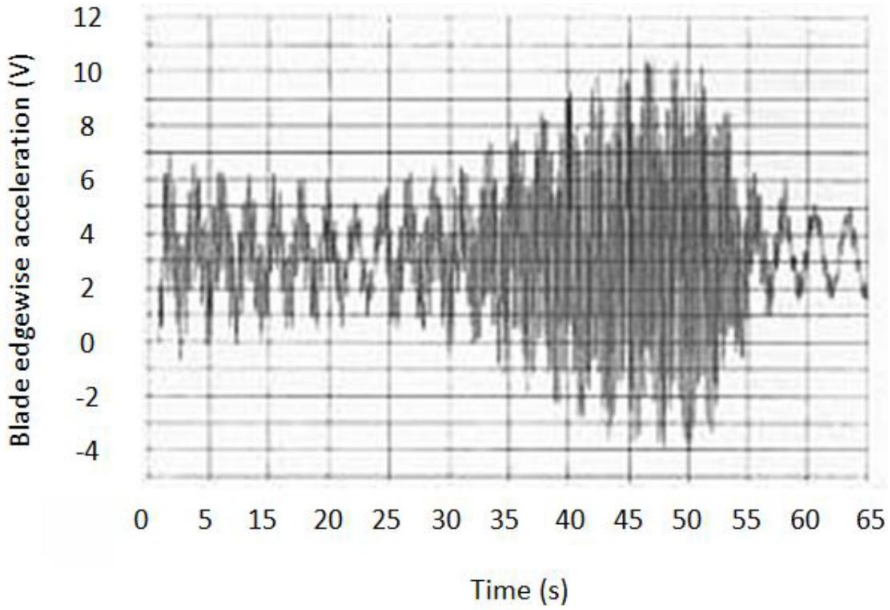

Figure 1.11: APX40T blade oscillations measured at 85% blade span [16]

1.3.4 Flutter

Flutter is an instability two-dimensional vibrational problem where two degrees of freedom (DOFs) coupled together and is a common issue in turbomachinery and fixed-wing aircraft but it has never appeared in commercial wind turbines [17].
Flutter can be classified into the following three types based on the different combinations of any two blade DOFs:

- **flap-pitch flutter** also known as classic flutter is the flap-wise and torsional blade motions coupling and is the most common one
- **lag-pitch flutter** involving edgewise and torsional blade motions coupling
- **flap-lag flutter** that combines flap-wise and edgewise blade movements

Starting from the figure below we can analyse a typical flap-pitch flutter.

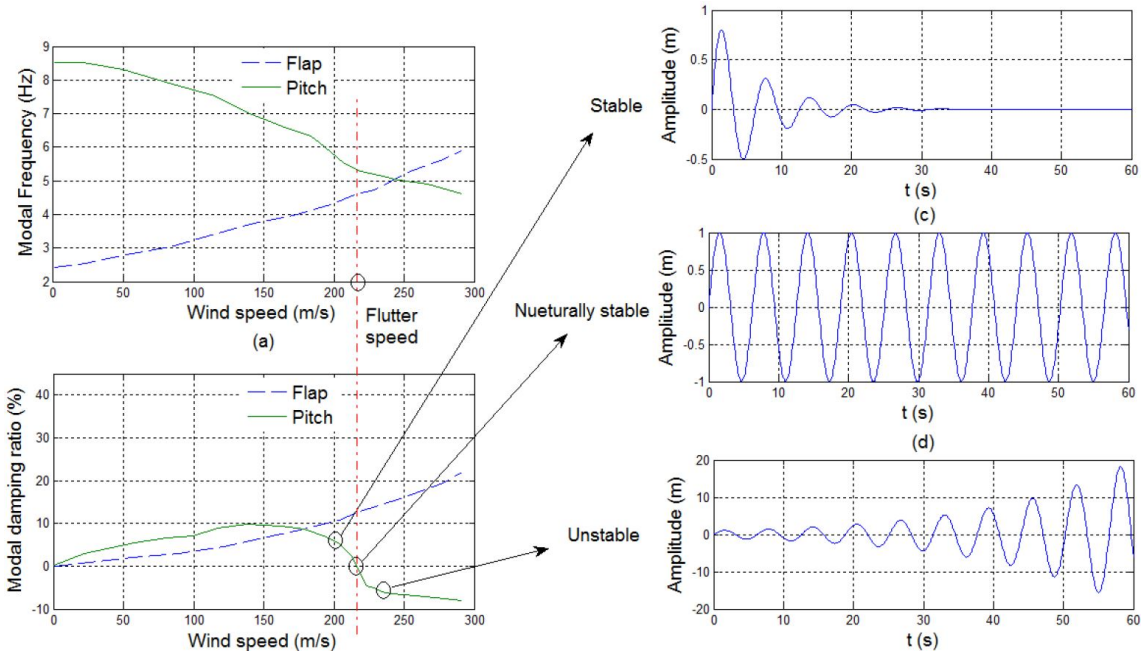

Figure 1.12: Flap-pitch flutter example [11]

As you can see from Fig. 1.12, as air velocity increases, the pitch mode frequency gets closer to the flap mode, resulting in one combined mode at a certain critical wind velocity (flutter velocity).
One of the modes (the pitch mode in this example) usually has zero net damping at flutter speed.
If the wind speed is higher than the flutter speed, the net damping, which is the sum of structural damping and aerodynamic damping, becomes negative and unstable oscillations happen and lead to structural failure.
With larger wind turbines, there is concern that flutter could emerge because the torsional frequency decreases with increased structural flexibility.
For example, Vatne [18] analysed a 10 MW wind turbine of about $140m$ diameter rotor and found out that the flutter speed is near double the max operational speed.

1.3.5 Whirl flutter

It is well known that classic whirl flutter occurs on tilt rotors [19], conventional turboprop aircraft and helicopters.
It is an instability that results in a whirling rotor plane in the combined yaw and tilt direction.
Depending on the direction of this whirling motion in respect to the rotor rotation, this whirl mode is called a forward whirl or backward whirl.
Whirl flutter may start quickly and, as the above mentioned flutter, has a critical velocity above which there will be instability.
At the flutter velocity limit, the aerodynamic and structural damping take out of the system the exact same amount of energy as the yaw moment due to the pitch and pitch moment being put into the system due to yaw.
It was found that this instability is very unlikely to occur on wind turbines, the shaft or tower-top rigidity had to be reduced to such a degree before the instability occurred, that it is unlikely to become an issue with any of the current wind turbines or larger upscaled turbines [20]. However, for wind turbines there is a known instability issue that involves the rotor's whirling motion.
A clear description of the mechanism behind the instability is given by Petersen [21], who found two different types of whirl motion, the so-called local blade whirl and the global rotor whirl.
The local blade whirl is a consequence of the dynamic effects of unsymmetrical edgewise modes of the blades(see Fig.1.13) and the resulting in-plane force due to inertia is not equal to zero.

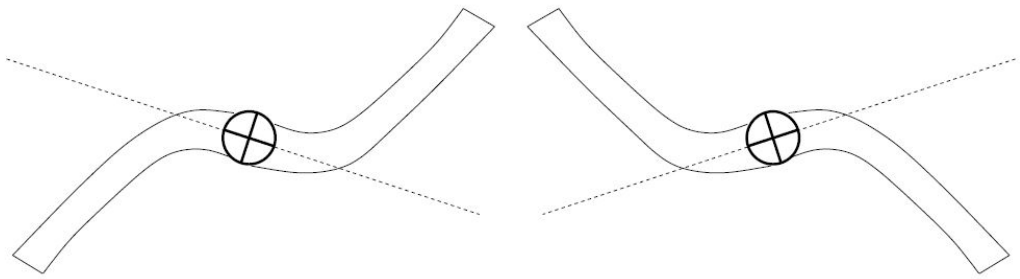

Figure 1.13: Anti-symmetric lead-lag mode for a two bladed turbine

The so-called global rotor whirl modes involves tower, nacelle and shaft and results in a dynamics combination of the tilt and yaw movements, including parts due to the bending flexibility of the shaft.

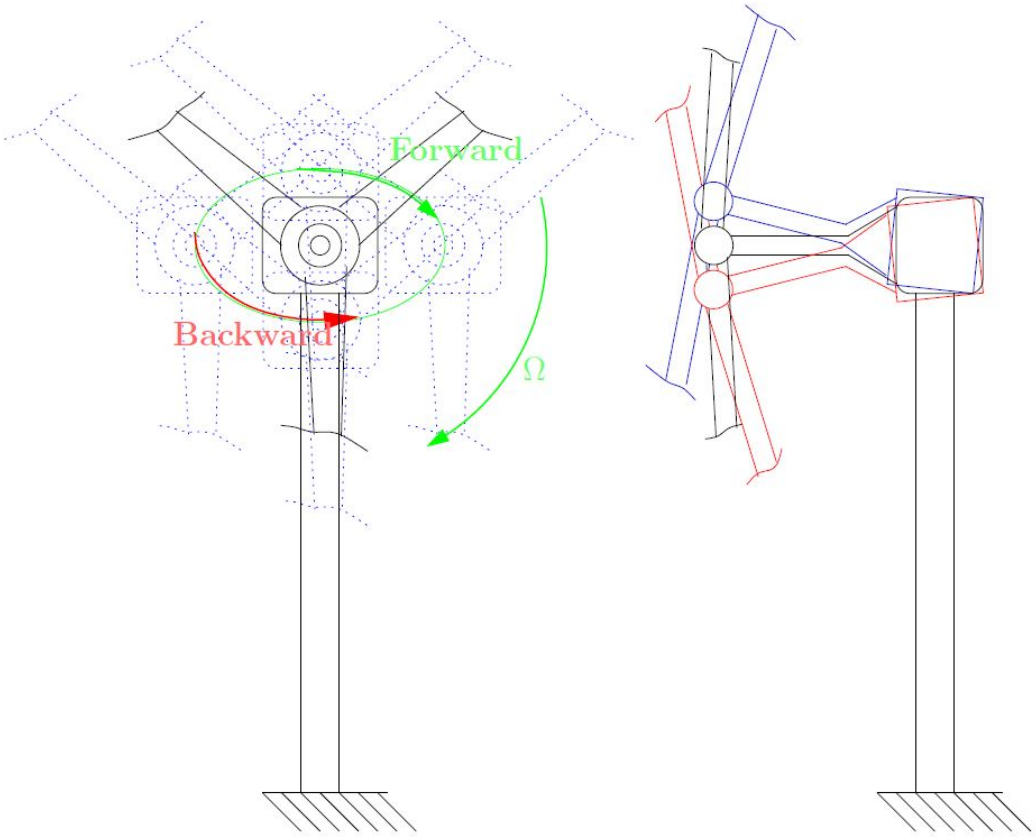

Figure 1.14: Whirl motion of a wind turbine with the rotor centre moving along an ellipse

1.3.6 Coupled rotor/tower instabilities

Aeroelastic analysis of a single turbine blade is typically insufficient as it is possible to couple the vibrations of other system components such as tower or nacelle through the structural connections with blade vibrations.
A famous example of this instability occurred in the 1980s on the KEWT prototype where the first tower torsion mode and lead/lag mode were coupled when the rotor's angular velocity was half the first tower torsion mode frequency [22].
Furthermore a second instability issue happen when the angular velocity was half the frequency of the second tower bending mode [22].

1.4 Aeroelastic models

As described in the previous sections, changes in the design of wind turbine blades due to the growth in size may result in other aeroelastic instabilities that have not yet been recognized and is therefore very important to develop a wind-turbine-specific aeroelastic model.
An aeroelastic model should include an aerodynamic component for calculating aerodynamic loads and a structural component for determining structural dynamic responses.
To better understand the capacity and the characteristics of the state of the art in aeroelastic modelling of wind rotor, a comprehensive review of the aerodynamic and structural components of it has been proposed below.
Let's start the analysis with an overview of the different components of the analysed model.

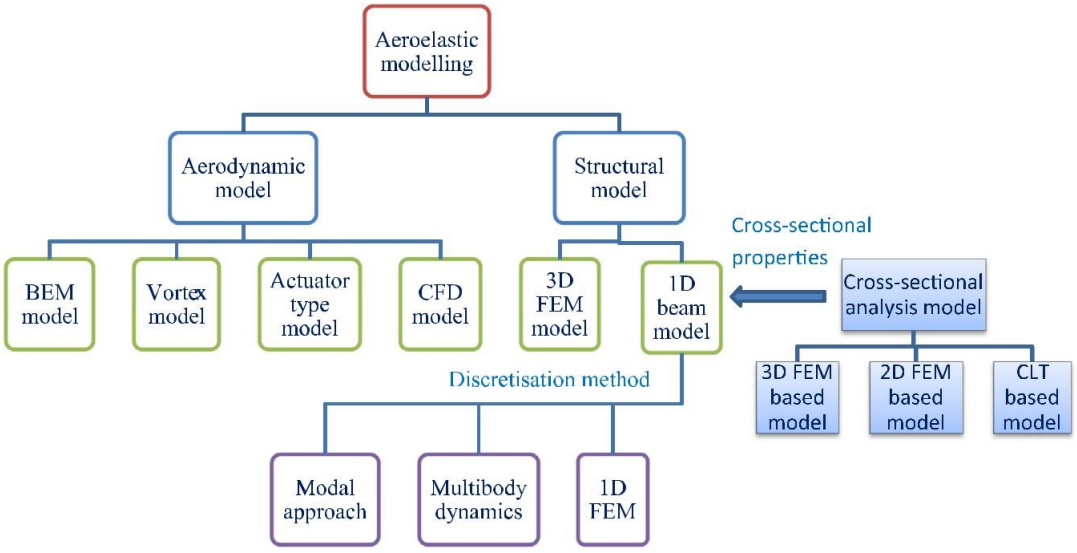

Figure 1.15: . Components of the aeroelastic modelling of wind turbine blades [23]

1.4.1 Aerodynamic models

In the aero-elastic modelling of wind turbine blades, four types of aerodynamic models were used:

- **Blade element momentum theory** combines the "theory of blade elements" in order to calculate local forces on a propeller or wind turbine blade and the "theory of momentum" in order to alleviate some of the difficulties in calculating induced rotor velocities [24].

The blade momentum theory introduces axial induction factor a and angular induction factor a' to respectively calculate the induced velocity in the axial and tangential directions, as shown schematically in Fig. 1.16.
The induced velocity affects the angle of attack of the blade and therefore influences the aerodynamic loads calculated by the above mentioned blade element theory [23].

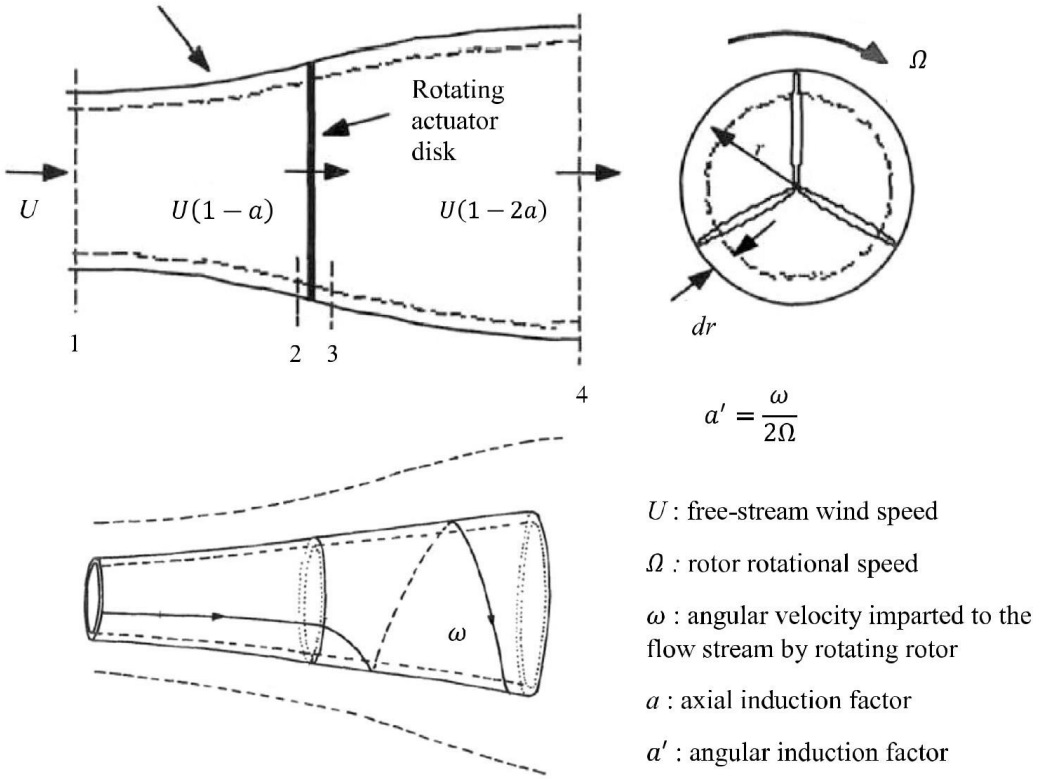

Figure 1.16: Diagram of the blade momentum theory

The classical BEM model has several limitations that are usually found in wind turbine applications but overcome by introducing empirical corrections borrowed from helicopter applications or based on experience with wind turbines. Those limitations are linked to the introduction of a tip loss correction factor, a turbulent wake state correction factor, a dynamic and unsteady inflow model and a dynamic stall model.
The BEM model has been validated with experimental data [25] and is simple, efficient and fast when reliable airfoil aerodynamic data are available.

- **Vortex model** has also found applications in the aeroelastic models of wind turbine blades to better model the wake dynamics of wind turbine rotors.
  For this model, the lifting lines or surfaces represent the trailing and shed vorticity in the wake that can be calculated using either the prescribed wake method or the free wake method.

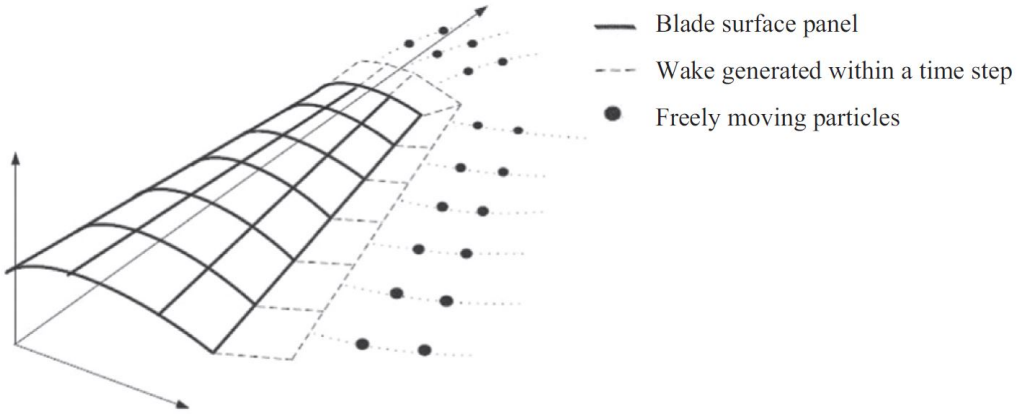

Figure 1.17: Structure of the free-wake modelling of a blade [26]

In the first one, it is assumed that the wake shedding from the blade is rigid and is described using semi-empirical formulations and is computational time savings but at the same time limits its application to steady incoming flow [26].
Otherwise, in the second mentioned method, the wake can be varied freely both in time and space and is therefore applied to wind turbine blades to study the unsteady flow and wakes of blades [27].

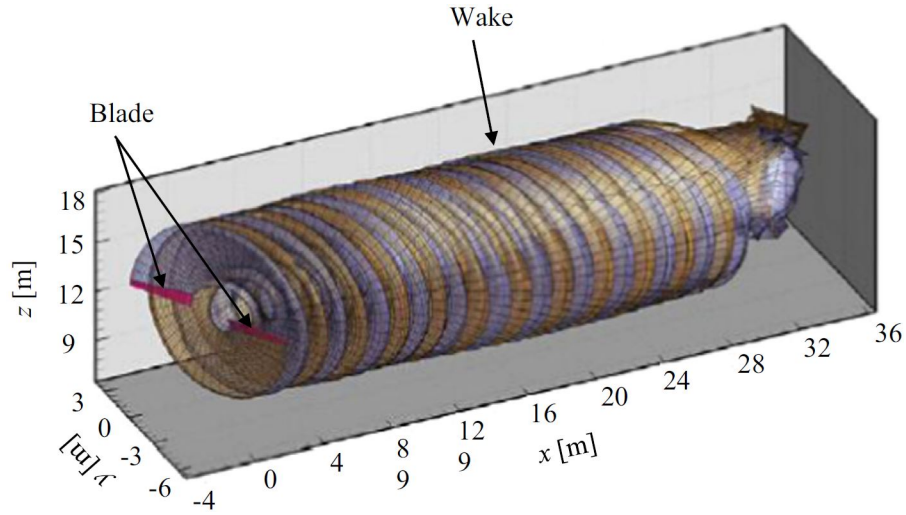

Figure 1.18: Wake of a two-bladed wind turbine rotor using the vortex model [28]

Compared to the BEM model, the vortex model requires more computational resources but its implementation and reliability is limited because viscous effects are ignored and the simulations tends to diverge due to the intrinsic singularities of the vortex panels.

- **Actuator type model** has been developed in various form which can be classified based on the representation of the blade, namely: actuator disc model, actuator line model and actuator surface model.
  The actuator disc model was the first one developed by Rankine [29] and Froude [30]. The before mentioned model is derived from the 1D momentum theory and ended up in the BEM model and in its general form can be numerically combined with the Euler or Navier-Stokes equations.
  Analysing a simple case of a uniformly charged actuator disk, the force acting on the disk is determined by the thrust coefficient and reference wind speed while for a non-uniformly charged actuator disk, the force acting on the disk varies along the radial position but remains constant over the annulus.
  More accurate model have been developed by Sørensen and Shen [31] who extended the non-uniformly loaded actuator disc method to the actuator line approach, in which a line with distributed loads is used to represent the blade forces.

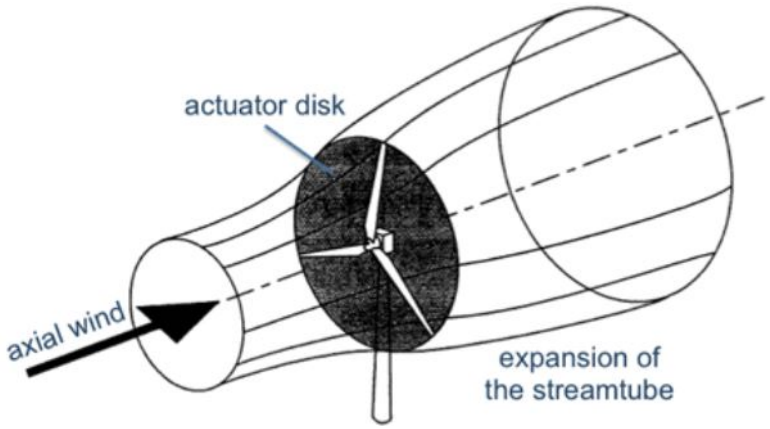

Figure 1.19: Illustration of wind through the actuator disk swept area [32]

In conclusion, the actuator type models discussed above should be credited for a better insight into the 3D and the wake dynamics, but they are more time-consuming (Navier-Stokes equations) and the results are not more accurate than the BEM model.

- **3D CFD model** has received considerable attention in recent years with the advancement of computing resources.
  The CFD method solves the governing fluid flow equations at thousands of positions on and around the rotor blade in an iterative process resulting in aerodynamic loads on the body and allows visualization of the flow field.

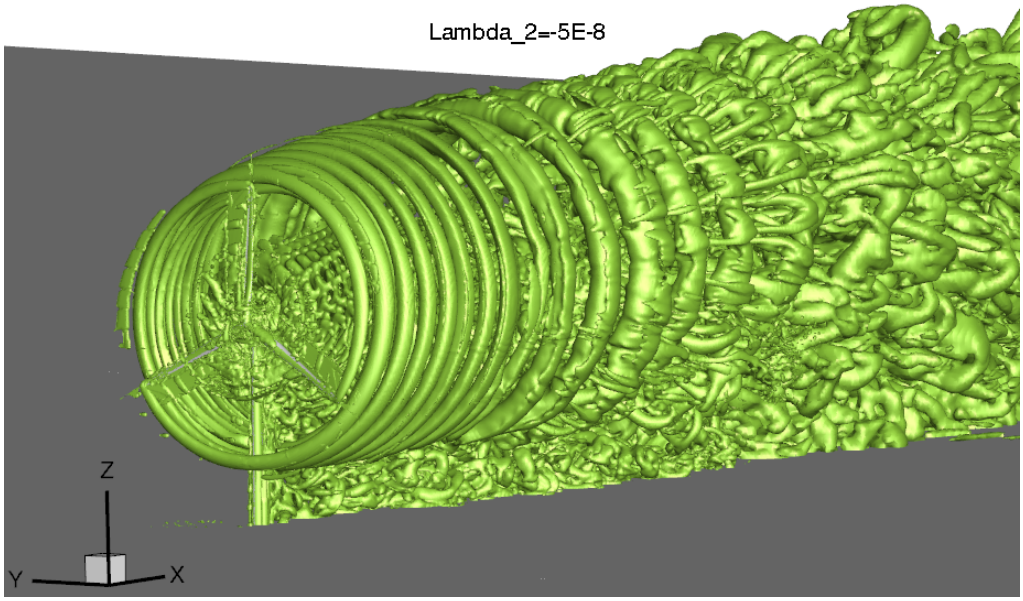

Figure 1.20: Full model wind turbine vortex surfaces

The main structure of thermo-fluid examinations is governed by equations based on the conservation law of the physical properties of the fluid.
CFD's mathematical fundamentals are the Navier-Stokes equations that govern fluid behaviour and are derived from the conservation laws of momentum, energy, and continuity.
Since the relative wind speed for wind turbine blades is much lower than the speed of sound speed we can consider the air incompressible for our case study and the before mentioned governing equations can be written in the convective form as follows [33]:

$$\nabla \cdot u = 0 \tag{1.8}$$

$$\frac{\partial u}{\partial t} + (u \cdot \nabla)\, u = -\nabla P + \nu \nabla^2 u \tag{1.9}$$

The 3D blade geometry needs to be accurately described in a digitized format through a CAD software for CFD modelling of wind turbine blades.
Wind turbine blade's have a complex geometry and is therefore quite complicated to generate a suitable and accurate mesh.
Typical mesh types are three:

- **structured mesh** has high resolution, easy convergence and low memory usage but had instead difficulties to describe properly complicated geometries
- **unstructured mesh** instead can describe accurately complex geometries but are more time and computational consuming
- **hybrid mesh** is a combination of the two above and uses a structured mesh for important regions, such as boundary layers, while unstructured mesh is used elsewhere.
  Thanks to his flexibility, hybrid mesh has been widely used in the current CFD modelling of wind turbine blades [34].

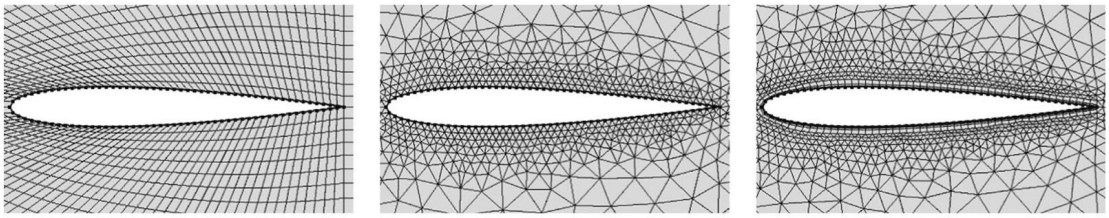

Figure 1.21: CFD mesh typology

It is possible to achieve the discretion of NS equations through three typical methods of discretion:

- **FVM (method of finite volume)** is the common method used in CFD modelling, as it has solution speed and memory usage advantages.
- **(FEM (method of finite-element)** is much more stable compared to FVM, but it consumes more memory and has slower solution times [35]
- **FDM (method of finite-difference)** is easy to implement but limited to simple grids and for this reasons is used by only a few specialised codes

A turbulence model based on RANS (Reynolds Averaged NS equations) is required to apply NS equations to solve practical engineering problems on wind turbine blades.
RANS equations are time-averaged equations used to describe turbulent flows of fluid flow motion based on the Reynolds decomposition by decomposing an instant quantity into its time-averaged and fluctuating quantities [36].

Models of turbulence can be classified on the basis of computational costs, which corresponds to the range of scales modelled versus resolved.
When the majority of turbulent scales are modelled, the computational cost is very low, but the trade off comes in the form of reduced accuracy.
Different RANS-based turbulence models were used for wind turbine applications, such as SST model, $k-\epsilon$ model, $k-\omega$ model and Spalart-Allmaras model.
We will deeply analyse later the turbulence model used for the CFD analysis run for this thesis and the Task 29 project.
CFD has been widely used for wind turbine aerodynamic and aeroelastic analysis since the computational resources of the current clusters has increased exponentially over the last decade.

	BEM model	VORTEX model	Actuator type model	CFD model
Accuracy	***	***	***	****
Computational speed	****	***	**	*
Airfoil aerodynamic data required?	Yes	Yes	Yes	No
Viscous effects included?	Yes	No	Yes	Yes

Table 1.1: Comparison of aerodynamic models

1.4.2 Structural models

To calculate a wind turbine's aeroelasticity response, it is necessary to include the structural model to determine the displacements and the consequently temporal variation of the loads in the different components.
Structural models used in aeroelastic modelling of wind turbine blades can be roughly categorized into two groups:

- **3D FEM model** uses 3D composite shell elements to describe composite layer characteristics throughout shell thickness of wind turbine blades.
  Wind turbine blades are objects with a complex structure, typically consisting of many layers of fiber-reinforced composite material with the required shear webs, root fixtures and tapering cross sections.
  The above mentioned constructions complexity requires a 3D FEM model to examining the internal stresses distribution and coupled with CFD to perform aeroelastic modelling of wind turbine blades provide accurate results but is computationally expensive and is therefore rarely used [37].

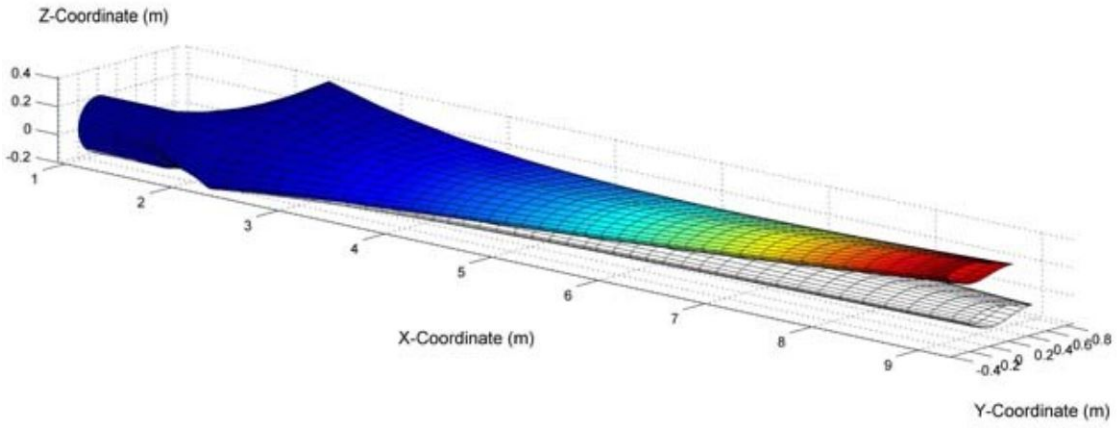

Figure 1.22: 3D FEM model of a wind turbine composite blade [38]

- **1D beam model** is used to model efficiently wind turbine blades and components since they have one of their dimensions significantly larger than the other two.
  The beam axis is defined along the largest dimension and it is considered that a cross section perpendicular to this axis varies along the beam span and characterised the blades with their local structural properties.

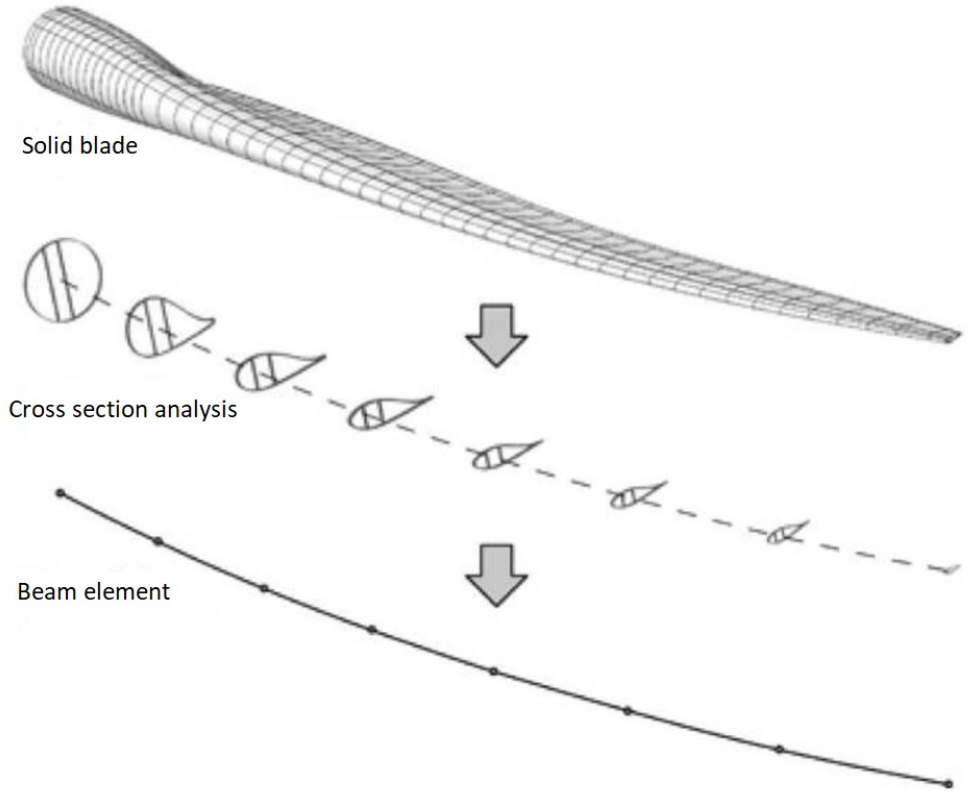

Figure 1.23: Beam model of wind turbine blade

A lot of beam models have been developed over the years but the most used

and important are:

- **Euler-Bernoulli beam model** known as the classic beam model deals with slender beams that are subject to extended, torsional and bending loads but ignore the shear deformation [39].
- **Timoshenko beam model** was developed by Timoshenko in the early 20th century, takes account of shear deformation effects, making it more suitable for describing the behaviour of thick and short beams than the Eulero-Bernoulli model [40].

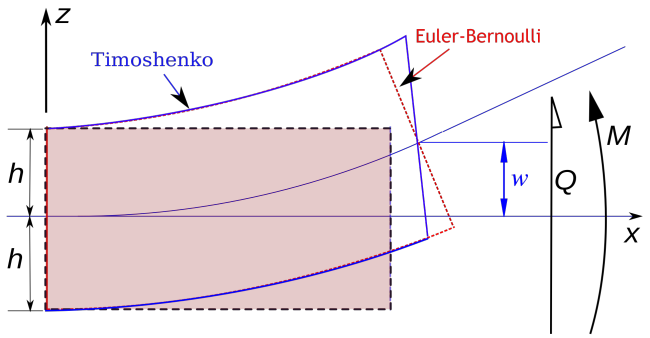

Figure 1.24: Timoshenko beam (blue) compared with Euler-Bernoulli beam (red)

- **GEBT (geometrically exact beam theory)** is a non lineal model where the deformed beam geometry (i.e. the displacements and rotations of the beam reference line) is represented exactly.
  In fact both the Euler-Bernoulli and Timoshenko beam models contain the assumption of small deflections that is not exact for current wind rotor blades with large deflections.

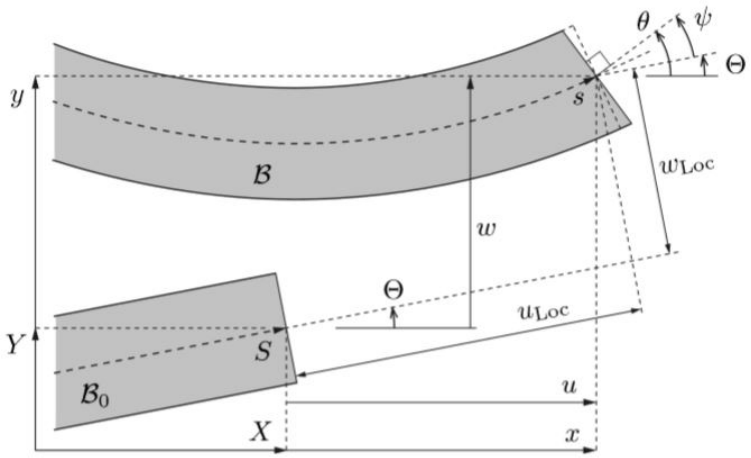

Figure 1.25: Nonlinear kinematics of the geometrically exact beam [41]

Three types of discretionary methods are often used to discrete the blade into a series of 1D beam elements:

– **Modal approach** describes the deflection shape of the flexible bodies, such as the blade and tower, as a linear combination of a set of mode shapes and is a way to reduce the number of DOFs and thus reducing the size of matrices and accelerating the computations per time step.

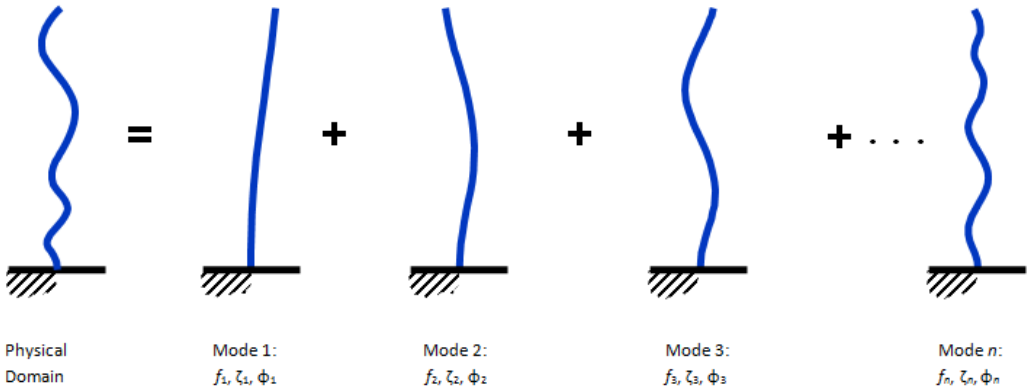

Figure 1.26: Structure of the modal analysis

However the modal approach is computationally efficient, it has at the same time some limitations due to the type and number of DOFs allowed in the structure.
For example, FLEX5 [42], which is a widely used aeroelastic analysis model based on the modal approach, uses only the initial three or four eigenmodes for the blade and the torsional eigenmodes, which are important for flutter analysis, are generally not available.
Another major limitation of the modal approach is due to its linear assumption because a linear combination of the provided mode shapes describes the deflection shape of the flexible components and therefore the model is not capable of handling the flexible blade's large deflections.
In conclusion is important to underline how the modal approach deserves a finite element based pre-processor the first to obtain the mode shapes of the blade.

– **MBD (multi-body dynamics)** is a method for studying the dynamic behaviour of interconnected rigid or flexible bodies that can have translational and rotational displacements.
These bodies are interconnected by force elements (such as springs) or kinematic constraints (such as joints) and structural dynamics can be assessed using motion equations, usually derived from Lagrange's equations or Newton-Euler equations [43].

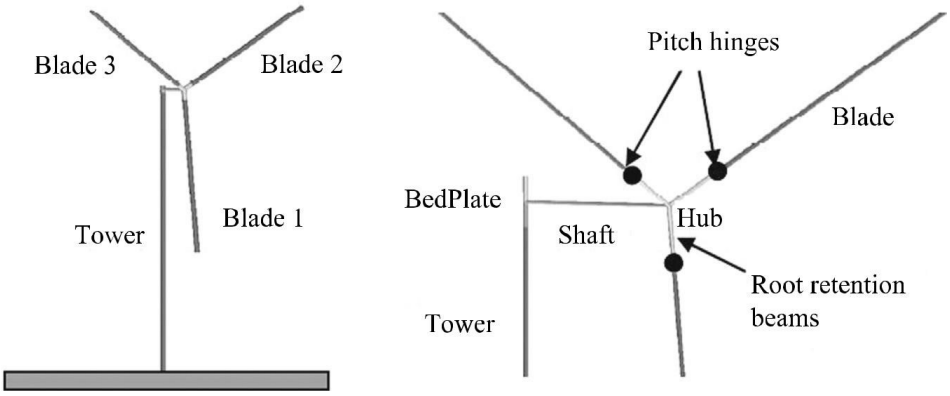

Figure 1.27: An example of wind turbine MBD configurations

Compared to the modal approach, the MBD method benefits from high modelling flexibility, requiring more computational resources, but it allows the modelling of an increased number of DOFs.

– **1D FEM method** is widely used in the aeroelasticity of wind turbines because it allows a more comprehensive and accurate deformation description by analysing an assembly of finite elements connected by nodes.

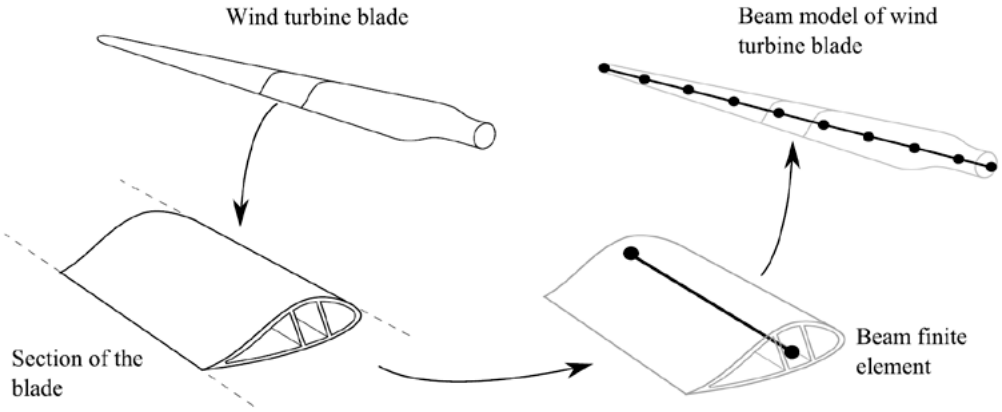

Figure 1.28: Beam finite element of wind turbine blade

Compared to other discretization methods, the 1D FEM requires more computational resources but is, thanks to his flexibility and accuracy, the most used and will be implemented in this thesis.

	Modal approach	MBD	1D FEM
Accuracy	*	**	***
Computational speed	***	**	*
Number of DOFs	*	**	***
Prescribed modal shapes required?	Yes	No	No

Table 1.2: Comparison of discretisation methods

1.5 State of the Art

In this section we will announce and discuss the different aeroelastic models developed over the years by academic research teams or by the industry for the analysis of wind turbine aeroelasticity response.
Let's start with the first ever wind turbine aeroelastic models developed within the European Non-Nuclear Energy project JOULE III, STALLVIB [44].
This code was designed to predict dynamic loads and investigate problems of edgewise instability.
After this first attempt a lot of codes were developed and are listed ad described in more detail below:

- **ADAMS/WT (Automatic Dynamic Analysis of Mechanical Systems – Wind Turbine)** was developed by Mechanical Dynamics Inc. (MDI) with the help of National Renewable Energy Laboratory (NREL)[44].
- **FAST (Fatigue, Aerodynamics, Structures, and Turbulence)** has been designed by National Renewable Energy Laboratory (NREL) to analyse both two- and three-bladed horizontal-axis wind turbines [45] and has been certificated by Germanisher Lloyd [45].
- **FLEX5** has been created by the Fluid Mechanics Department at the Technical University of Denmark (DTU) and is capable of simulating wind turbines with different configurations [42].
- **GAST (General Aerodynamic and Structural Prediction Tool for Wind Turbines)** is a code designed by the National Technical University of Athens that implement also a module to generate turbulent wind fields and a post-processing module to perform fatigue analysis [46]
- **GH-Bladed** is an integrated and validated commercial software package created by Garrad Hassan (GH) Ltd and based on a windows interface (GUI) [47].

- **HAWC2 (Horizontal Axis Wind Turbine Code 2nd generation)** has been developed by Technical University of Denmark (DTU) for horizontal axis in time domain [48]
- **PHATAS (Program for Horizontal Axis Wind Turbine Analysis Simulation)** was developed by ECN (Energy research Centre of the Netherlands) to predict the dynamic behaviour and the corresponding loads on horizontal axis wind turbines [49]
- **CFD-CSD based programs** where the aerodynamic part uses a CFD solver like **FLOWer [50], ©2019 ANSYS Fluent or ©STAR-CCM +** to obtain the aerodynamic blade loads based on the time-accurate solution of the unsteady Reynolds-averaged Navier-Stokes equations.
  On the other side the structural part is based on a CSD solver like **Carat++ [51], Kratos Multiphysics [52] or ©SIMPACK** and is used to calculate the blade deformations

Program name	Structural blade model	Structural discretization method	Aerodynamic model	Blade cross-sectional properties necessary?
ADAMS/WT	1D beam	MBD	BEM	Yes
FAST	1D beam	MA	BEM	Yes
FLEX5	1D beam	MA	BEM	Yes
GAST	1D beam	1D FEM	Free wake panel	Yes
GH-Bladed	1D beam	MA	BEM	Yes
HAWC2	1D beam	MBD	BEM	Yes
PHATAS	1D beam	1D FEM	BEM	Yes
CFD-CSD based programs	3D beam	3D FEM	CFD	Yes

Table 1.3: Overview of wind turbine aeroelastic models

1.6 Goal of this thesis

Analysing the state of the art in aeroelastic modelling of wind turbine is at a first sight clear how most commercial codes are based on the BEM model concerning the aerodynamic part and on the 1D FEM beam model regarding the structural part.
The BEM model, as seen before, has been developed over years and has some correction factors that make it more accurate and performing towards unsteady behaviour of the flow.
However a CFD analysis can describe better the unsteady behaviour and the wake flow and allow flow visualization around and behind the wind rotor.
Regarding the structural part, most of the 1D FEM beam based models are linear models based on assumption of small blade deflections and do not take account of large deflection effects on modelling responses and loads.
The goal of this thesis is to create the structural model of the DANAERO wind turbine rotor in terms of 1D FEM and consistent to the beam model available for the aeroelastic tool HAWC2.
Starting from an already available CFD model of the same turbine, the structural model will be created using the open-source Finite Element based software KRATOS.
Before performing FSI simulations, the influence of the number of 1D elements, the interpolation between the structural properties, and the importance of the different structural parameters on the resulting eigenfrequencies of the model will be deeply analysed and documented.
The differences of the structural modelling approaches in the aeroelastic answer will identify limitations, advantages and disadvantages in the different cases.
The CFD solver that will be used for the FSI simulations is URANS solver FLOWer.
In order to perform the simulations, a maximum timestep analysis needs to be carried out and maybe some changes in the meshes will be necessary, using the commercial software Pointwise.
At the end, all results of the work will be documented.

- Creation of a 1D FEM model of the wind turbine rotor
- Investigation of influence of the structural parameters on the eigenfrequencies
- Performance of FSI simulations with Kratos Multiphysics
- Documentation of the work

Chapter 2

Baseline turbine configuration

2.1 Introduction

This chapter describes the configuration of the wind turbine to an extent in order to be able to perform aeroelastic calculations with the provided model of the NM80 turbine structure based on the work done in the EU STABCON project in 2004 [53] for the aeroelastic models developed for HAWC and HAWC2 code.
Here are the details of the baseline turbine configuration used in the investigations and we will focus first on the aerodynamic and structural properties of the blades and secondly on the tower and support structure.
Although the CAD model of the entire wind turbine is present for the CFD modelling, the geometrical properties are important in order to change reference system and to create the 1D FEM model for the structural analysis.
A lot of attention will be given on the reference system in which the difference structural properties of the wind turbine are given and it will be explained how to change them from one system to the other.

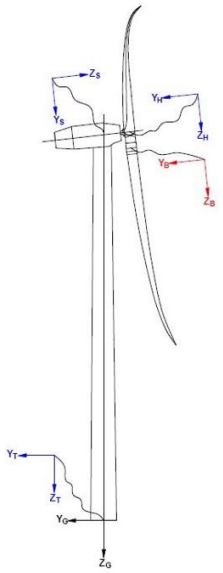

Figure 2.1: Reference systems for the entire wind turbine [48]

2.2 Blades structure

In order to understand the different values that will be given in this section, it is important to introduce first the blade reference system which is set at the blade half chord and is rotated at a twist angle θ_z related to main body coordinates set at the blade root ($X_B - Y_B$).

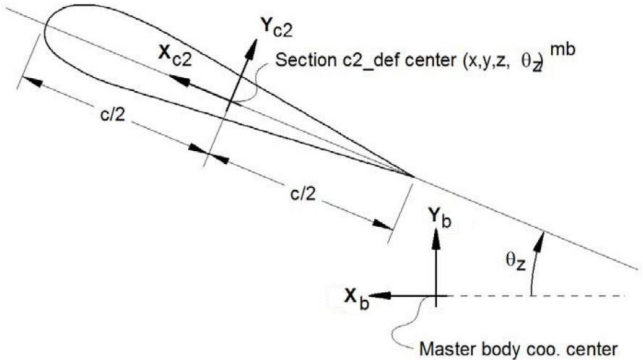

Figure 2.2: Illustration of c2 coordinate system related to main body coordinates [48]

Another important detail is that the blade half chord coordinates include the twist angle but exclude the hub-blade substructure.

$X_{c2}\,[m]$	$Y_{c2}\,[m]$	$Z_{c2}\,[m]$	$\theta_z\,[°]$

Table 2.1: Blade half chord coordinates related to main body coordinates

The position of the mid chord of the blade itself is not sufficient because the structural properties are related to the elastic center of every single section of the beam model.
More geometrical properties are therefore necessary and the next table provides the position of the elastic center (EA), the center of mass (CG) and the shear center (SC) with respect to the half-chord reference frame.
While shear and gravitational centres are simply translated, the elastic center and principal bending axis are not only translated but also rotated in relation to the mid-chord reference frame by a pitch angle θ_s as depicted in the next figure.

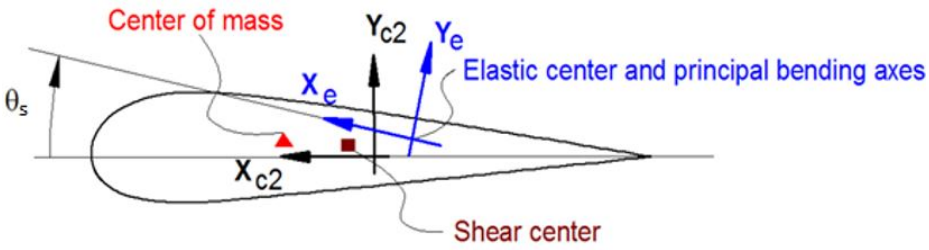

Figure 2.3: Schematics of the elastic reference frame [48]

$Z\,[m]$	$X_{CG}\,[m]$	$Y_{CG}\,[m]$	$X_{SC}\,[m]$	$Y_{SC}\,[m]$	$X_{EA}\,[m]$	$Y_{EA}\,[m]$	$\theta_s\,[°]$

Table 2.2: CG, SC, EA positions related to c2 reference frame

2.2.1 Aerodynamic properties

In this section the list of the aerodynamic properties of the blade will be shortly presented without listing them for copyright reasons.

Z [m]	Chord [m]	Relative thickness [%]	Airfoil type

Table 2.3: Blade aerodynamic properties

2.2.2 Structural properties

After we have discussed the geometrical properties of the blade and its representative centres and axis, let's analyse which structural properties we got from the EU STABCON project and how we can get from those information the values we need to implement the 1D FEM model.
First of all it's important to underline that in order to perform our FEM analysis, the structural properties have to be set around the principal bending and torsional axis positioned at the SHEAR CENTER while the values we got are referred to the axis placed at the elastic center.

In the following items there will be explained the single steps that where undertaken to achieve the values referred to the SHEAR CENTER:

- the starting point of the procedure are the available data:

$Z\,[m]$	m $[kg/m]$	Area $[m^2]$	E $[N/m^2]$	G $[N/m^2]$	$I_{x_{CE}}$ $[m^4]$	$I_{y_{CE}}$ $[m^4]$	$I_{P_{CE}}$ $[m^4]$

Table 2.4: Starting blade structural properties

- the next step consist in rotating the principal bending and torsional axis of the ELASTIC CENTER to the orientation of our mid-chord reference system which are the same for our 1D FEM model (see Figure 2.4).
  This is done by the next set of equations:

$$I_{x'} = \frac{I_x + I_y}{2} + \frac{I_x - I_y}{2} cos(2\theta) - I_{xy} sin(2\theta) \tag{2.1}$$

$$I_{y'} = \frac{I_x + I_y}{2} - \frac{I_x - I_y}{2} cos(2\theta) + I_{xy} sin(2\theta) \tag{2.2}$$

  in which $\theta = \theta_s + \theta_z$ and the last term of both equations containing the product of inertia of area (I_{xy}) can be considered zero because I_{xy} is not provided in the data set and its value is zero in case of the presence of at least one axis of symmetry in the geometry. For our case study the airfoil is slightly cambered but in first approximation to simplify the problem can be considered symmetrical.

- once the reference system is rotated it is possible to translate it first to the center of mass and then to the shear center using the "Parallel axis theorem":

$$I = I_{cm} + Ad^2 \tag{2.3}$$

  where d represents the distance between the new axis and the parallel axis that passes across the center of mass.
  For our case study the first set of equations are:

$$I_{x_{CG}} = I_{x_{CE_{ROT}}} - A(y_{CE} - y_{CG})^2 \tag{2.4}$$

$$I_{y_{CG}} = I_{y_{CE_{ROT}}} - A(x_{CE} - x_{CG})^2 \tag{2.5}$$

$$I_{p_{CG}} = I_{p_{CE}} - A\left(\sqrt{(x_{CE} - x_{CG})^2 + (y_{CE} - y_{CG})^2}\right)^2 \tag{2.6}$$

  There are some things to notice, the first one is that in this case we start from a different point and move back to the center of mass and the second one is that the distances between axis set on the same points are different from direction to direction.

- the last translation using the "Parallel axis theorem" is the one of the reference system from the center of mass to the SHEAR CENTER:

$$I_{x_{SH}} = I_{x_{CG}} + A(y_{SH} - y_{CG})^2 \tag{2.7}$$

$$I_{y_{SH}} = I_{y_{CG}} + A(x_{SH} - x_{CG})^2 \tag{2.8}$$

$$I_{p_{SH}} = I_{p_{CG}} + A\left(\sqrt{(x_{SH} - x_{CG})^2 + (y_{SH} - y_{CG})^2}\right)^2 \tag{2.9}$$

  Compared to the previous set of equation, this time we moved from the center of mass out and therefore there is a sum of the second term considering the distance.

- the last step is focused on the Young's modulus and shear modulus and their relationship. Under the assumption of isotropic and linear elastic material, we can define the Poisson's ratio as follows:

$$\nu = \frac{E}{2G} - 1 \tag{2.10}$$

  In the data set we have both the Young's and the shear modulus and is therefore possible to calculate the Poisson's ratio for every single piece of our blade.

$Z\,[m]$	$Poisson$	$I_{x_{SC}}$ $[m^4]$	$I_{y_{SC}}$ $[m^4]$	$I_{P_{SC}}$ $[m^4]$

Table 2.5: Calculated blade structural properties at the SHEAR CENTER

We have now calculated the structural properties at the SHEAR CENTER and we know the SHEAR CENTER position related to the mid-chord (c2) reference frame. However the mid-chord reference frame, as depicted in figure 2.5, changes its position along the blade span with respect to the main body coordinates set at the blade root. In the 1D FEM analysis our reference frame is set at the blade root and is therefore necessary to calculate the SHEAR CENTER position referred to this one as following:

$$x_{SC_{main\,body}} = x_{c2} + x_{SC} \tag{2.11}$$

$$y_{SC_{main\,body}} = y_{c2} + y_{SC} \tag{2.12}$$

$Z\,[m]$	$x_{SC_{main\,body}}\,[m]$	$y_{SC_{main\,body}}\,[m]$

Table 2.6: SHEAR CENTER position in the main body coordinate system

2.3 Tower and support structure

In this thesis not only the static and dynamic behaviour of the blade will be investigated but also the tower will be analysed.
The tower is composed bottom up by the foundation, the tower part and the nacelle element.
In this chapter the properties of the whole tower will be presented but it is important to take into account that for the next CFD modelling the nacelle element will be partly unconsidered.
The next table reports some general dimensions of the wind turbine tower got from the project.

Hub height [m]
Tower height [m]
Tower bottom radius [m]
Tower top radius [m]

Table 2.7: Overall dimensions of the tower

The geometrical and structural properties will be presented and differently than the blade there are here less calculations to do because the tower has an axisymmetric shape and therefore shear, elastic and mass centres overlap each other and are placed at the origin of the axis along the tower height.
As before, at this stage we consider an isotropic and linear elastic material and the Poisson's ratio si calculated.

$Z\,[m]$	m $[kg/m]$	Area $[m^2]$	E $[N/m^2]$	G $[N/m^2]$	ν	$I_{x_{CE}}$ $[m^4]$	$I_{y_{CE}}$ $[m^4]$	$I_{P_{CE}}$ $[m^4]$

Table 2.8: Tower geometrical and structural properties

This chapter includes all the properties needed for the structural analysis of the blade and the tower.
In this thesis the whole structure of the wind turbine will not be investigated and therefore components like the hub and the drive-train are not discussed and their properties not analysed and reported.

Chapter 3

Structural modelling

3.1 Introduction

Let's get into the core of the thesis with the first of the element necessary for the aeroelstic analysis.
In this chapter the utilised FEM code "Kratos-Multiphysics" is going to be first discussed in detail, afterwards the theoretical background and the characteristic of the structural model are introduced and at the end a verification of the software is done based on the comparison with analytical results.

3.2 Kratos Multiphysics

3.2.1 Introduction

Kratos was developed by CIMNE (Centre Internacional de Mètodes Numèrics a l'Enginyeria) in Barcellona and is designed as an Open-Source framework for implementing numerical methods for the solution of engineering problems, is written in C++ and its design is focused on modularity as well as on performance [54].
This framework was created for the development of multidisciplinary programs for finite elements and therefore provides several tools for easy deployment of finite-element applications and a common platform for easy interaction between them [55].
The kernel and application approach and a layers based design are used to reduce the possible conflicts arising between developers of different fields and with different programming knowledge.

3.2.2 Users

Kratos, due to its multidisciplinary nature, provides a variety of algorithms that can be implemented in different engineering areas and is therefore widely used [56].
The main categories of users are:

- Finite Element Developers: who are considered to be more FEM expert from a physical and mathematical point of view and who will not be involved in advanced programming concepts.
- Application Developers: who are less interested in finite element programming and their programming knowledge may vary from very expert to higher than basic.
  Developers of optimization programs or design tools are the typical users of this kind.
- Package Users Engineers: who use Kratos and its applications to model and solve their problem without getting involved in internal programming of this package.
  This kind of users like a flexible external interface (GUI) in order to build up the problem and visualize the solutions.

In this thesis Kratos is used in a way between developers and engineers because to solve our core problem is necessary to implement and modify some specific settings.

3.2.3 Properties

There is here a list of why and where is Kratos useful:

- MULTI-PHYSICS: Kratos allows the combination of different analysis (thermal, fluid dynamic, structural) with optimising methods in one global software package with just one user interface and with customising opportunities.
- FINITE ELEMENT METHOD (FEM) based: Kratos is FEM based and therefore allows the treatment of most engineering and applied science problem governed by Partial Differential Equations (PDE) in a powerful, flexible and versatile way.
- OPEN SOURCE: the main code and program structure is available and distributed without any restriction, but with the possibilities to develop new parts of the code on an open or close basis.
- FREE: because the software is devoted mainly to developers, researchers and students, because you have the freedom to modify and distribute it and, therefore, is the best way to share knowledge and built a robust numerical methods laboratory.

- OBJECT ORIENTED DESIGN: from the computational point of view, the modular design, hierarchy and abstraction of the object oriented philosophy fits to the generality, flexibility and reusability required for the current and future challenges in numerical methods.
  This methodology consists in splitting a problem into multiple individual objects and defining their interactions through a common interface which for this software reproduces the concepts of the finite element structure [52].

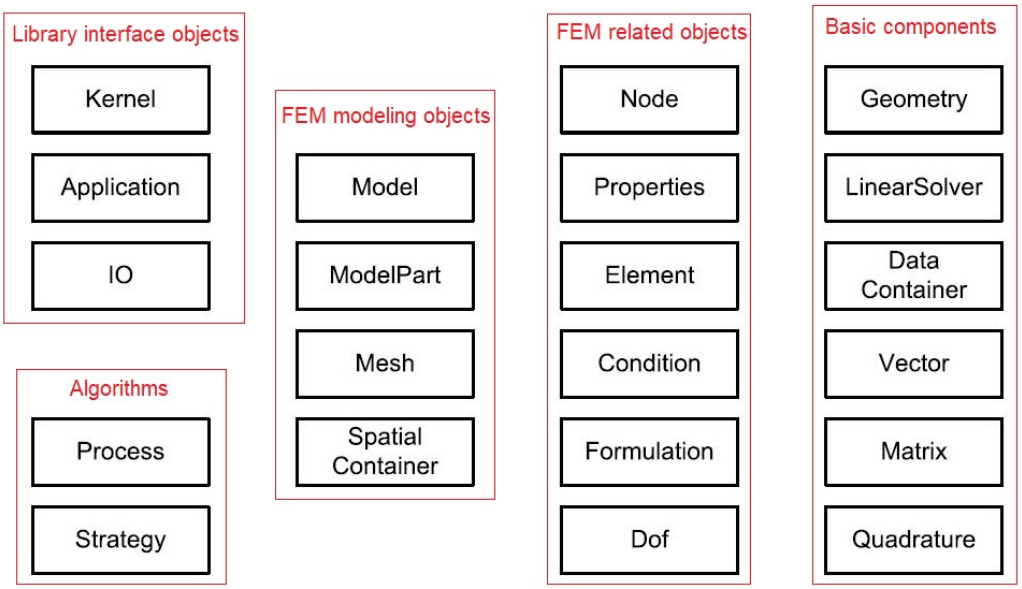

Figure 3.1: Main classes defined in Kratos

- MULTI-LAYERED-DESIGN: in which each object only interacts with other objects in its layer or in a more basic layer.
  Layering reduces the dependency inside the program while helping the the maintenance of the code and providing developers a better understand of the code [52].
  The layering is created in a way so that each user has to work in the minimum number of layers as possible reducing the amount of code to be known by each user.
  The layers are summarised in the following figure.

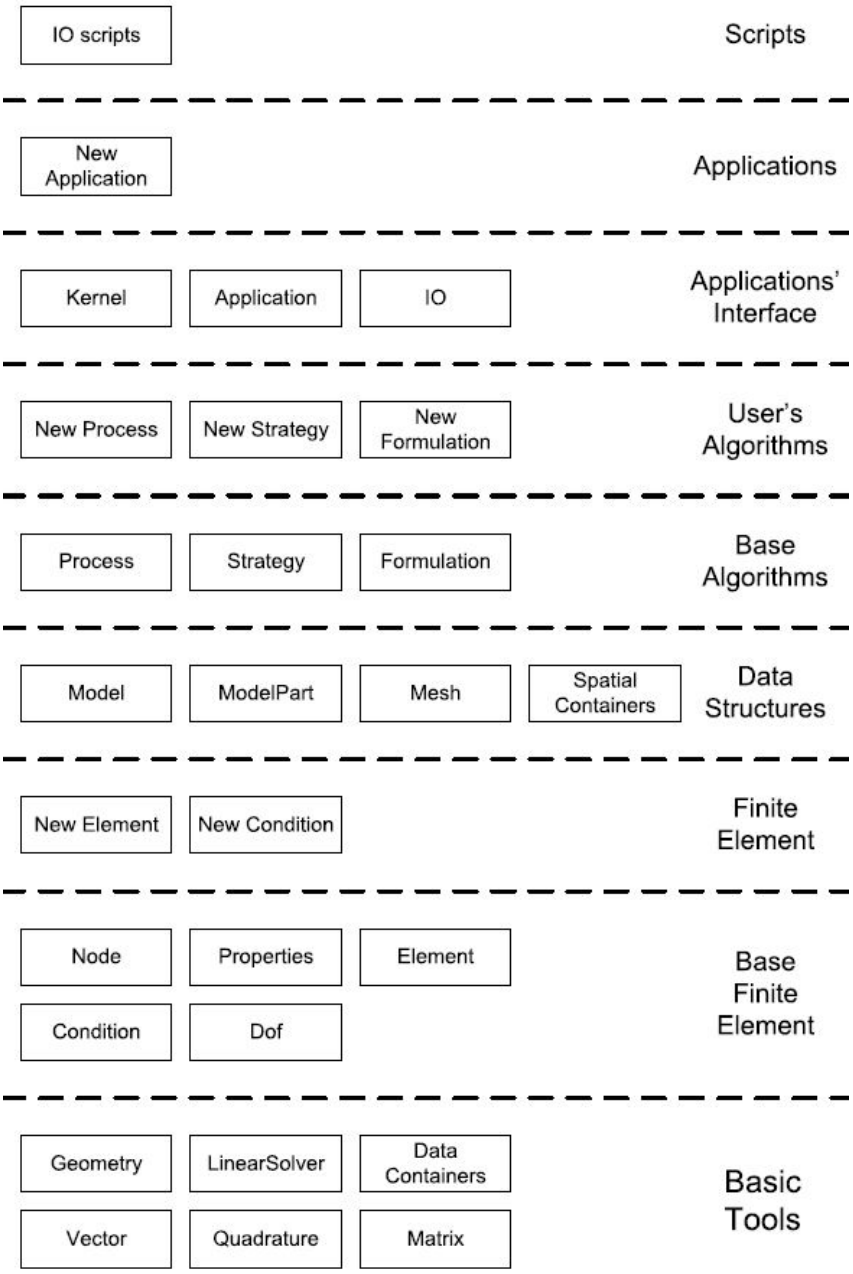

Figure 3.2: Multi-layer nature of Kratos

3.2.4 Input files

Problems in Kratos are generally described by a certain number of files which contains the information needed from the solver to produce results.
Differently than other software, Kratos doesn't deserve a graphical interface to be set up and the input files are readable by a simple text editor and can be created just by typing names and numbers.

A Kratos case consists of three different types of files:

The project parameters file

This Kratos file is commonly referred to as "ProjectParameters.json," is responsible for simulation settings and contains four main blocks:

- *problem_data*: general settings for the Kratos run
- *solver_settings*: that contain the most important information regarding the analysis
  - "*solver_type*": static/quasi static/dynamic/eigenvalues
  - "*analysis_type*": linear/non linear
  - "*time_stepping*"
  - "*convergence_criterion*"
  - "*linear_solver_settings*"
- *processes*: to apply boundary conditions, forces, moments, gravitational and cetrifugal loads
- *output_processes*: settings for the output file as binary or for post-processing software

The Model part file

The "ModelPart" file with extension ".mdpa" contains the model information in Kratos specific syntax.
Through this file the Modelpart is created which is the basis for generating the geometry, submodels for specific materials, boundary conditions or forces and to generate the mesh.

- **Geometry** is created by defining the nodes and their position in the tree dimensional space. The syntax looks like [56]:

  Begin Nodes
  // id X Y Z
  End Nodes

- **Elements** are necessary for the mesh generation, for the FEM analysis and for defining specific material properties on different elements of the structure. At this stage the type of element used for the FEM analysis is specified.
  For our simulations we will use corotational linear/non linear beam element in 3 dimensions and with 2 nodes (CrLinearBeamElement3D2N/CrBeamElement3D2N).

Elements are created by defining the extreme points of them using the nodes defined before.

Begin Elements *element_type* // *element_name*
// id *prop_id* node1 node2
End Elements

- **ElementalData** is therefore necessary to define the reference system for every element created for the mesh.
  This is important in order to assign a reference system in which loads and moments can be computed but also material properties can be assigned.

  Begin ElementalData *elemental_data_name*
  id [dimensions] (x, y, z)
  End ElementalData

- **conditions** are necessary for applying loads and moments

  Begin Conditions
  //id type node
  End Conditions

- **SubModelPart** are, as the name tell, subpart of the model that enable the user to customise components of the model through specific materials properties, forces, moments and boundary conditions.

  Begin SubModelPart *submodel_name*
  Begin SubModelPartNodes
  // id node
  End SubModelPartNodes
  Begin SubModelPartElements
  // id element
  End SubModelPartElements
  Begin SubModelPartConditions
  End SubModelPartConditions
  End SubModelPart

The Material part file

Before running the simulation, for a structural analysis the material properties can be set at the beginning of the "ModelPart" file or in a separated .mpda file [56]. Different properties can be set in accordance with the desired constitutive law and there is also the opportunity to set variable properties for variable elements.

The following properties of the beam have to be defined for our case of interest:

- Density
- Young modulus
- Poisson ratio
- Cross sectional area
- I22: Bending inertia along the flapwise direction
- I33: Bending inertia along the edgewise direction
- Torsional inertia

The Kratos python script

This file is generally named "MainKratos.py", is responsable for loading the required Kratos applications, calling the main Kratos functionalities and user settings and, at the end, running the simulation [56].

3.2.5 Graphical User Interface (GUI)

As mentioned before, Kratos Multiphysics can be used through the software "GiD" which enables pre and post-processing by an easier and at a first sight more clear graphical interface. All the above mentioned input files are created automatically from GiD after the user has set up the structural simulation trough the structural GUI depicted in the image below.

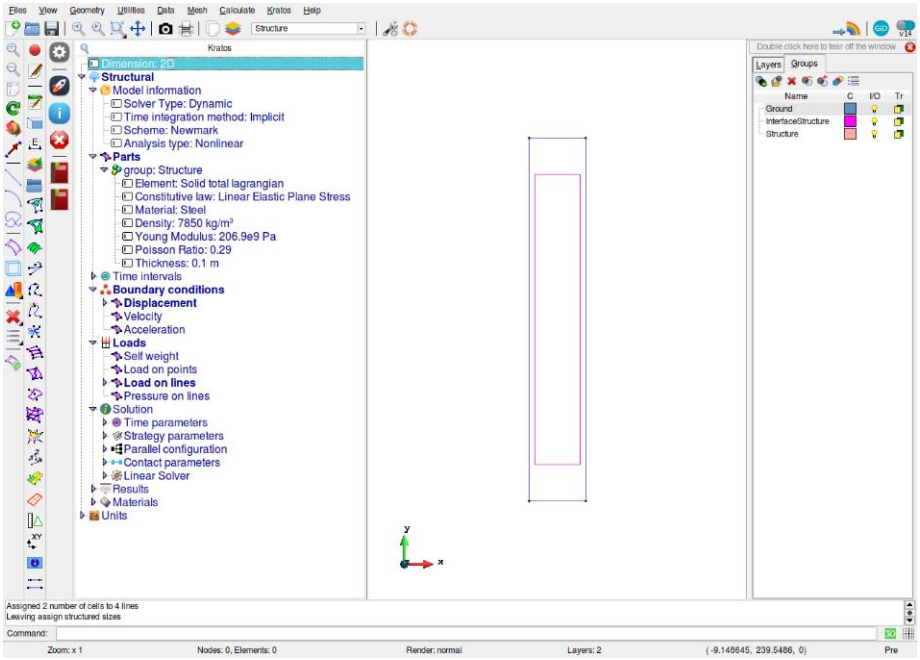

Figure 3.3: GiD software for Kratos structural application [56]

3.3 Beam element 3D2N

In this section we are going to analyse in detail the element used for the FEM analysis, its properties from different point of views and the governing equations that we are going to implement and solve in our simulation.
Let's start saying that we will treat every component of the wind turbine as a beam structure.
In this thesis the tower and the blade will be structurally studied as beam since their axial extension is predominant when compared to any other dimension orthogonal to it [57].
The cross-section of the beam is identified by intersecting the structure with planes that are orthogonal to its axis, whereas geometry, displacements, strains and stresses are referred to an orthonormal coordinate frame of reference [57].
For our case study we will describe the structures through a corotational linear/non linear beam element 3D2N under the assumption of small displacements.
This element uses a corotational reference frame, has 2 nodes placed in 3 dimensions, can account geometrical linearities or non linearities and has 3 degrees of freedom for each node as shown in figure below.

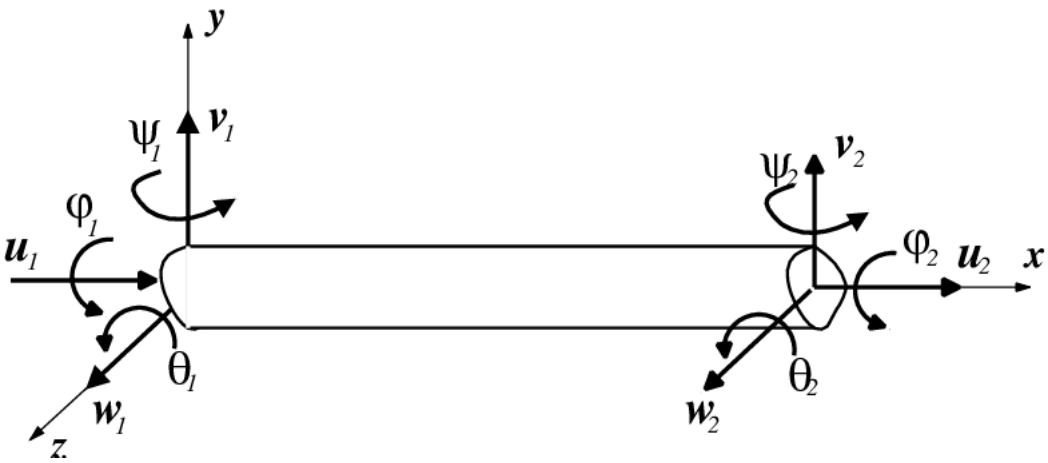

Figure 3.4: 3D 2 nodes beam element

3.4 Corotational formulation

The formulation of the corotational beam considers a beam element with reference to the local coordinate system based on elements [58]. Using this approach, any frame structure arbitrarily displaced and rotated at the global level can be solved by decomposing the movement of its beam elements into its corresponding rigid body and pure deformation motions [58].
The global displacements of the end nodes are removed from the motion of the beam referred to its local reference frame and therefore only local strain producing deformation are taken into account.

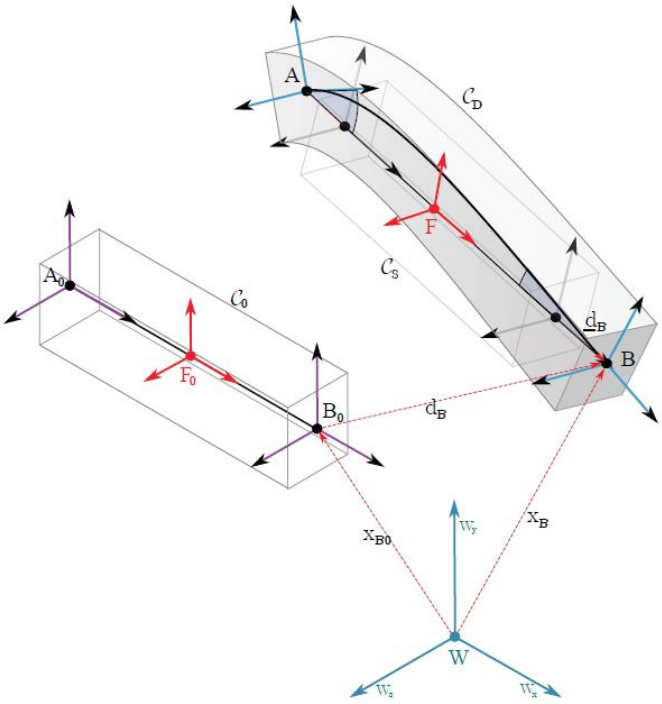

Figure 3.5: A schematic representation of the corotational concept

A foating coordinate system F follows the deformed element, so the overall gross movement into the deformed state C_D can be viewed as the superposition of a large rigid body movement from the reference configuration C_0 to the so-called floating or shadow configuration C_S, plus a local deformation from C_S to C_D.

3.5 The Euler–Bernoulli theory

The Eulero-Bernoulli model (Euler, 1744) (EBBT) represents a classical beam theory and is a reference model for describing the mechanism of a slender homogeneous beam under bending [57].

3.5.1 Assumptions, kinematics and deformations

The EBBT model is based on the following assumptions:

1. the cross-section is rigid on its plane
2. the cross-section rotates around a neutral surface remaining plane
3. the cross-section remains perpendicular to the neutral surface during deformation

A consequence of the hypothesis is that Poisson contractions in the transverse direction due to axial strains are ignored.
The cross-section deformed position is described uniquely by those vectors:

$$\mathbf{w} = \begin{bmatrix} w_x \\ w_y \\ w_z \end{bmatrix}, \quad \theta = \begin{bmatrix} \theta_x \\ \theta_y \\ \theta_z \end{bmatrix} \tag{3.1}$$

Under the assumption of small displacement components, w_x, w_y, w_z are small compared to the beam length l and therefore the rotational components can be rewritten as:

$$sin\theta \approx tan\theta \approx \theta \tag{3.2}$$

At this stage let's look at a material point on the cross-section with the referential coordinates (x, y, z) that achieves a displacement vector $u = u(x, y, z)$ with the u_x, u_y, u_z components.

$$\begin{cases} u_x(x,y,z) = w_x(x) + z\theta_y(x) - y\theta_z(x) \\ u_y(x,y,z) = w_y(x) - z\theta_x(x) \\ u_z(x,y,z) = w_z(x) + y\theta_x(x) \end{cases} \tag{3.3}$$

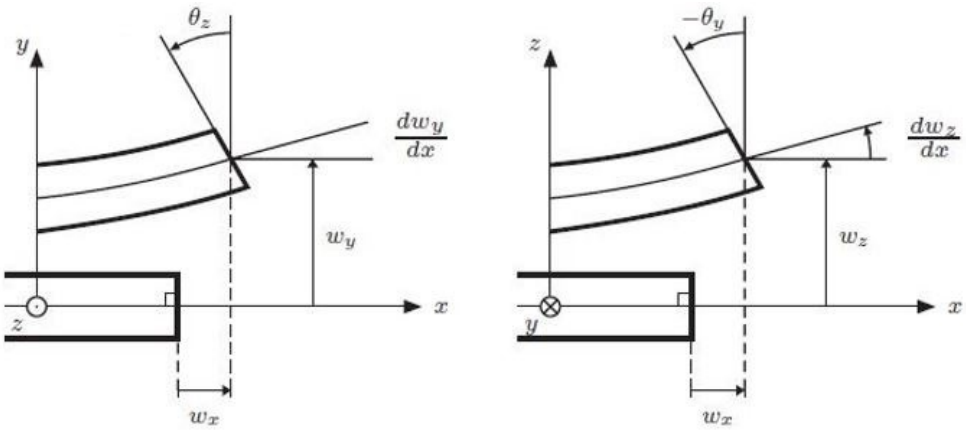

Figure 3.6: Deformation components in the bending beam theory

For simplicity let's analyse only one bending direction and assume that $\theta_x = 0$ disregarding for the moment the twist of the beam.

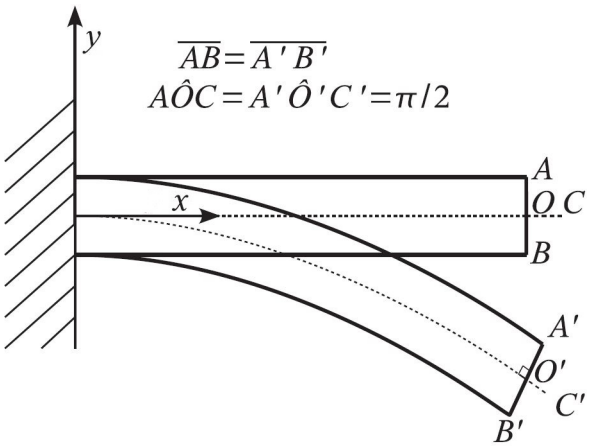

Figure 3.7: Bending of a beam according to the kinematic hypotheses of Euler – Bernoulli [57]

The in-plane displacements u_y and u_z depend only on the axial coordinate x according to the first hypothesis:

$$\begin{cases} \epsilon_{yy} = \dfrac{\partial u_y}{\partial y} = 0 \\ \epsilon_{zz} = \dfrac{\partial u_z}{\partial z} = 0 \\ \gamma_{yz} = \dfrac{\partial u_z}{\partial y} + \dfrac{\partial u_y}{\partial z} = 0 \end{cases} \tag{3.4}$$

The second hypothesis imposes that the axial displacement u_x is linear versus the in-plane coordinates [57] and therefore the whole displacement field looks like:

$$\begin{cases} u_x(x,y,z) = w_x(x) + z\theta_y(x) - y\theta_z(x) \\ u_y(x,y,z) = w_y(x) \\ u_z(x,y,z) = w_z(x) \end{cases} \tag{3.5}$$

The last hypothesis allows us to disregard shear deformations $\gamma_{xy} = \gamma_{xz} = 0$ and through the above listed equations the angles of rotation can be obtained as functions of the in-plane displacement derivatives:

$$\begin{cases} \gamma_{xy} = \dfrac{\partial u_y}{\partial x} + \dfrac{\partial u_x}{\partial y} = \dfrac{\partial w_y}{\partial x} - \theta_z = 0 \\ \gamma_{xz} = \dfrac{\partial u_x}{\partial z} + \dfrac{\partial u_z}{\partial x} = \dfrac{\partial w_x}{\partial z} + \theta_y = 0 \end{cases} \tag{3.6}$$

The end displacement field according to the Eulero-Bernoulli theory is:

$$\begin{cases} u_x(x,y,z) = w_x(x) - z\dfrac{\partial w_x}{\partial z}(x) - y\dfrac{\partial w_y}{\partial x}(x) \\ u_y(x,y,z) = w_y(x) \\ u_z(x,y,z) = w_z(x) \end{cases} \tag{3.7}$$

3.6 The St.Venant torsion

In 1885 St. Venant gave the first correct beam torsion analysis for a homogeneous linear-elastic bar.
The underlying hypothesis was that $\frac{\partial \theta_x}{\partial}$ is constant, making the warping identical in all cross-sections.
The axial strain ϵ_{xx} from torsion disappears and in all sections the distribution of the shear strains γ_{xy} and γ_{xz} is the same [58].

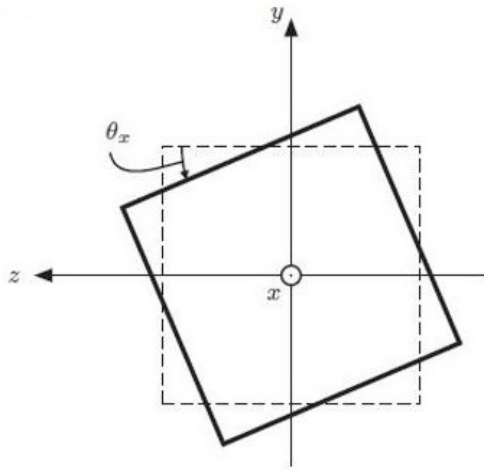

Figure 3.8: Deformation component in the torsional beam theory

For a uniform cross-sectional beam:

$$\theta_x = \frac{ML}{GI_z} \tag{3.8}$$

where:

- T is the applied torque
- L is the beam length
- G is the Modulus of rigidity (shear modulus) of the material
- I_z is the torsional constant

3.7 Constitutive relations

As state before, for our structural analysis we are going to consider an isotropic linear elastic material that is directly related to the Hooke's law.
There is therefore a relationship between stress and strain components:

$$\sigma = [C]\epsilon \tag{3.9}$$

where for isotropic materials the form of the matrix [C] looks like [57] :

$$[C] = \begin{bmatrix} C_{11} & C_{12} & C_{13} & 0 & 0 & 0 \\ C_{12} & C_{22} & C_{23} & 0 & 0 & 0 \\ C_{31} & C_{32} & C_{33} & 0 & 0 & 0 \\ 0 & 0 & 0 & C_{44} & 0 & 0 \\ 0 & 0 & 0 & 0 & C_{55} & 0 \\ 0 & 0 & 0 & 0 & 0 & C_{66} \end{bmatrix} \tag{3.10}$$

where

$$\begin{aligned} C_{11} = C_{22} = C_{33} &= \frac{E(1-\nu)}{(1+\nu)(1-2\nu)} \\ C_{12} = C_{13} = C_{23} &= \frac{\nu E}{(1+\nu)(1-2\nu)} \\ C_{44} = C_{55} = C_{66} = G &= \frac{E}{2(1+\nu)} \end{aligned} \tag{3.11}$$

At this stage it is very important to analyse what is going to do the FEM model with the structural properties we give them.
Starting from the Young modulus and the Poisson's ration, the FEM code calculates the Shear modulus G with the before written equation.
The Poisson's ratio is necessary only for the previously calculation because in the simulation itself the cross section is supposed to be rigid and therefore in this case ν is considered as 0.

3.8 FEM formulation

The FEM method was born around 1956 in the aeronautical sector because there was the necessity to have more accurate structural analysis and results for very complex shapes and geometries.
At the beginning the FEM method was rarely used because of its computational effort but as the technology goes further this method became very powerful.
The basic idea behind this method is to get an approximated solution by splitting and describing a complex problem and geometry in a easier way.
There are sever ways to get the finite element method:

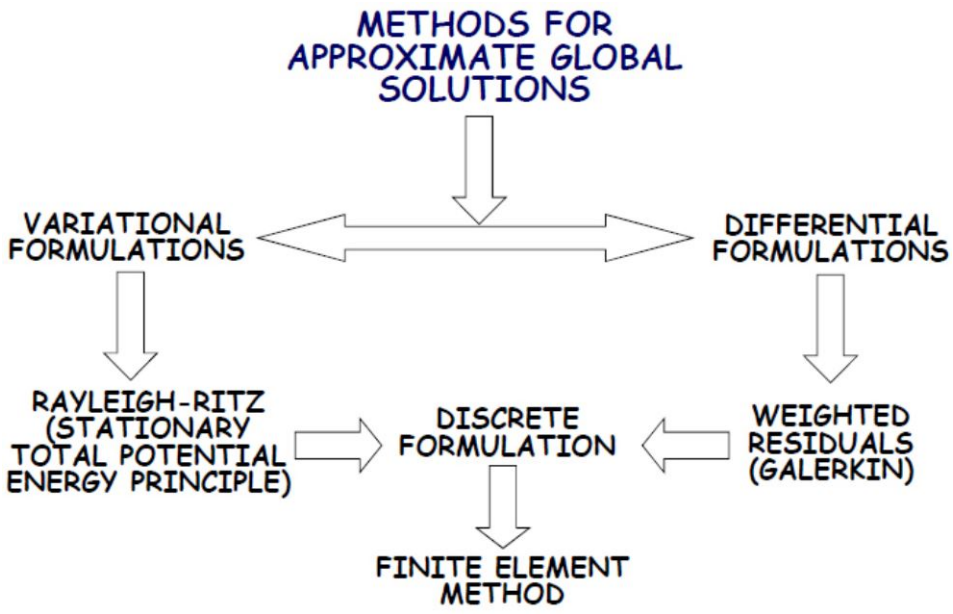

Figure 3.9: Methods for approximate global solutions

In this case we start from a variational formulation and after applying the Rayleigh-Ritz method based on the stationary of the total potential energy we get the discrete formulation on which the FEM method is based.

3.8.1 Basic Concepts of FEM Discretization

Typically, the finite element method solves differential equation-governed problems with appropriate boundary conditions.
In effect the FEM method solves the set of differential equations

$$A(u) = 0 \quad in\ \Omega \tag{3.12}$$

subjected to the boundary conditions

$$B(u) = 0 \quad in\ \Gamma \tag{3.13}$$

where A and B are matrices of differential operators defined over the analysis domain Ω and its boundary Γ and $u(x,t)$ is the vector of problem unknowns which may depend on the space dimension and the time [59].

The FEM solution is found by approximating the unknown polynomial expansions defined within each element that discretize the analysis domain Γ, i.e.

$$u \approx u_h = \sum_{i=1}^{N} N_i u_i \tag{3.14}$$

where N is the number of nodes in the mesh, N_i is the shape functions matrix and u_i are the approximate values of u at each node.
The shape functions must be linearly independent between each other and have to satisfy the geometrical boundary conditions applied to the structure.

The next step si to find the matrix system of equation.
This is obtained by substituting the expressions of strain and stresses in the energy equation of elastic deformation:

$$U_P = \frac{1}{2} \int_V \sigma^T \epsilon \, dV \tag{3.15}$$

The strains can be calculated starting from the displacements and deriving them and are therefore dependent from the derivates of the shape functions $N_i^{'}$ and the approximate node values u.

$$\epsilon = \epsilon(N_i^{'}, u) \tag{3.16}$$

The stresses can be calculated starting from the strains and applying the Hooke's law and will be also dependent from N_i and u.

$$\sigma = \sigma(N_i^{'}, u) \tag{3.17}$$

Now that we have described our energy equation (Eq.3.15) we have to take into account the work done by external forces V_P in order to get the total potential energy.

$$\Pi_P = U_P + U_P \tag{3.18}$$

At the end by using the before mentioned principle of the stationary total potential energy is possible to get N equation in the N unknowns.

$$\frac{\partial \Pi_P}{\partial u_i} = 0 \tag{3.19}$$

The resulting discrete equation system (for the static case) can be written as:

$$[K]\{u\} = \{f\} \tag{3.20}$$

where $[K]$ is the stiffness matrix, $\{u\}$ are the approximate nodal displacements and $\{f\}$ the equivalent nodal force vector [59].

3.9 Stiffness Matrix

In the previous page we introduced the stiffness matrix $[K]$ which is of basic importance in solving a structural static analysis with the FEM method.
We will first explain through a simple example how the stiffness matrix can be obtained inside the above described process and then the stiffness matrix for the 3D beam element will be calculated.

3.9.1 Stiffness matrix of a cantilever beam under constant axial load

The case under exams can be described through this picture:

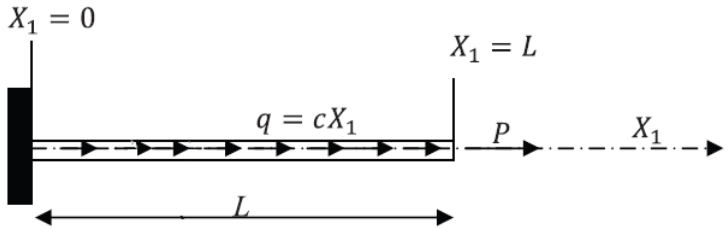

Figure 3.10: Cantilever beam under constant axial load

Let's start from the elastic energy deformation:

$$U_P = \frac{1}{2}\int_V \sigma^T \epsilon \, dV \tag{3.21}$$

Since the stress and strains are only in one direction we can write:

$$U_P = \frac{1}{2}\int_V \sigma_x \epsilon_x \, dV = \frac{1}{2}\int_V E \, \epsilon_x \epsilon_x \, dV = \frac{1}{2}\int_0^L E \, A \, (u_{,x})^2 \, dx \tag{3.22}$$

Applying the FEM discretization the displacement's derivative can be rewritten as:

$$u_{,x} = \{u\}^T \{N_{,x}\} = \{N_{,x}\}^T \{u\} \tag{3.23}$$

$$(u_{,x})^2 = u_{,x} u_{,x} = \{u\}^T \{N_{,x}\} \{N_{,x}\}^T \{u\} \tag{3.24}$$

Substituting into equation 3.22 we get:

$$U_P = \frac{1}{2}\{u\}^T \left(\int_0^L E \, A \, \{N_{,x}\} \{N_{,x}\}^T \, dx \right) \{u\} = \frac{1}{2}\{u\}^T [K] \{u\} \tag{3.25}$$

In conclusion the stiffness matrix is calculated as:

$$[K] = \int_0^L E \, A \, \{N_{,x}\} \{N_{,x}\}^T \, dx \longrightarrow K_{ij} = \int_0^L E \, A \, N_{i,x} N_{j,x} \, dx \tag{3.26}$$

3.9.2 Stiffness matrix for the 3D beam element

We have seen before how to get the stiffness matrix for an easier case than a 3D beam element. The process to get $[K]$ for bending loads and torsional moment looks similar and the resulting stiffness matrix are going to be reported in this section.
Starting from the assumption of small strains we can consider a linear problem and therefore for a 3D beam element the stiffness matrix will be a linear combination of every single effect of the applied loads. As seen in Figure 3.4 the beam element has 6 degrees of freedom for each node and is composed by 2 nodes and because of this the general stiffness matrix will be a 12x12.
Let's sum up the stiffness matrices for every single load conditions in the general one.

- **Axial load bar element**: the stiffness matrix looks like:

$$[K]^e = \frac{EA}{L/2}\begin{bmatrix} 1 & -1 \\ -1 & 1 \end{bmatrix} \tag{3.27}$$

  and is placed at this coordinates inside the 3D beam element stiffness matrix:

Axial bar	3D beam
K_{11}	K_{11}
K_{12}	K_{17}
K_{21}	K_{71}
K_{22}	K_{77}

Table 3.1: Position of axial bar stiffness elements inside 3D beam element matrix

- **Torsional load bar element**: the stiffness matrix looks like:

$$[K]^e = \frac{GJ_T}{L}\begin{bmatrix} 1 & -1 \\ -1 & 1 \end{bmatrix} \tag{3.28}$$

  and is placed at this coordinates inside the 3D beam element stiffness matrix:

Torsional bar	3D beam
K_{11}	K_{44}
K_{12}	$K_{4\ 10}$
K_{21}	$K_{10\ 4}$
K_{22}	$K_{10\ 10}$

Table 3.2: Position of torsional bar stiffness elements inside 3D beam element matrix

- **Bending beam element**: the stiffness matrix looks like:

$$[K]^e = \frac{EI_{33}}{L^3}\begin{bmatrix} 12 & 6L^{(e)} & -12 & 6L^{(e)} \\ 6L^{(e)} & 4L^{(e)2} & -6L^{(e)} & 2L^{(e)2} \\ -12 & -6L^{(e)} & 12 & -6L^{(e)} \\ 6L^{(e)} & 2L^{(e)2} & -6L^{(e)} & 4L^{(e)2} \end{bmatrix} \tag{3.29}$$

  and is placed at this coordinates inside the 3D beam element stiffness matrix:

Torsional bar	3D beam
K_{11}	$K_{2\ 2}$
K_{12}	$K_{2\ 6}$
K_{13}	$K_{2\ 8}$
K_{14}	$K_{2\ 12}$
K_{21}	$K_{6\ 2}$
K_{22}	$K_{6\ 6}$
K_{23}	$K_{6\ 8}$
K_{24}	$K_{6\ 12}$
K_{31}	$K_{8\ 2}$
K_{32}	$K_{8\ 6}$
K_{33}	$K_{8\ 8}$
K_{34}	$K_{8\ 12}$
K_{41}	$K_{12\ 2}$
K_{42}	$K_{12\ 6}$
K_{43}	$K_{12\ 8}$
K_{44}	$K_{12\ 12}$

Table 3.3: Position of beam stiffness elements inside 3D beam element matrix

  The other bending direction is also implemented inside the 3D beam general matrix in a similar way as stated before.

In the next page is presented the stiffness matrix for a 3D beam element.

$$[K] = \begin{bmatrix}
\frac{EA}{L} & 0 & 0 & 0 & 0 & 0 & -\frac{EA}{L} & 0 & 0 & 0 & 0 & 0 \\
0 & \frac{12EI_{33}}{L^3} & 0 & 0 & 0 & \frac{6EI_{33}}{L^2} & 0 & \frac{-12EI_{33}}{L^3} & 0 & 0 & 0 & \frac{6EI_{33}}{L^2} \\
0 & 0 & \frac{12EI_{22}}{L^3} & 0 & \frac{6EI_{22}}{L^2} & 0 & 0 & 0 & \frac{-12EI_{22}}{L^3} & 0 & \frac{6EI_{22}}{L^2} & 0 \\
0 & 0 & 0 & \frac{GJ_T}{L} & 0 & 0 & 0 & 0 & 0 & -\frac{GJ_T}{L} & 0 & 0 \\
0 & 0 & \frac{6EI_{22}}{L^2} & 0 & \frac{4EI_{22}}{L} & 0 & 0 & 0 & \frac{-6EI_{22}}{L^2} & 0 & \frac{2EI_{22}}{L} & 0 \\
0 & \frac{6EI_{33}}{L^2} & 0 & 0 & 0 & \frac{4EI_{33}}{L} & 0 & \frac{-6EI_{33}}{L^2} & 0 & 0 & 0 & \frac{2EI_{33}}{L} \\
-\frac{EA}{L} & 0 & 0 & 0 & 0 & 0 & \frac{EA}{L} & 0 & 0 & 0 & 0 & 0 \\
0 & \frac{-12EI_{33}}{L^3} & 0 & 0 & 0 & \frac{-6EI_{33}}{L^2} & 0 & \frac{12EI_{33}}{L^3} & 0 & 0 & 0 & \frac{-6EI_{33}}{L^2} \\
0 & 0 & -\frac{12EI_{22}}{L^3} & 0 & \frac{-6EI_{22}}{L^2} & 0 & 0 & 0 & \frac{12EI_{22}}{L^3} & 0 & \frac{-6EI_{22}}{L^2} & 0 \\
0 & 0 & 0 & -\frac{GJ_T}{L} & 0 & 0 & 0 & 0 & 0 & \frac{GJ_T}{L} & 0 & 0 \\
0 & 0 & \frac{6EI_{22}}{L^2} & 0 & \frac{2EI_{22}}{L} & 0 & 0 & 0 & \frac{-6EI_{22}}{L^2} & 0 & \frac{4EI_{22}}{L} & 0 \\
0 & \frac{6EI_{33}}{L^2} & 0 & 0 & 0 & \frac{2EI_{33}}{L} & 0 & \frac{-6EI_{33}}{L^2} & 0 & 0 & 0 & \frac{4EI_{33}}{L}
\end{bmatrix} \tag{3.30}$$

We have calculated the stiffness matrix $[K]$ for the 3D beam element that will be implemented in the static case for achieving the final displacement and in the dynamic case as part of the partial differential equation that is going to be solved, as we will see in the sext section.

3.10 Geometric Non-Linearity

Until now we have considered small strain and a linear static analysis where a linear relation holds between applied forces and displacements and where the equations of equilibrium are formulated in the undeformed state and are not updated with the deformation.
This applies in practice to structural issues where stresses stay within the linear elastic range of the material used and for those problems the stiffness matrix of the model is constant and the solving process is brief compared to a non-linear analysis on the same model [60].
If displacements, rotations, or strains become sufficiently big, consideration must be given to geometric non-linearity that take into account the difference between the original length and the deformed length of the elements.
Geometrical non-linearities are considered into the simulation by representing the strains through the Green-Lagrange strain tensor.

For example the normal strain can be written as [61]:

$$\epsilon_{xx} = \frac{\partial u_x}{\partial x} + \frac{1}{2}\left(\frac{\partial u_x}{\partial x}\right)^2 + \frac{1}{2}\left(\frac{\partial u_y}{\partial x}\right)^2 + \frac{1}{2}\left(\frac{\partial u_z}{\partial x}\right)^2 \tag{3.31}$$

while the shear strain can be calculated by [61]:

$$\epsilon_{xy} = \frac{1}{2}\left(\frac{\partial u_x}{\partial y} + \frac{\partial u_y}{\partial x} + \frac{\partial u_x}{\partial x}\frac{\partial u_x}{\partial y} + \frac{\partial u_y}{\partial x}\frac{\partial u_y}{\partial y} + \frac{\partial u_z}{\partial x}\frac{\partial u_z}{\partial y}\right) \tag{3.32}$$

In case of the non-linear analysis the following properties of the simulation changes:

- **the stiffness matrix** is not constant and has to be calculated multiple times in the course of the non linear analysis
- **the principle of superposition** is possible in the linear analysis and not possible in the non linear analysis
- **non linear analysis** is solved by Newton-Raphson technique and needs numerous iterations in each increment to achieve a converged outcome

3.11 Equations of motion

The equation of motion for a system can be derived from the classical mechanics (Newtonian mechanics) or using the energy based Lagrangian mechanics.
For a system with dumping and with more degrees of freedom the resulting partial differential equation is:

$$[M]\ddot{x}(t) + [C]\dot{x}(t) + [K]x(t) = L(t) \tag{3.33}$$

where $[M]$ is the mass matrix, $[C]$ is the dumping matrix, $[K]$ is the stiffness matrix, x are the degrees of freedom such as displacements and rotations and L are the external forces and moments.
While the mass and stiffness matrix depends from the geometrical and structural properties of the system, the dumping matrix needs to be calculated following a particular scheme that will be explained in the next section.

3.11.1 Rayleigh damping method

Introduction

Damping plays a significant role in the dynamic analysis of structures but is at the same time difficult to calculate.
For the analysis we are going to carry out in this thesis, we will consider only the structural damping inside the $[C]$ matrix since the aerodynamic damping is implicitly introduced by the CFD computed forces.

However, the most efficient way to treat damping within the context of structural analysis is to treat the damping value as an equal Rayleigh damping in the form of:

$$[C] = \alpha[M] + \beta[K] \tag{3.34}$$

where $[M]$ is above mentioned mass matrix and $[K]$ is the stiffness matrix.

This method is based on the assumption that the mass participation in structural damping decreases with increase in modes (frequency) while the stiffness matrix influence is linearly proportional to the frequency [62].
The basic equation of the Rayleigh damping method and its plot can give us a better understanding.

$$\zeta_i = \frac{\alpha}{2\omega_i} + \frac{\beta\omega_i}{2} \tag{3.35}$$

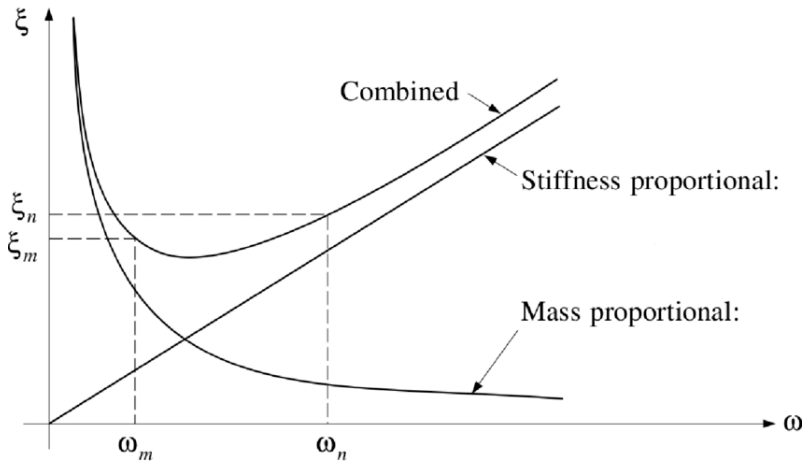

Figure 3.11: Example of Rayleigh damping method solution

Computation of coefficients for the tower

The next step will be to calculate the Rayleigh damping coefficients for our cases. For the tower we do not have any damping ratios from the input data and therefore we have to assume that the significant dynamic response of the system will die down within first four modes with damping ratios varying between 2% to 10%.
The damping rations for the second and third frequencies can be computed through:

$$\zeta_i = \frac{\zeta_4 - \zeta_1}{\omega_4 - \omega_1}(\omega_i - \omega_1) + \zeta_1 \tag{3.36}$$

and the resulting data are listed in the next page:

Mode	ω $[Hz]$	Damping ratio [%]
1	0.654	2
2	4.480	3.3
3	12.516	6.6
4	24.249	10

Table 3.4: Computed damping ratios for the tower

In the end what is needed in order to perform the structural analysis are the coefficients that are estimated using the first and the last mode data as following:

$$\beta = \frac{2\zeta_1\omega_1 - 2\zeta_m\omega_m}{\omega_1^2 - \omega_m^2} = 0.008209298 \tag{3.37}$$

$$\alpha = 2\zeta_1\omega_1 - \beta\omega_1^2 = 0.022637865 \tag{3.38}$$

Computation of coefficients for the blade

For the blade of the wind turbine the procedure is a little bit different since the first three modal damping ratios are given.
In this case we performed a best fit analysis of the given values [62].

Mode	Name	ω $[Hz]$	Damping ratio [%]
1	1st flap	1.01	1.53
2	1st edge	1.91	1.75
3	2nd flap	2.96	1.68

Table 3.5: Given damping ratios for the blade

In this approach we estimated first the coefficients using the values from mode 1 and 2:

$$\beta = \frac{2\zeta_1\omega_1 - 2\zeta_2\omega_2}{\omega_1^2 - \omega_2^2} = 0.013677321 \tag{3.39}$$

$$\alpha = 2\zeta_1\omega_1 - \beta\omega_1^2 = 0.016953765 \tag{3.40}$$

and then using modal data 1 and 3:

$$\beta = \frac{2\zeta_1\omega_1 - 2\zeta_3\omega_3}{\omega_1^2 - \omega_3^2} = 0.021873144 \tag{3.41}$$

$$\alpha = 2\zeta_1\omega_1 - \beta\omega_1^2 = 0.008854873 \tag{3.42}$$

Now the last step is to plot and compare the resulting damping ratio curves with the given log.Decrement values and select the one which best fit them.

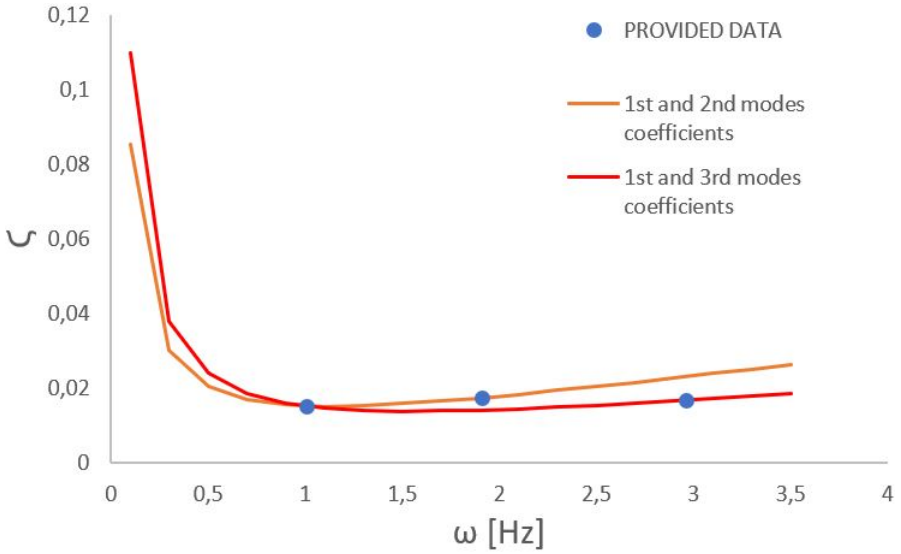

Figure 3.12: Rayleigh damping solutions for the blade

From the plot we can conclude that the curve based on the coefficients calculated from the 1st and 3rd modes better fits the given values.

3.11.2 Numerical Integration for Structural Dynamics

In order to solve the structural dynamic problem described in equation 3.33 is necessary to find a stable method to get the solution from the finite element discretization of the partial differential equation that govern our problem.
In other words we need to find a way to get $x(t)$ and $\dot{x}(t)$ at any point in time in order to solve the accelerations $\ddot{x}(t)$ in terms of the displacements, velocities, and the applied forces.

There are generally two classes of numerical integration methods :

- **explicit methods** where displacements and velocities at t_{i+1} can be determined in closed form from displacements, velocities, accelerations and external forces at the time step t_i
- **implicit methods** where displacements and velocities at t_{i+1} depend from displacements, velocities, accelerations and external forces at the time step t_i and also t_{i+1}

In this dissertation we will use an implicit scheme because of its flexibility and stability and two methods are going to be presented.

The Newmark method

The Newmark method is here presented with the three equations that allow to determine the displacement vector by solving the system of equations while complementary computations are carried out to determine velocity and acceleration vector [63].

$$\begin{cases} x_{i+1} = x_i + h\dot{x}_i + h^2\left[\left(\frac{1}{2} - \beta\right)\ddot{x}_i + \beta\ddot{x}_{i+1}\right] \\ \dot{x}_{i+1} = \dot{x}_i + h(1-\gamma)\ddot{x}_i + h\gamma\ddot{x}_{i+1} \\ [M]\ddot{x}_{i+1} + [C]\dot{x}_{i+1} + [K]x_{i+1} = L_{i+1} \end{cases} \tag{3.43}$$

The Bossak method

The Bossak method is an extension of the before explained method where the acceleration $\ddot{x}$ is taken prior the time step t_{i+1} [64].
In all cases, the method can replace the Newmark method successfully.

$$\begin{cases} x_{i+1} = x_i + h\dot{x}_i + h^2\left[\left(\frac{1}{2} - \beta\right)\ddot{x}_i + \beta\ddot{x}_{i+1}\right] \\ \dot{x}_{i+1} = \dot{x}_i + h(1-\gamma)\ddot{x}_i + h\gamma\ddot{x}_{i+1} \\ [M](1-\alpha_B)\ddot{x}_{i+1} + [M](\alpha_B)\ddot{x}_i + [C]\dot{x}_{i+1} + [K]x_{i+1} = L_{i+1} \end{cases} \tag{3.44}$$

This is the method we are going to use in our dynamic analysis because is characteristic of a good damping in high frequencies range and less sensible to the wrong choice than other methods [64].

3.12 Verification

Right now we have deeply described our structural model in each of its properties. The last step before moving on to the aerodynamic model is to ensure that the FEM code is actually implementing the structural model we have described and that it is consistent with the well known analytical solutions.
In this section 3 different structural responses are going to be validated.

3.12.1 Bending static

Let us consider a cantilever, rectangular cross-section beam with the following properties, made of an isotropic material and loaded at the center point of the free tip (x=L) by a force F_y.

Property	Value
base length	0.2 m
height length	0.1 m
Young modulus (E)	7.00 E+10 Pa
I_1	1.67 E-05 m^4
length	10 m
ρ	7850 kg/m^3
F_y	1000 N

Table 3.6: Beam properties and loads for static bending analysis

The aim of the validation is to calculate the analytical vertical free tip displacement (v) of the free end of the beam via the integration of the equation:

$$\frac{\partial^2 v}{\partial x^2} = \frac{M(x)}{EI_1} \longrightarrow v_1|_{x=L} = \frac{F_y}{EI_1}\left(\frac{Lx^2}{2} - \frac{x^3}{6}\right) = 0.285714\ m \tag{3.45}$$

and compare it with the displacement (v) computed trough the FEM analysis with different meshes and with linear and non linear methods.
This first table report the FEM results for the linear analysis where only the vertical displacement has been taken into account because, as stated before, in geometrical linearity the beam itself doesn't stretch along its span axis.

The last column outline the relative error of the FEM compared to the analytical solution calculated through:

$$\epsilon_{rel} = \left(\frac{v_1|_{x=L} - v_{FEM}|_{x=L}}{v_1|_{x=L}}\right) \tag{3.46}$$

MESH [elements]	v_{FEM} [m]	ϵ_{rel}[%]
1	0.285144	-0.20
10	0.285144	-0.20
100	0.285144	-0.20
1000	0.285144	-0.20

Table 3.7: Static bending results for linear analysis

We can see that the number of nodes doesn't affect the resulting tip displacement because the exact/analytical theory is the same that has been implemented inside the FEM code.
Moreover the obtained results agree with the analytical ones with very small relative errors.

Let's take a look at the non linear analysis data by giving particular attention to the displacements in both directions since we expect that the beam deflects but also compress itself.

MESH [elements]	v_{FEM} [m]	ϵ_{rel} [%]	w_{FEM} [m]
1	/	/	/
10	0.284906	-0.28	-0.00486132
100	0.284906	-0.28	-0.00487133
1000	0.284906	-0.28	-0.00487133

Table 3.8: Static bending results for non-linear analysis

For this second step of analysis we have some different results as expected.
First of all for this kind of computations is not possible to have only one element mesh because geometrical non-linearities cannot be described.
Secondly we can see how the vertical displacement is lower than expected by a very tiny percentage and the beam, due to non-linear behaviour, compress itself a little bit.

3.12.2 Bending modes

After have ensured that the beam deflect as expected under a given and known load, in this chapter we want to test if the bending modes or eigenfrequencies of a given beam corresponds to the one calculated in trusted and analytical ways.

Let us consider for this purpose a cantilever, rectangular cross-section beam with the following properties and made of an isotropic material.

Property	Value
base length	0.56 m
height length	0.2 m
Young modulus (E)	7.00 E+10 Pa
I_1	3,73E-04 m^4
I_2	2,93E-03 m^4
length	10 m
ρ	2700 kg/m^3

Table 3.9: Beam properties for bending modes analysis

For this purpose we have used the results given by [65] and have compared them with the one given by the FEM code by a mesh of 100 elements.

Bending mode	Theory [Hz]	FEM [Hz]	ϵ_{rel} [%]
1	1.645	1.63768	0.44
2	10.3039	10.2632	0.39
3	28.8664	28.8664	0
4	56.5661	56.3133	0.45
5	93.509	93.0898	0.45

Table 3.10: Eigenfrequencies for linear analysis

Also per the eigenfrequencies estimate we can conclude that the FEM code is consistent.

3.12.3 Torsional static

The last section in this chapter is also the last comparison between the Kratos code and analytical results in order to verify the accuracy and reliability of the used FEM tool.

In order to do that an isotropic cantilever, rectangular cross-sectional beam is used whose characteristics are:

Property	Value
base length	0.2 m
height length	0.1 m
Young modulus (E)	7.00 E+10 Pa
Shear modulus (G)	2.713 E+10 Pa
J	0.01 m^4
length	2 m
ρ	7850 kg/m^3
M_t	10 Nm

Table 3.11: Beam properties for torsional static analysis

The theory give as a formulation in order to calculate the torsional angle along the span:

$$\phi = \frac{M_t L}{JG} \longrightarrow \phi|_{x=L} = 7,3714^\circ \tag{3.47}$$

The FEM code gave as result : $\phi|_{x=L_{FEM}} = 7,3714^\circ$

We can conclude that the code is also validated for the torsion of the beam.

Chapter 4

Aerodynamic modelling

In this chapter we will analyse the second fundamental simulation tool in order to perform our aeroelastic analysis, the CFD solver.
After introducing the Navier-Stokes equations for fluid dynamics, we will analyse how those are averaged for the unsteady flow (URANS) by the utilised CFD solver FLOwer and which settings our computational model is going to have.

4.1 Conservation Laws

Balancing fluxes over a control volume provides us with conservation laws for the mass, momentum and energy of the lump of fluid that is at time t surrounded by this control volume.
For notation convenience, the dynamic viscosity coefficient μ has been extracted from the second order shear stress tensor $\bar{\bar{\tau}}$, which holds all throughout this text [66].

$$\begin{cases} \dfrac{\partial \rho}{\partial t} + div\rho(\vec{V} - \vec{V_b}) = 0 \\ \dfrac{\partial \rho \vec{V}}{\partial t} + div\left(\rho\vec{V} \times (\vec{V} - \vec{V_b}) + p\bar{\bar{I}} - \mu\bar{\bar{\tau}}\right) + \vec{\omega} \times \rho\vec{V} = \vec{0} \\ \dfrac{\partial \rho E}{\partial t} + div\left(\rho H \times (\vec{V} - \vec{V_b}) - \mu\bar{\bar{\tau}} \cdot \vec{V} - K\ \overrightarrow{grad}\ T\right) = 0 \end{cases} \tag{4.1}$$

The specific internal energy e, when augmented by the pressure over the density, gives the specific enthalpy h. When added to the specific kinetic energy, these two become respectively specific total energy E and specific total enthalpy H [66].

$$H = E + \frac{p}{\rho} = h + \frac{V^2}{2} = e + \frac{p}{\rho} + \frac{V^2}{2} \tag{4.2}$$

4.2 CFD solver FLOWer

4.2.1 Introduction

The fluid dynamic simulations are carried out by employing the block-structured CFD solver,FLOWer [50], from the German Aerospace Center (DLR).
The FLOWer code solves the compressible, three-dimensional Reynolds-Averaged Navier-Stokes equations (URANS) and in the recent years has been continuously developed at the Institute of Aerodynamics and Gas Dynamics (IAG) - University of Stuttgart for wind turbine applications [67].

4.2.2 Grid generation and motion

In order to perform a CFD case study is necessary to know and create the geometry of the analysed body and to generate the grid domain through which the flow passes. For this thesis the software named Pointwise and an academic tool were used for the purposes.
Another important aspect that will be described in this section is how the different grids (MULTIGRID) are matched together (CHIMERA) and how they can move with respect to the others using this method.

Pointwise

As mentioned before, Pointwise was the choice for computational fluid dynamics meshing.
This software enables to cover all aspects of preprocessing from importing or creating the model to flow solver export [68].
By generating the structured mesh, a lot of parameters and levels of control are available and the program is also capable of creating simple geometries like cylinders and block.
Later will be described in detail the settings parameters for the mesh for every single part of the wind turbine.

4.2.3 Background generator

Starting from the local mesh around the wind turbine component, a background grid is generated through this academic code by giving a few detail of the expected result.
The program needs the 3D dimensions of the background block, the smallest cell size and a coarsening level for the mesh .
Using this tool permits to save time and at the same time have a very detailed and efficient mesh around the body.

Chimera

The Chimera-technique has been introduced by Benek et al. in 1983 [69].The idea of the Chimera-technique is to use overlapping grids to discretize the computational domain as the next example of a 2D airfoil shows.

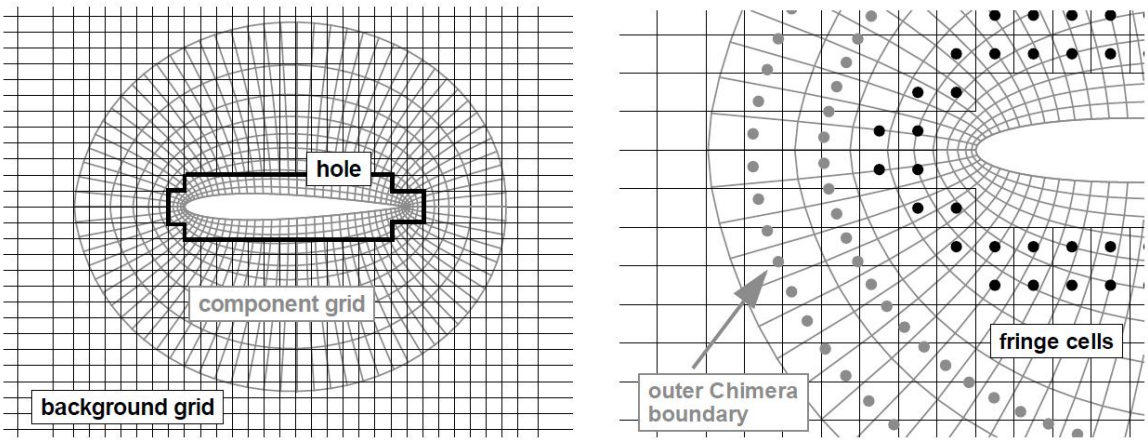

Figure 4.1: Overlapping grid system for 2D airfoil

In the left picture of Figure 4.1 is shown how the grid around the airfoil is embedded into another grid.
Grids around solid bodies are often called 'component grids' or 'near field grids'.
The component grids may be embedded into other component grids, or into a background grid, which is only used to cover the outer areas of the computational domain.
In Figure 4.1, left, some points of the background grid fall inside the airfoil. These points can not be discretized and are therefore blanked and excluded from the flow calculation.
In order to establish intergrid communication during the solution process, the grid points at the grid boundaries and close to blanked points are updated with interpolated flow data from an overlaying grid, see Figure 4.1, right.

The Chimera technique has two major advantages for grid generation:

- grids associated with moving bodies move with the bodies without stretching or distorting the grids.
- the grid generation for complex geometries is simplified. This is achieved by breaking down the geometry into simple shaped components, for which individual grids can easily be created.

4.2.4 Spatial discretization scheme

The approximation of the governing equations follows the method of lines, which decouples the discretization in space and time. The spatial discretization is based on a finite volume method which subdivides the flow field into a set of non-overlapping hexahedral cells. The equations of change are applied on each cell in integral form, which ensures the treatment of the equations in conservative form [70].
Through the application of the integral form of the Navier-Stokes equations, a discrete flux balance is obtained for each control volume, which can be used to approximately determine the change of flow quantities with respect to time in particular points.
In FLOWer the cell-vertex and the node-centered approaches are realized, in which the flow variables are associated with the vertices of the cell [70]. The spatial discretization leads to an ordinary differential equation for the rate of change of the conservative variables in each grid point:

$$\frac{\partial}{\partial t}\vec{W}_{i,j,k} = -\frac{1}{V_{i,j,k}}\left(\vec{R}^{\,c}_{i,j,k} - \vec{R}^{\,v}_{i,j,k}\right) \tag{4.3}$$

where $\vec{R}^{\,c}_{i,j,k}$ and $\vec{R}^{\,v}_{i,j,k}$ represent the approximation of the inviscid and viscous net flux of mass, momentum and energy for a particular control volume arrangement with volume surrounding the grid node (i,j,k).
In the simulation computed for this thesis the second order Jameson-Schmidt-Turkel (JST) [71] scheme is implemented while for the background of the full model simulation a WENO scheme according to Shu [72] with a fifth order spacial accuracy is used.

4.2.5 Time integration scheme

FLOWer is able to compute steady as unsteady simulations. While for the steady one the hypothetical time step has an infinite value, for unsteady computations a time integration scheme is therefore necessary.
The algorithms for computing unsteady flows are of two main types, explicit and implicit.
In FLOWer you have the choice between two explicit and one implicit scheme [70]. Explicit methods are subjected to severe stability restrictions through the CFL condition and to guarantee stability to the method a very small time step could be necessary.

An implicit discretization of the problem helps to bypass the time step limitation of explicit schemes. Jameson has developed a very efficient multigrid-driven implicit approach for the solution of the unsteady Euler equations [73] called „the dual-timestepping method“.
Using central differences in space and an implicit multistep discretization in time, a large set of simultaneous non-linear equations is formed and marched to steady-state in pseudo-time through a multigrid algorithm within each physical time step.
Following Jameson, the DLR multi-block code FLOWer has been extended to the solution of unsteady viscous flows [73].

If we discretize the time derivative term with a backwards difference second order accurate operator [70], we obtain (drop the i,j,k subscripts for clarity) :

$$\frac{3\vec{W}^{n+1}}{2\Delta t} - \frac{2\vec{W}^{n}}{\Delta t} + \frac{\vec{W}^{n-1}}{2\Delta t} + \vec{P}(\vec{W}^{n+1}) = 0 \tag{4.4}$$

This equation for $\vec{W}^{n+1}$ is non-linear due to the presence of the term $\vec{P}(\vec{W}^{n+1})$ and cannot be solved directly.
For an iterative solution, Jameson modifies eq. (4.4) in a very skilful manner by integrating the modified equation in a fictitious pseudo time:

$$\frac{d}{d\tau}\vec{W} + \vec{P}^{\tau}(\vec{W}) = 0 \tag{4.5}$$

with the altered residual

$$\vec{P}^{\tau}(\vec{W}^{v}) = \frac{3\vec{W}^{v}}{2\Delta t} - \frac{2\vec{W}^{n}}{\Delta t} + \frac{\vec{W}^{n-1}}{2\Delta t} + \vec{P}(\vec{W}^{v}) \tag{4.6}$$

The integration of the system of eq. (4.4) for each physical time step can be carried out using the same techniques as for the steady case. Performing a number of subiterations (counter v), a pseudo steady state is reached:

$$\tau \rightarrow \infty \Rightarrow \frac{d}{d\tau}\vec{W} \rightarrow 0, \ \vec{W}^{v} \rightarrow \vec{W}^{n+1} \tag{4.7}$$

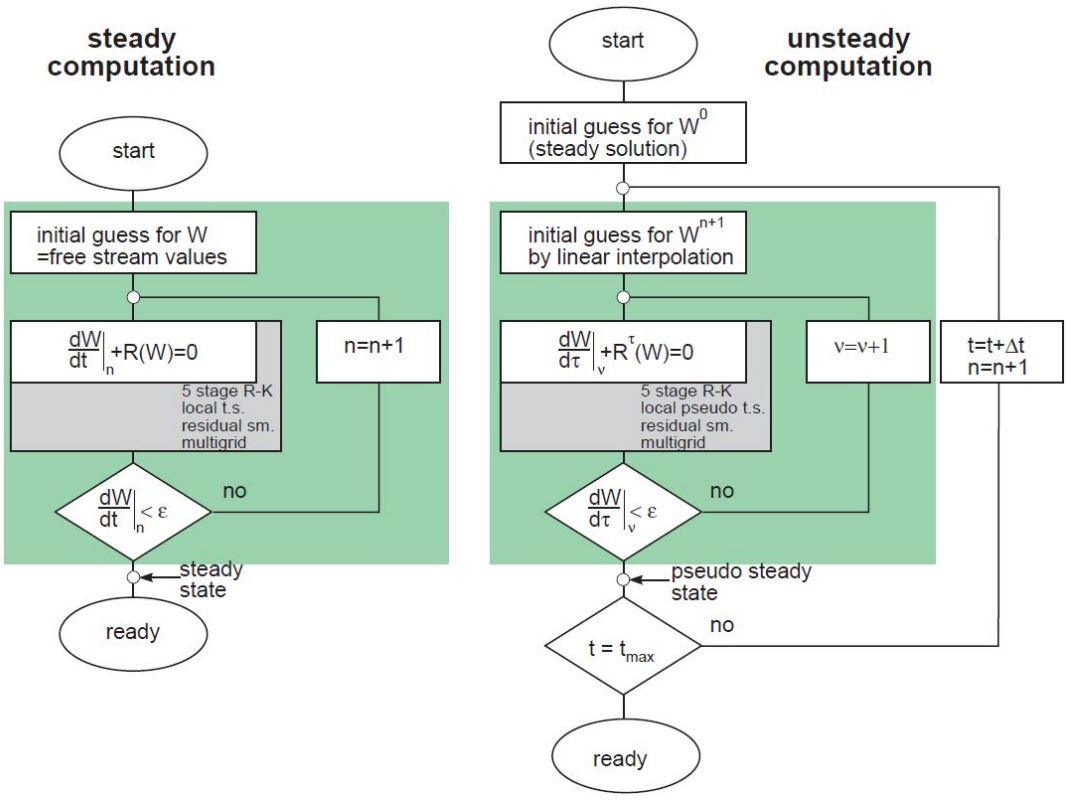

Figure 4.2: Computational methods

4.2.6 Turbulence model

In this subsection we deal with specific details of the Reynolds-averaged Navier-Stokes system of equations and with turbulence models
Simulating the genuine viscous turbulent flow still resorts to expensive DNS techniques.
Instead, the (statistical) Reynolds averaging is applied to the original Navier-Stokes system of equations (4.1).
Let us denote by $< \cdot >$ this averaging operator applied to a quantity φ:

$$< \varphi > (\vec{x}, t) = \lim_{N \to \infty} \frac{1}{N} \sum_{i=1}^{N} \varphi_i(\vec{x}, t) = \frac{1}{T} \int_{t-T/2}^{t+T/2} \varphi_i(\vec{x}, \tau) d\tau \tag{4.8}$$

all quantities meet the ergodicity assumption which means that a statistical average can only be equal to a time average when the integration time interval T is supposed to be large enough with respect to the turbulence time scales and small enough with respect to the macroscopic time scales of the flow [66].
Signals are then decomposed into their mean component $< \varphi >$ and their fluctuation part φ':

$$\varphi =< \varphi > +\varphi' \tag{4.9}$$

By substituting the decomposition into the initial Navier-Stokes equations we get a more complex partial differential equation system.

For the sake of clarity, the average notations are from now on left out in order to recover the same symbols as reported at the beginning of this chapter, that is: all *latin* and *greek* characters refer to mean flow quantities with the exception of k, $\bar{\bar{\tau}}_R$ and $\vec{q}_t$.
However, this time, both the total energy and the total enthalpy not only include the mean flow kinetic energy $V^2/2$ but also the turbulence kinetic energy k (by the way well deserving being termed total energy and total enthalpy) [66]:

$$E^* = e + \frac{1}{2}V^2 + k \; and \; H^* = h + \frac{1}{2}V^2 + k \tag{4.10}$$

The final system of equations, from which turbulence modelling is further developed reads:

$$\begin{cases} \dfrac{\partial \rho}{\partial t} + div \rho \vec{V} = 0 \\ \dfrac{\partial \rho \vec{V}}{\partial t} + div \left(\rho \vec{V} \times \vec{V} + p \bar{\bar{I}} \right) = div(\mu \bar{\bar{\tau}} + \bar{\bar{\tau}}_R \Big) \\ \dfrac{\partial \rho E^*}{\partial t} + div \rho \vec{V} \left(E^* + \frac{p}{\rho} \right) = div((\mu \bar{\bar{\tau}} + \bar{\bar{\tau}}_R) \cdot \vec{V} - \vec{q} - \vec{q}_t) \end{cases} \tag{4.11}$$

It is now a matter of modelling $\bar{\bar{\tau}}_R$ and $\vec{q}_t$.

Boussinesq's Assumption

Higher order turbulence models are based on transport equations for each of the Reynolds correlations (the entries of $\bar{\bar{\tau}}_R$) that are solved simultaneously to the mean flow equations, at the price of an increased model complexity and of much larger computation times.
This is bypassed thanks to lower order approaches that make use of the Boussinesq's assumption [66]. This one relates the turbulence new terms $\bar{\bar{\tau}}_R$ and $\vec{q}_t$ to the gradients of the mean flow, by means of relations similar to their "laminar" counterparts for $\bar{\bar{\tau}}$ and $\vec{q}$:

$$\begin{cases} \bar{\bar{\tau}} = -\dfrac{2}{3}\mu \; div\vec{V}\bar{\bar{I}} + \mu\left(\overline{\overline{grad}}\;\vec{V} + \;{}^t\overline{\overline{grad}}\;\vec{V}\right) \\ \vec{q} = -\dfrac{\mu_t \; c_p}{Pr}\;\overrightarrow{grad}\;T \end{cases} \tag{4.12}$$

induce with the help of an eddy viscosity coefficient μ_t and of a turbulence Prandtl number Pr_t:

$$\begin{cases} \bar{\bar{\tau}} = -\dfrac{2}{3}\mu \; div\vec{V}\bar{\bar{I}} + \mu\left(\overline{\overline{grad}}\;\vec{V} + \;{}^t\overline{\overline{grad}}\;\vec{V}\right) \\ \vec{q} = -\dfrac{\mu_t \; c_p}{Pr}\;\overrightarrow{grad}\;T \end{cases} \tag{4.13}$$

The system to be solved reads in the end:

$$\begin{cases} \dfrac{\partial \rho}{\partial t} + div\rho\vec{V} = 0 \\ \dfrac{\partial \rho\vec{V}}{\partial t} + div\left(\rho\vec{V}\times\vec{V} + p\bar{\bar{I}} - (\mu+\mu_t)\bar{\bar{\tau}}\right) = \vec{0} \\ \dfrac{\partial \rho E}{\partial t} + div\left(\rho\vec{V}H - (\mu+\mu_t)\bar{\bar{\tau}}\vec{V} - c_p\left(\dfrac{\mu}{Pr} + \dfrac{\mu_t}{Pr_t}\right)\overrightarrow{grad}\;T\right) = 0 \end{cases} \tag{4.14}$$

where $E^* \equiv E$ and the turbulence Prandtl number is always set to $Pr_t = 0.9$ since we only address turbulence.

Now turbulence models help evaluate k and μ_t.

$k-\omega$ Type Models

For the the $k-\omega$ Type Models, 2-transport equation models set the eddy viscosity to:

$$\mu_t = C_\mu \frac{\rho k}{\omega} \tag{4.15}$$

where the function of the flow C_μ has no dimension and $[\omega] = T^{-1}$.

Two transport equations are provided for the turbulence kinetic energy k and for ω:

$$\begin{cases} \dfrac{\partial \rho k}{\partial t} + div\left(\rho k \vec{V} - \left(\mu + \dfrac{\mu_t}{\sigma_k}\right) \overrightarrow{grad}\ k\right) = S_k \\ \dfrac{\partial \rho \omega}{\partial t} + div\left(\rho \omega \vec{V} - \left(\mu + \dfrac{\mu_t}{\sigma_\omega}\right) \overrightarrow{grad}\ \omega\right) = S_\omega \end{cases} \tag{4.16}$$

where the numerical constants of the diffusion terms σ_k and σ_ω stand without dimensions and are usually identical for all models [66]. The source terms S_k and S_ω are again split into production and destruction terms according to:

$$\begin{cases} S_k = P_k - D_k \quad [S_k] = ML^{-1}T^{-3} \\ S_\omega = P_\omega - D_\omega \quad [S_\omega] = ML^{-3}T^{-2} \end{cases} \tag{4.17}$$

and the production/destruction pairs read:

$$\begin{cases} P_k = \mu_t S - \dfrac{2}{3}\rho k\ div\ \vec{V} \\ D_k = \beta_k\ \rho k \omega \end{cases} \tag{4.18}$$

$$\begin{cases} P_\omega = \beta_{\omega 1} P_k \dfrac{\omega}{k} \\ D_\omega = \beta_{\omega 2}\ \rho \omega^2 \end{cases} \tag{4.19}$$

The strain rate invariant is hereby denoted by S and carries the dimensions of the square of a velocity space derivative, that is $[S] = T^{-2}$. Also, the additional functions of the flow
$\beta_k, \beta_{\omega 1}$ and $\beta_{\omega 2}$ are dimensionless.
The various $k-\omega$ type models implemented in FLOWer differ only in the definition of the coefficients:

$$C_\mu,\ \beta_k,\ \beta_{\omega 1}\ and\ \beta_{\omega 2} \tag{4.20}$$

In this thesis the turbulent closure of the URANS equations is provided by the before explained eddy viscosity two-equation shear stress transport (SST), $k-\omega$ model because is known for improved prediction of flows with strong adverse pressure gradients and separation.

Chapter 5

Aeroelastic model

5.1 Introduction

In this chapter the main and most important part of this thesis is described where the settings and the results of the aeroelastic study are presented and discussed.
We will first focus on how the structural properties, structural mesh and reference section of the tower and blade are selected.
Afterwards we will introduce the mesh and solver settings for the CFD analysis and at the end the solutions of the one way and two way coupling.

5.2 One way coupling tower

5.2.1 Analysis of structural data and interpolation scheme

Before setting up the fluid dynamic simulation is important to know on which section of the tower our CFD code needs to compute forces and which structural properties do have the element of the FEM analysis, starting from the nodal values.
In order to do that we got from the data project the first 4 bending eigenfrequencies. Therefore we have calculate with different structural data interpolation methods our modal shape frequencies and we have compared them with the original ones in order to find out which one is the closest.
The question is now which property we assign to the element having two different values at its nodes.

Three different methods have been used for this purpose:

- **backward scheme** where the property of the second node is taken:

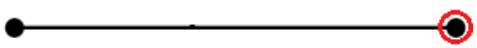

Figure 5.1: Backward scheme node

- **forward scheme** where the property of the first node is taken:

Figure 5.2: Forward scheme node

- **central different scheme** where the mean value of the nodes is taken:

$$f_{element_i} = \frac{f_{node_i} + f_{node_{i+1}}}{2} \tag{5.1}$$

The material and structural properties of the tower looks like:

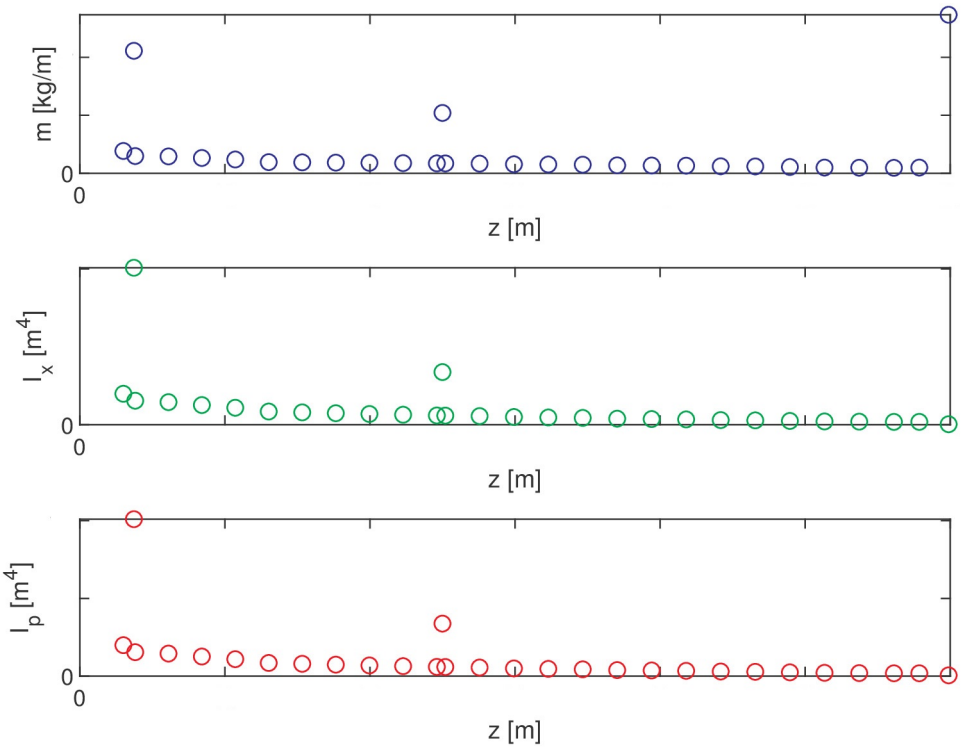

Figure 5.3: Starting properties of the tower

It is important do underline how these 3 methods have been applied only to the central part of the tower while for the basement and the nacelle respectively a forward scheme and a backward scheme have been used in order to preserve their mass and stiffness.
In the previous chapter has been stated that the tower has axis symmetrical properties and for this reasons only bending modes in one direction will be reported in the next table.

The last column of the results in the next table shows the mean relative error for every applied method estimated through:

$$\epsilon_{rel} = \sum_{i=1}^{4} \left(\frac{f_{FEM_i} - f_{REFERENCE_i}}{f_{REFERENCE_i}} \right) \tag{5.2}$$

Method	1st mode [Hz]	2nd mode [Hz]	3rd mode [Hz]	4th mode [Hz]	$\epsilon_{rel}[\%]$
WINSENT	a	b	c	d	/
centered	a1	b1	c1	d1	3.81
backward	a2	b2	c2	d2	2.00
forward	a3	b3	c3	d3	2.17

Table 5.1: Eigenfrequencies TOWER analysis

We can conclude that the backward scheme is the more accurate for our goals and moreover the structural properties will be set into the FEM code according to this result.

5.2.2 Tower CFD model

In order to perform the CFD analysis the computational domain needs to be divided according to a volume mesh.
The CFD code build up the domain putting together many blocks, the tower mesh block and the background mesh block.

Mesh and boundary conditions

First of all the cylindrical surface of the tower has been created in POINTWISE with those geometrical characteristics:

Tower bottom radius [m]
Tower top radius [m]
Tower height [m]

Table 5.2: Tower geometrical properties

In order to set the mesh parameters like $y+$ is necessary to decide the boundary conditions of the simulation:

Wind speed	6.1 m/s
Reference length [top tower chord]	2.5 m
Density	1.231 kg/m^3
Dynamic viscosity	1.789E-05 $N \cdot s/m^2$
Reynolds number	1.04E+06
y ($y+ = 1$)	5.62E-05 m

Table 5.3: Simulation settings for the tower

We are now able to set the O-type mesh topology parameters taking into account to impose a wall distance lower than the one computed before.

y ($y+ < 1$)	2.9E-05 m
Growth rate	1.10
Horizontal distance from the tower	11.15 m
Vertical distance from the tower	11.15 m
Boundary condition on the surface	non-slip wall
Number of cells	3870720

Table 5.4: Mesh settings for the tower

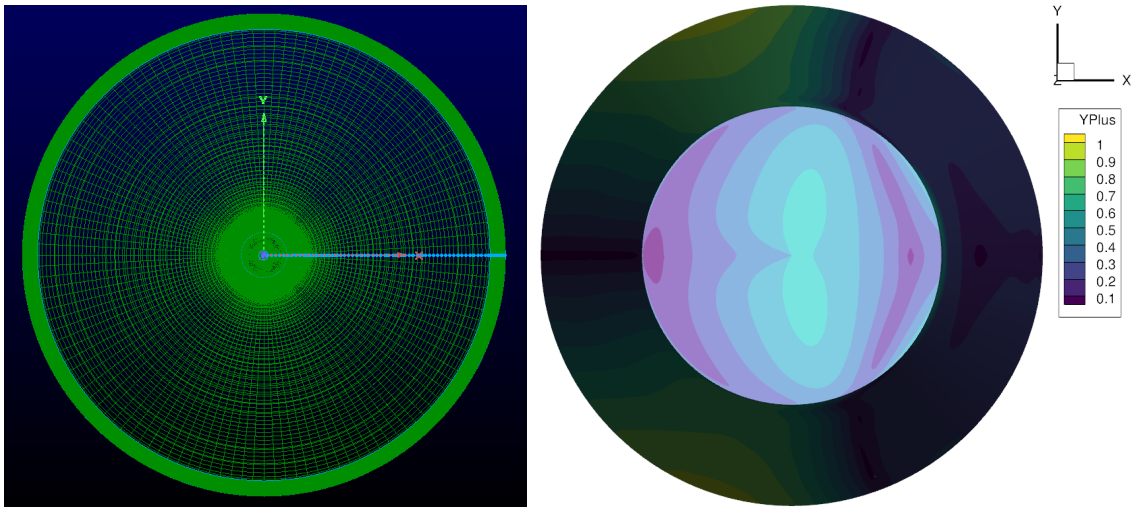

(a) Mesh tower top

(b) y+ tower top

Figure 5.4: Top view O-type mesh topology and y+ values

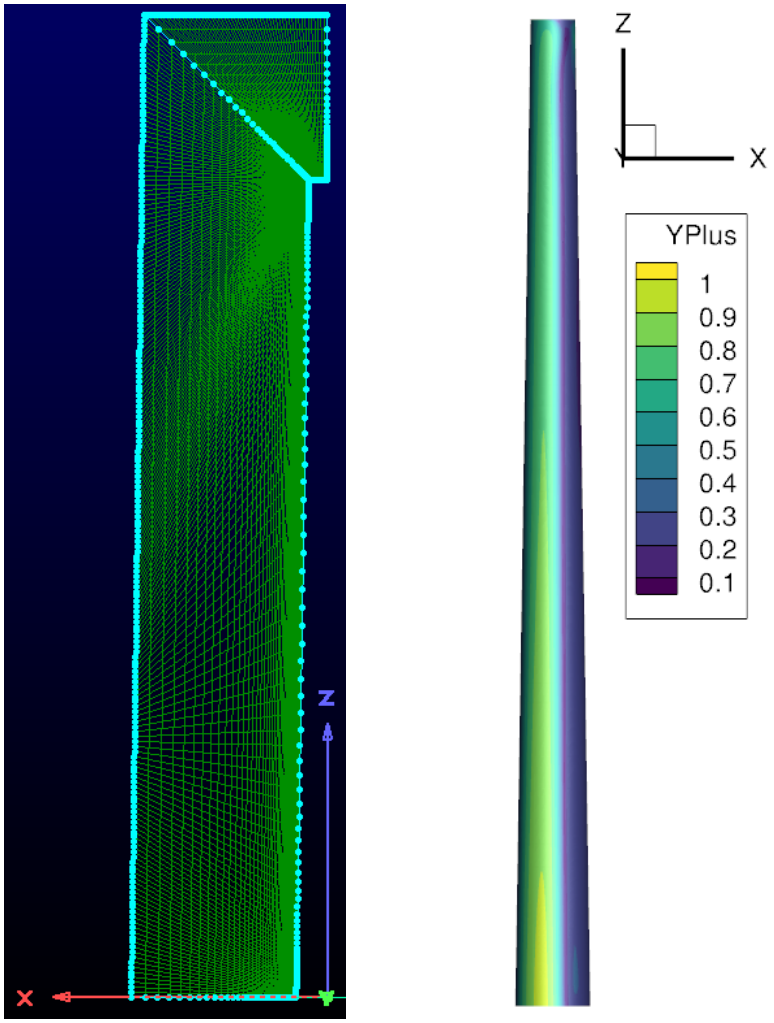

(a) Mesh tower side

(b) y+ tower side

Figure 5.5: Side view O-type mesh topology and y+ values

Once we have defined the mesh around the tower it's time to create the background using the before mentioned tool and the next parameters:

Height of the domain	$4 \cdot$ *Rotor diameter*
Width of the domain	$8 \cdot$ *Rotor diameter*
Length of the domain	$10 \cdot$ *Rotor diameter*
Minimum spacing (CHIMERA region)	0.25 m
Boundary condition on the ground	EulerWall
Boundary condition on the outer surface	Farfield
Number of cells	1515520

Table 5.5: Mesh settings for the tower-background

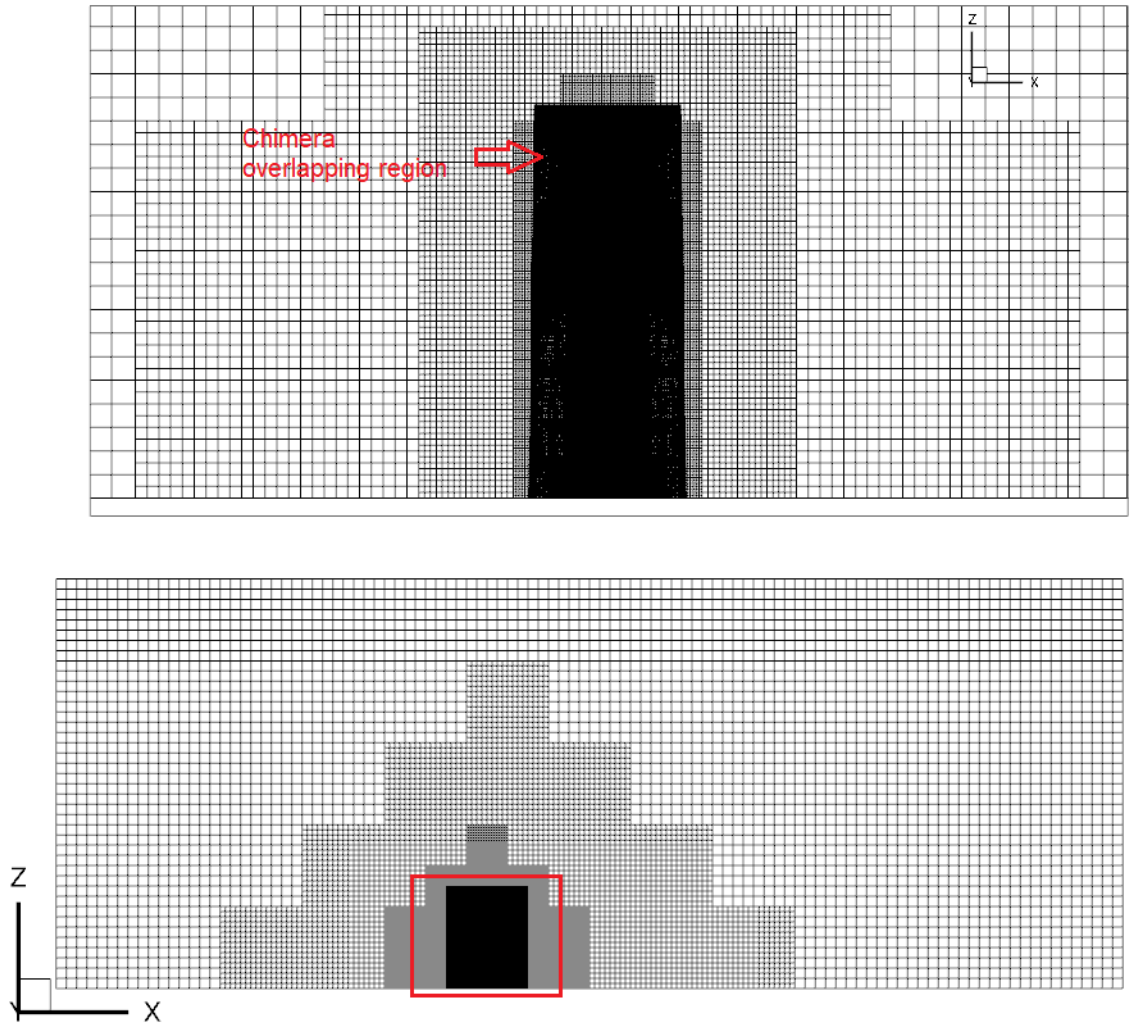

Figure 5.6: Background mesh for tower simulation

The Chimera interpolation method was applied in the overlapping area between the meshes.

CFD settings

Once the computational domain is created, the next step is to set the solver.
In the previous chapter we have described the solver setting that are also valid for this one with the only exception for the spatial discretization scheme:

CFD code	FLOWer (IAG-DLR)
Equations	URANS
Spatial discretization scheme for the FULL MODEL background	WENO (5th order accurate)
Spatial discretization scheme for other volumes	Jameson-Schmidt-Turkel (2nd order accurate)
Time integration scheme	explicit hybrid 5-stage Runge-Kutta (central discretization)
Turbulence model	$k-\omega$ SST

Table 5.6: CFD solver settings

In order to perform the CFD simulation and obtain a converged solution the following strategy has been used:

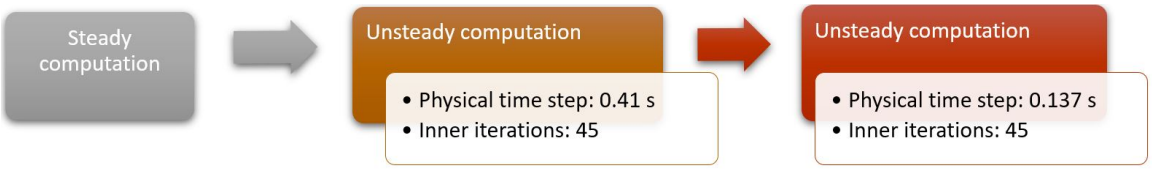

Figure 5.7: Solution strategy

The basic idea is to let converge the steady solution in order to have a basic and starting configuration for the unsteady process which is necessary to be performed in order to capture the unsteady effect of the flow around a tower of finite length placed on one side on a flat plate.

Inside the unsteady simulation two parameters needs to be defined:

- **physical timestep** that represents the real time that experiences a flow particle inside the domain. In the first step the time value is the one required by a fluid particle to travel from the upstream to downstream of the top of the tower. In the second and last step the time is 1/3 of the previous one.
- **Inner iterations** represents the number of iteration that the code perform in order to achieve a pseudo steady state for every single timestep.

One the set up of the code is ended and the simulation reaches a converged and "steady" solution the results can be analysed.

Results

First of all is necessary to ensure the convergence of the simulation by looking at the residuals and the force coefficients.

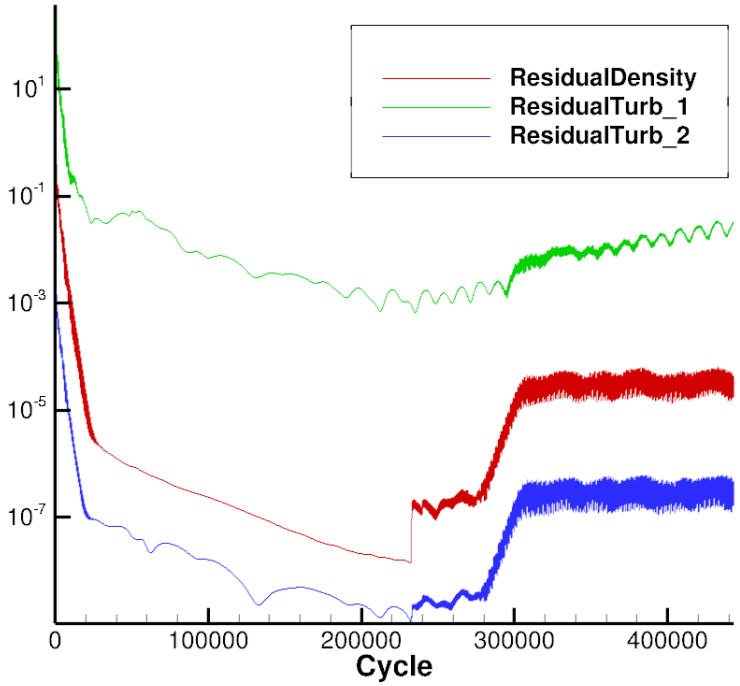

Figure 5.8: Residuals

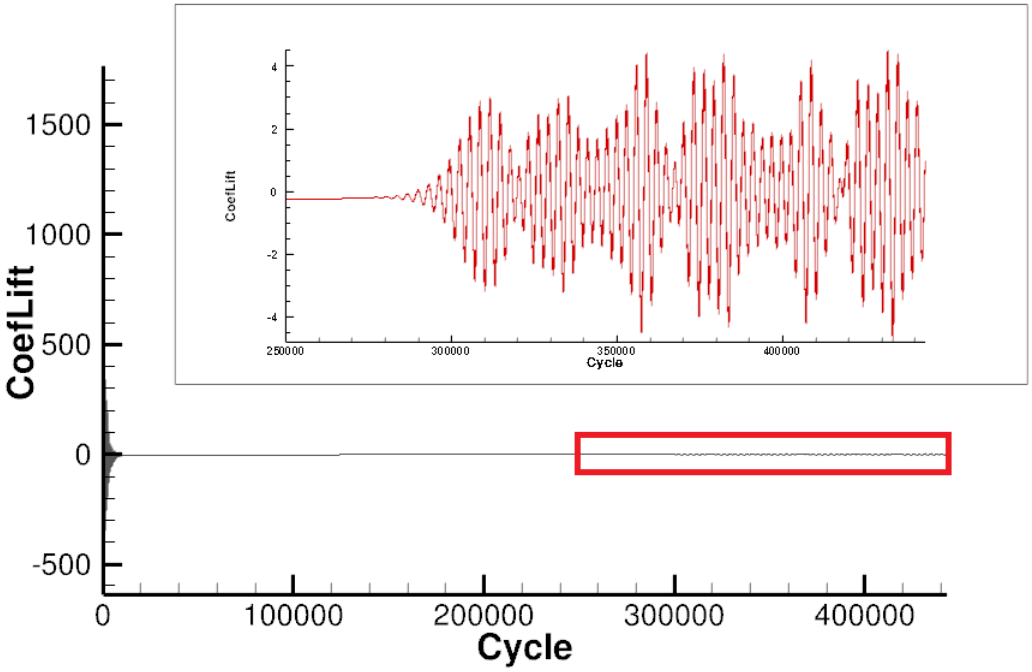

Figure 5.9: Lift coefficient values

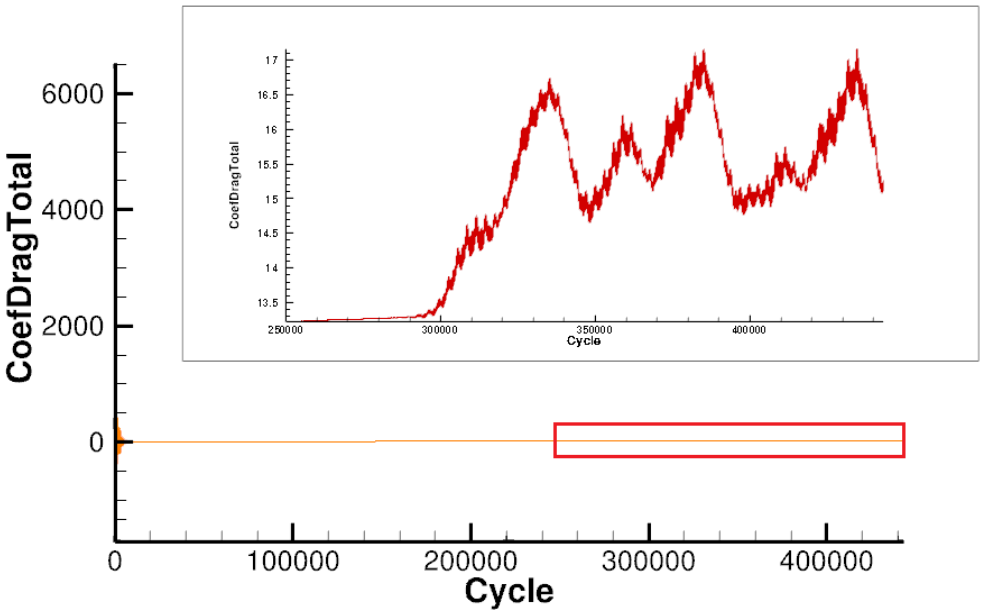

Figure 5.10: Drag coefficient values

From Figure 5.10 is clearly to see how the switch between steady and unsteady computation has increased the residuals due to the more complex flow to describe but at the same time confirm the necessity to analyse in that way this case.
By looking at Figure 5.9 and Figure 5.10 we can conclude that the flow has an unsteady behaviour along the lift direction (z-axis) and the drag direction (x-axis) because the forces coefficients change in time and therefore is necessary to analyse more in detail which phenomena occur.

Our investigation of the flow around a tower starts by looking at a simpler case like a flow around a cylinder of infinite length.

The Reynolds number of our test case is $1.04E+06$ and therefore we expect to have a fully turbulent wake with the beginning of a vortex sheet.
In the literature some experimental analysis have been made over the years and one interesting investigation on 3D wake structures for flow over a wall-mounted short cylinder was performed.
In order to check and compare the fluid dynamic around the tower some CFD visualization tools have been used.

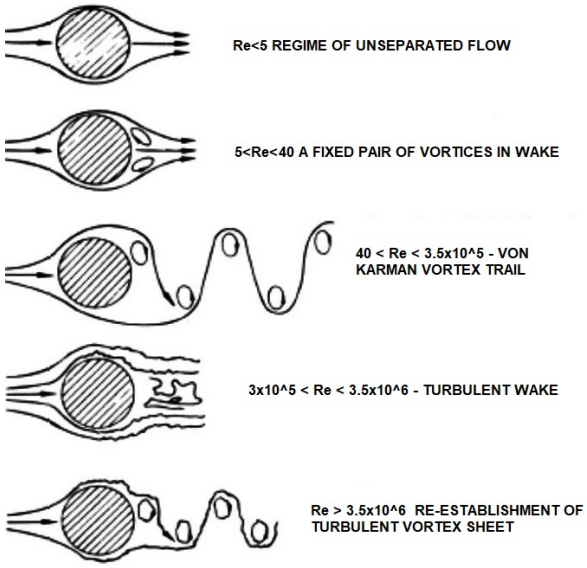

Figure 5.11: Regimes of fluid flow across a smooth tube [74]

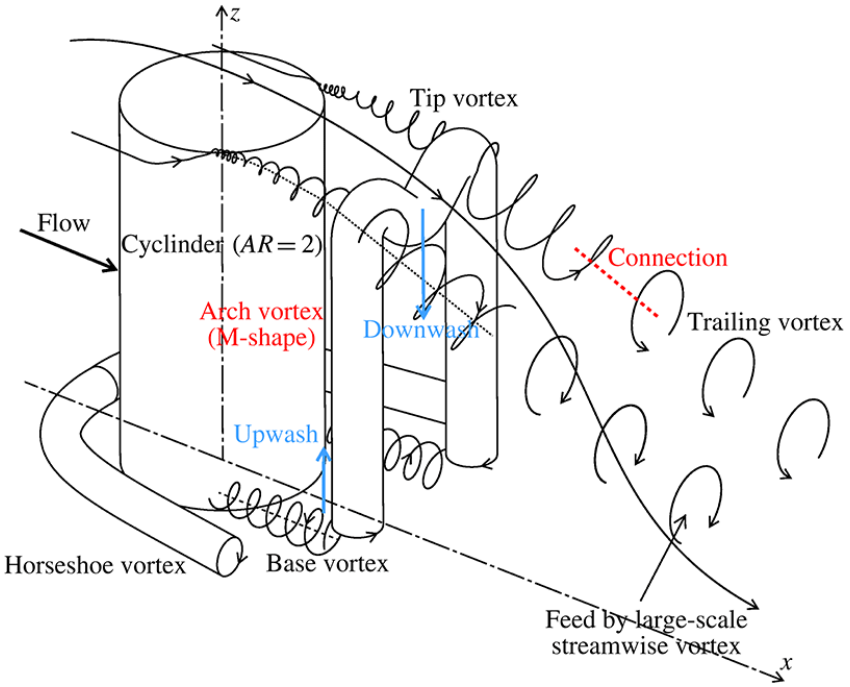

Figure 5.12: 3D wake structures for flow over a wall-mounted short cylinder [75]

The pressure coefficients shows us the stagnation point on the front view and how the flow accelerates on the sides of the tower while the rear view displays another stagnation point and two blue zones where the air accelerate due to the tip vortices. Also on the top of the top we can see two recirculation zones.
From the previous picture we can see not only the vortices that arises from the top and the bottom of the tower but also the down wash and up wash effects.

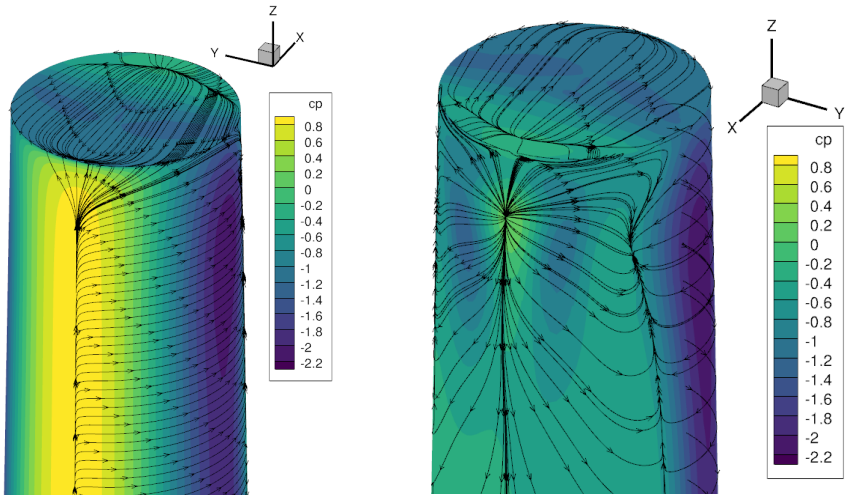

(a) Front view (b) Rear view

Figure 5.13: Pressure coefficient and flow visualization on the TOP of the TOWER

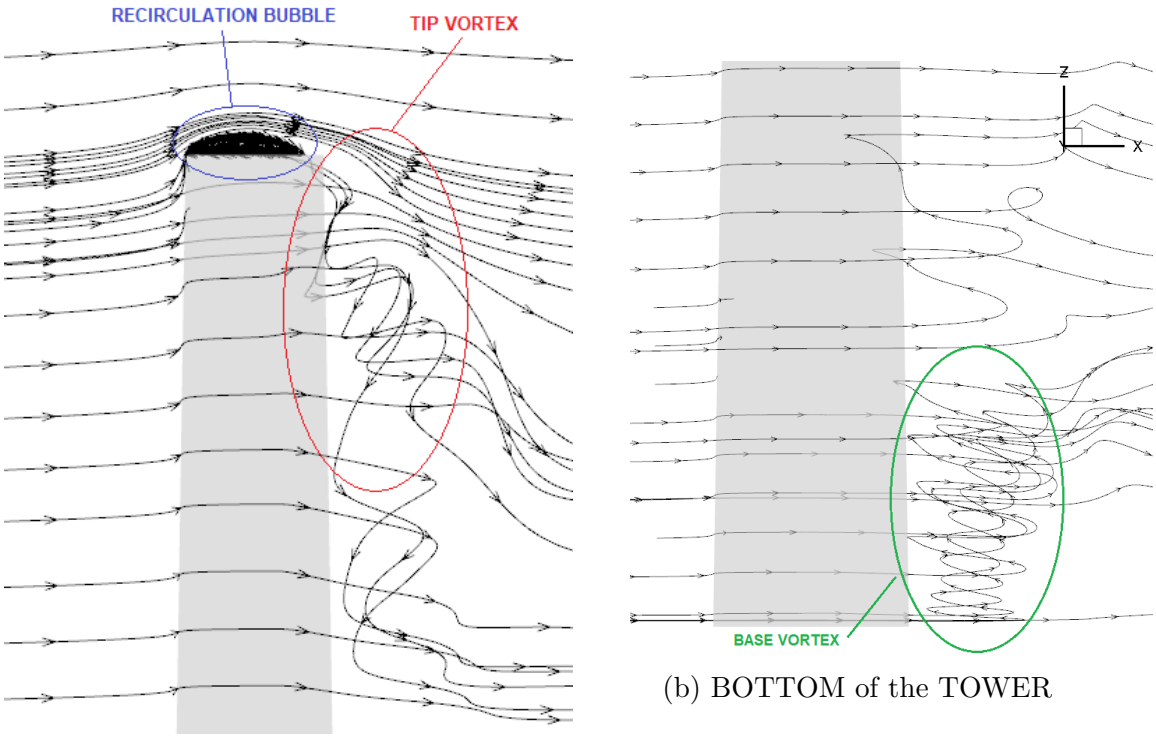

(a) TOP of the TOWER (b) BOTTOM of the TOWER

Figure 5.14: Side view streamlines

On the other side from the top view by visualizing the streamlines at different height (Figures 5.15) we can see how the vortices are not on the same side but switch from one side to the other.
The last Figure (5.16) resume what explained until now and give a sight on the vortex structure by catching the iso-surfaces of a certain values by using the Lambda2 method.

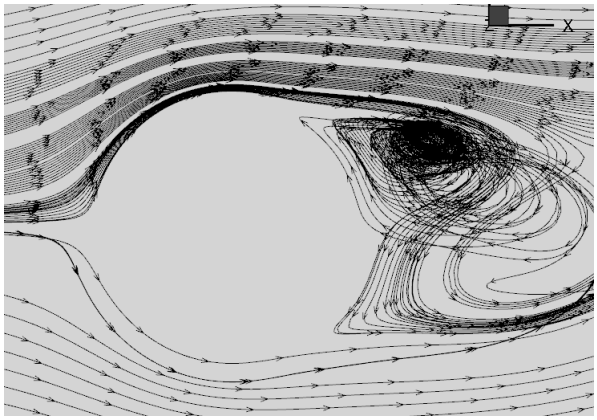

(a) TOP tower section at z=25m

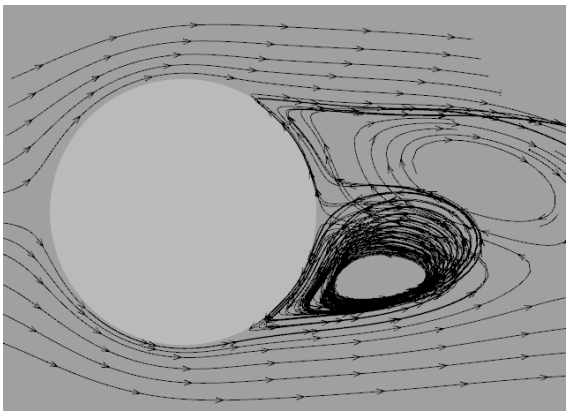

(b) TOP tower section at z=35m

Figure 5.15: TOP tower section at z=35m

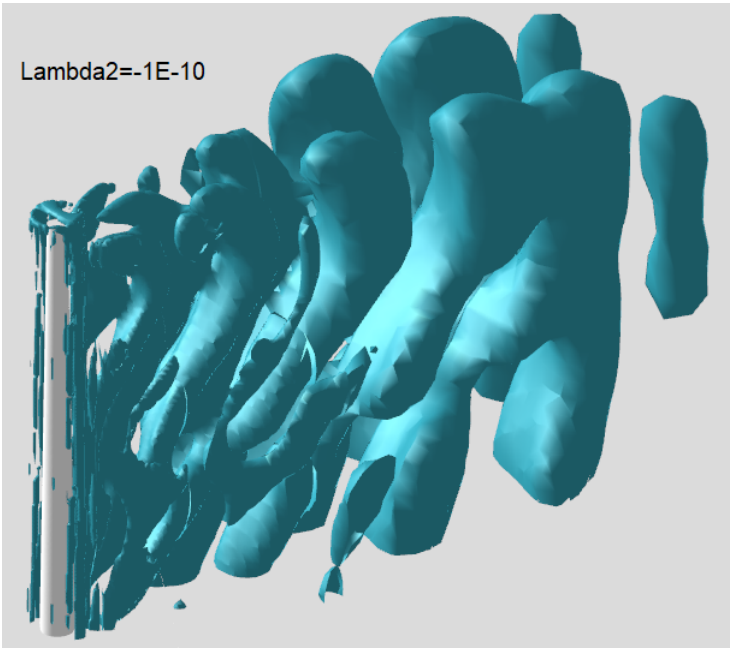

Figure 5.16: Vortex core structures detected by the lambda2 criterion

After have examined the fluid dynamic behaviour around the tower it's time to quantify the forces acting along it and at different sections.

Before presenting (next page) and commenting the results is important to understand that the SECTIONAL LOADS represents a force per unit length along the tower height and are therefore not sensitive to the distances between the sections of the modelled beam.
The "drag" (Fx) of the tower behave like the one of an infinite cylinder close to the bottom and the values decrease moving towards the top because the cross section shrink.
Close to the top the so called tip vortices increment the drag as they for example do on the aircraft's wings.

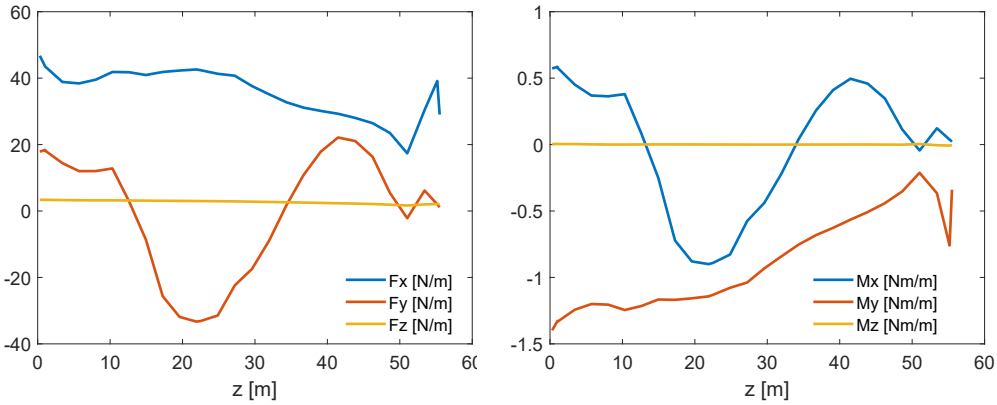

(a) Forces (b) Moments

Figure 5.17: Sectional loads along the tower

The force along the y-direction oscillates across the 0 value because the flow is unsymmetrical due to the vortex shedding.
The forces along the height of the tower are close to zero and the moments reflect the nature of the forces since they are computed starting from those one for local reference system.

The SECTIONAL LOADS gave a great overview but can't be easily implemented into the FEM code for the structural analysis and the solution was to compute forces and moments on sections along the tower that corresponds with the nodes of our FEM model (INTEGRATED SECTIONAL LOADS).

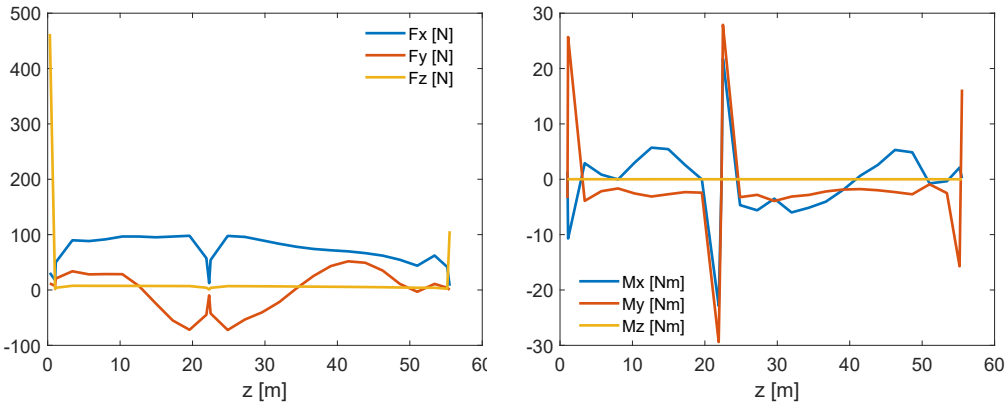

(a) Forces (b) Moments

Figure 5.18: Integrated sectional loads along the tower

Rather than the SECTIONAL LOADS, the INTEGRATED SECTIONAL LOADS are difficult to be interpreted because they represents the integrated value of forces and moments across a section but depend on the distances between the nodes of our beam model.

Before moving to the structural response of the tower a last comment to the global loads is necessary.

Fx	1.6929492e+03
Fy	1.1154125e+02
Fz	7.0796337e+02
Mx	-5.5223034e+03
My	1.6929492e+03
Mz	2.2885258e-02

Table 5.7: Global tower loads

In order to validate the results of the CFD analysis in the literature can be found a lot of experimental results for an infinite cylinder.

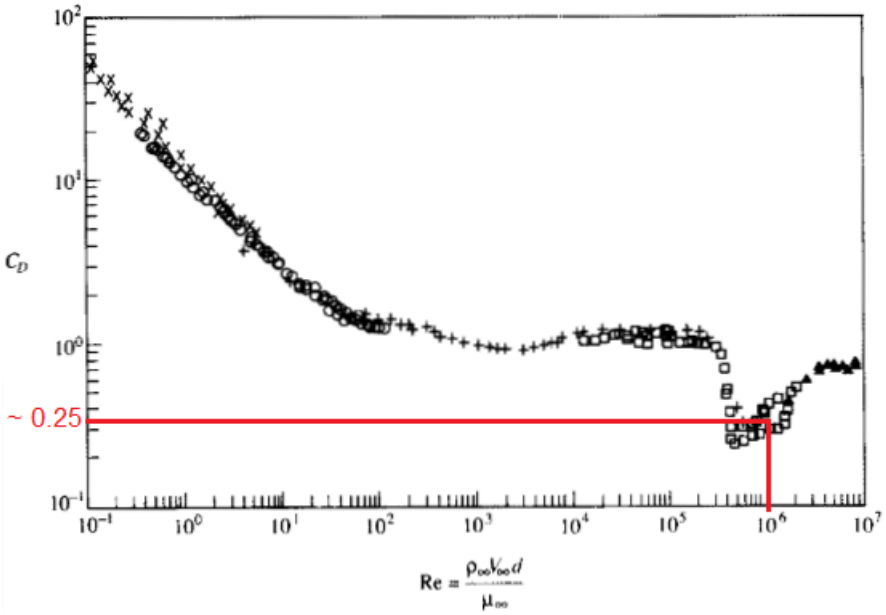

Figure 5.19: Variation of cylinder drag coefficient with Reynolds number [76]

The drag coefficient calculated from the line load of the tower is:

$$C_D = \frac{F_x}{0.5\ \rho\ V^2 \cdot c_{REF}} = 0.489 \tag{5.3}$$

where $c_{REF} = 3.35m$ is the mean chord.

The crag coefficient is slightly bigger than the one from the theory because we are dealing with a finite cylinder with a free tip.

5.2.3 Structural response

Once we have the solution of the flow around the tower and moreover the forces and the moments acting on it, we can go a step ahead and calculate the deformation on the structure.
In order to do that the FEM model of the tower has been created with the feature listed in the next section and the analysis with different configuration has been made.

FEM settings

The FEM software used is the open source code KRATOS Multiphysics and the simulation has been developed using this settings:

Code	Kratos Multiphysics
Beam model	Euler-Bernoulli
Beam element	3D2N
Nodes	31
Constitutive relation	Isotropic linear elastic material
Structural data interpolation scheme	backward
Analysis type	linear static

Table 5.8: FEM settings for the TOWER

In order to check and guarantee convergence to the simulation a residual criterion has been applied to the Newton-Raphson method.

Solver type	non linear
Convergence criterion	residual criterion
displacement relative tolerance	0.0001
displacement absolute tolerance	1e-9
residual relative tolerance	0.0001
residual absolute tolerance	1e-9
max iteration	100

Table 5.9: Convergence criterion settings for the TOWER

Results

Since the tower itself needs to be very stiff, we expect small displacements and rotations.
In the next table only the tip tower values for many configurations are presented since the other results along the height of the tower are very small and less useful for our goal.

Analysis configuration	Results type	x-axis	y-axis	z-axis
Aero + CG	Tip displ. [m]	0.000437607	6.71107e-05	-0.000175189
Aero + CG	Tip rot. [rad]	-1.69648e-06	1.11331e-05	-2.55039e-12
Only aero	Tip displ. [m]	0.000437609	6.71109e-05	7.83573e-08
Only aero	Tip rot. [rad]	-1.69649e-06	1.11332e-05	-2.55039e-12

Table 5.10: FEM results for the tower

As expected the values are very small and therefore no coupling simulation have been made since the tower itself is no much sensitive to the aerodynamic loads at this wind speed.
Comparing the results from the two cases (with and without gravitational forces) we can see how the gravitational force only affect the displacement along the z-axis since the tower is axis symmetric along this directions.
In more detail we can see how the z-displacement changes its sign and module and that give us an idea of the mass and therefore the influence of the tower structure on its structural behaviour.
The last observation regards the lateral forces and moments acting on the tower.
We expect that the tower doesn't deform in the lateral direction and rotate along the x-axis but due to the unsymmetrical behaviour of the turbulent flow and the vortex shedding there are small forces and moments components.

5.3 One way coupling blade

In the last chapter we have deeply studied the aerodynamic around a tower and in this one we will definitely deal with the blade and the whole wind turbine.
We are going to study the aerodynamic around a single blade using a 120° model and then the flow around the whole wind turbine with a full model.

5.3.1 Analysis of structural data

In the previous chapter we have defined our structural model comparing the eigen-frequencies obtained from our FEM model with the one given by the project.
The same process has been performed for the blade but instead of comparing only the different interpolation schemes, also the mesh sensitivity of the modal shapes has been checked.

Three different meshes have been used and the basic idea is that the refined mesh was created by halving the spacing between to coarse grid points.

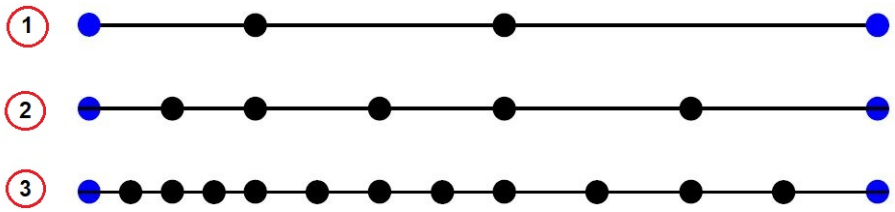

Figure 5.20: Mesh refinement criterion

The mass and structural properties itself have been discretized by calculating the mean value between the starting nodal values (linear interpolation):

$$f_{element_i} = \frac{f_{node_i} + f_{node_{i+1}}}{2} \tag{5.4}$$

Before presenting the results is necessary to appoint that this process of refinement is of the second order.
For the blade the first 3 bending modes have been calculated (2 flap wise and 1 edge wise).
In the next page's table the total relative error calculated through equation 5.2 is presented:

Method	Nodes	$\epsilon_{rel_{TOT}}[\%]$
backward	23	9.87
backward	45	6.72
backward	89	5.48
centered	23	5.42
centered	45	4.70
centered	89	4.52
forward	23	2.43
forward	45	3.05
forward	89	3.65

Table 5.11: Eigenfrequencies BLADE analysis

We can conclude that the forward method with 23 nodes (blue line)better represents the blade in the meaning of the total relative error.
For our FEM analysis the same method with 89 nodes (red line) has been used since the better mesh the more accurate results are obtained.

5.3.2 Analysis conditions

Before describing the mesh settings for both CFD models is important to set the test conditions under which our analysis are going to be carried out.
In order to analyse the aerodynamic and structural response of the blade under different conditions, two set of inlet velocities and RPM are implemented.
The first combinations represents the wind turbine in a low power generation condition:

Wind speed	6.1 m/s
RPM	12.3 rounds/minute
Blade tip velocity	50 m/s
Pitch angle	-0.15°
Tilt angle	5°
Reference length [MAC]	2.02 m
Density	1.231 kg/m^3
Dynamic viscosity	1.789E-05 $N \cdot s/m^2$
Reynolds number	8.48E+05

Table 5.12: First simulation settings for the turbine

The second condition represents a mean power generation situation and permits also a different analysis of the forces and moments acting on the wind turbine.

Wind speed	9 m/s
RPM	17.83 rounds/minute
Blade tip velocity	72.45 m/s
Pitch angle	-1.2°
Tilt angle	5°
Reference length [MAC]	2.02 m
Density	1.231 kg/m^3
Dynamic viscosity	1.789E-05 $N \cdot s/m^2$
Reynolds number	1.25E+06

Table 5.13: Second simulation settings for the turbine

Both settings will be applied on the 1/3 rotor model and on the full wind turbine simulation with a $TILT\ ANGLE = 5°$.

5.3.3 Single blade CFD model

Because of the 3-bladed rotor's rotational periodicity, a rotor sector of 120 degrees is considered for the first simulation.
Thus, only one blade and one-third of nacelle/hub are modelled where the full rotor aerodynamics are taken into consideration by periodic constraints.

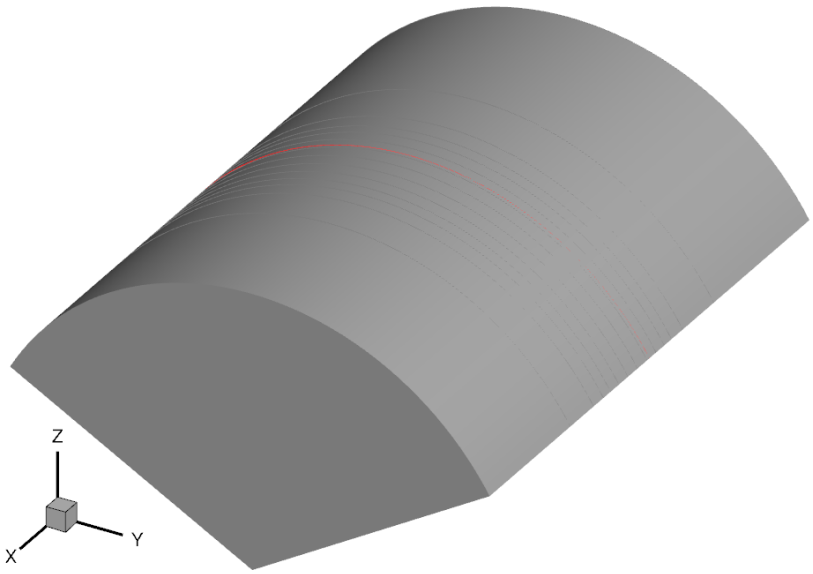

Figure 5.21: CFD computational domain [77]

As for the tower, also here the overall structured grid is composed by many single meshes that are overlapped using the CHIMERA technique.

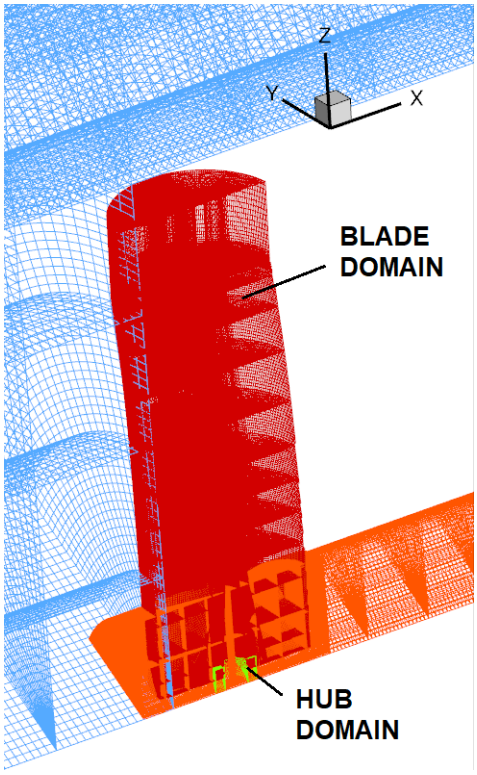

Figure 5.22: 1/3 model CFD mesh [77]

For the mesh of the blade the following parameters have been set:

Direction	Number of cells
Chord-wise	300
Span-wise	100
Boundary layer	35
y+	≈ 1
Boundary condition on the surface	No-Slip Wall
Number of cells	8814592

Table 5.14: Mesh settings for the Blade

For the HUB a mesh with 131072 cells have been created while for the background these values have been taken:

Height of the domain	$10 \cdot$ *Rotor diameter*
Length of the domain	$20 \cdot$ *Rotor diameter*
Minimum spacing (CHIMERA region)	0.25 m
Growth rate	1.17
Boundary condition on the surface	Far-field
Number of cells	16931840

Table 5.15: Mesh settings for the 1/3 model background

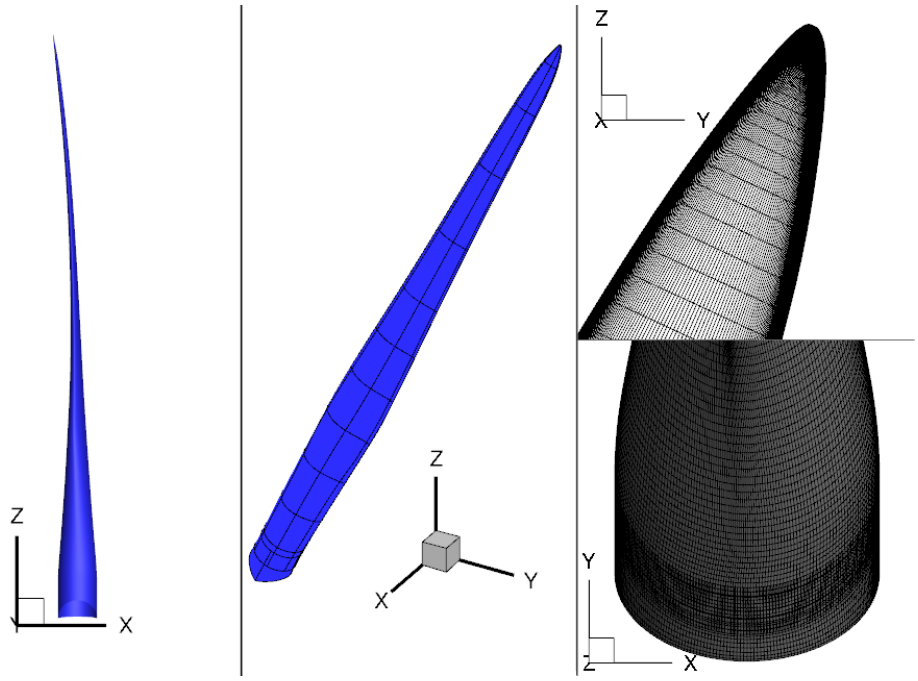

Figure 5.23: Blade mesh [77]

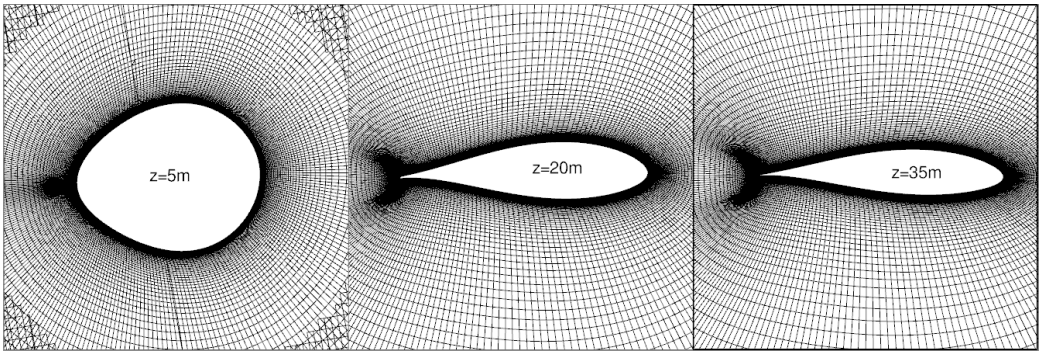

Figure 5.24: Airfoil mesh at different blade sections [77]

5.3.4 Single blade CFD settings and results

The CFD settings are the same as the one used for the tower since we are trying to capture as much details as possible from the flow region.
On the other hand, at this stage we have used the same strategy but with different physical timestep.
The focus in this simulation is on the rotating blade of the wind turbine and because of this the decision is to achieve at the end an accuracy of 1 as physical time.
For this reason the following strategy has been adopted to converge towards the simulation:

Figure 5.25: Solution strategy for the simulation at $rpm = 12.3$

Figure 5.26: Solution strategy for the simulation at $rpm = 17.83$

Through this strategy a converged solution has been achieved with 24 revolutions:

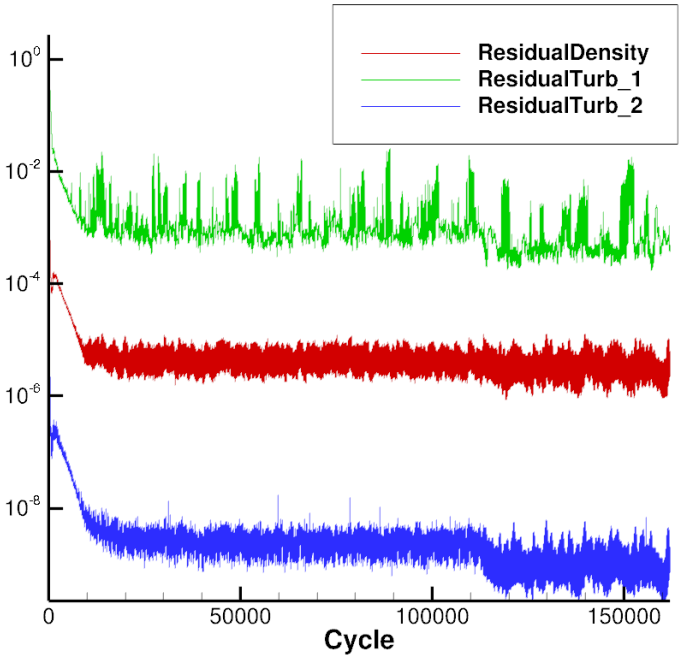

Figure 5.27: Residuals for the simulation at $rpm = 12.3$

The forces coefficients acting on the blade looks like:

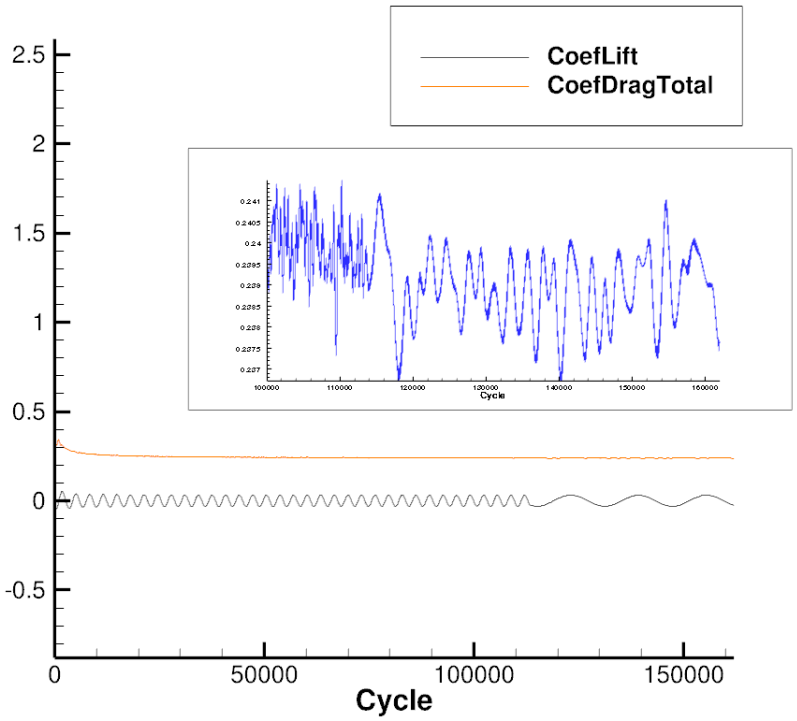

Figure 5.28: Forces coefficients for the simulation at $rpm = 12.3$

Forces and moments acting on the blade in different directions and on different sections will be investigated further when the results from different configurations are going to be compared.
In order to understand how the flow passes around the blade some CFD analysis tools have been used.

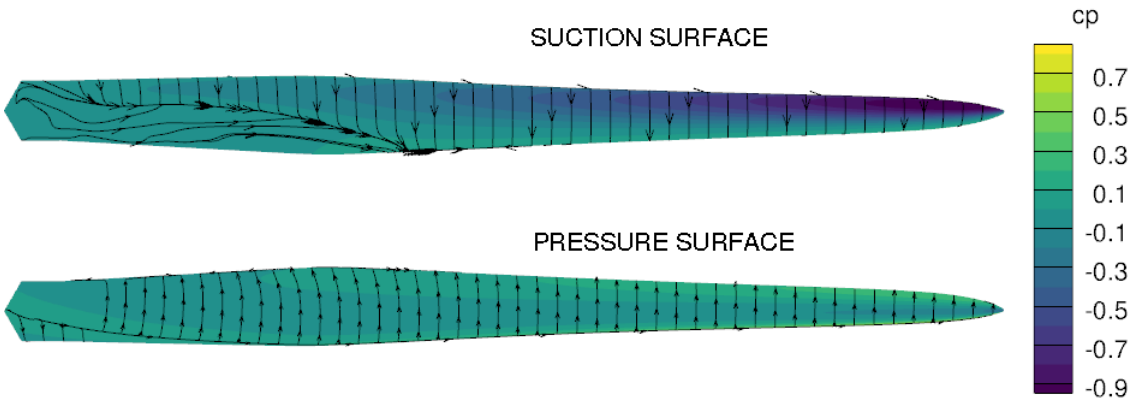

Figure 5.29: Pressure coefficients contour and streamlines over the blade

From the pressure coefficients we can see how the flow accelerates on the suction side mostly on the half of the blade closer to the tip due to the rotational velocity component.

By looking the streamlines on the suction surface is interesting to see how the flow close to the root follows different paths before joining the main direction.
Another observation is that along the leading and trailing edge the streamlines are directed towards the outside of the rotor because of the centrifugal forces.
The last image that is worth to see is the one reporting the vortex core regions around the blade:

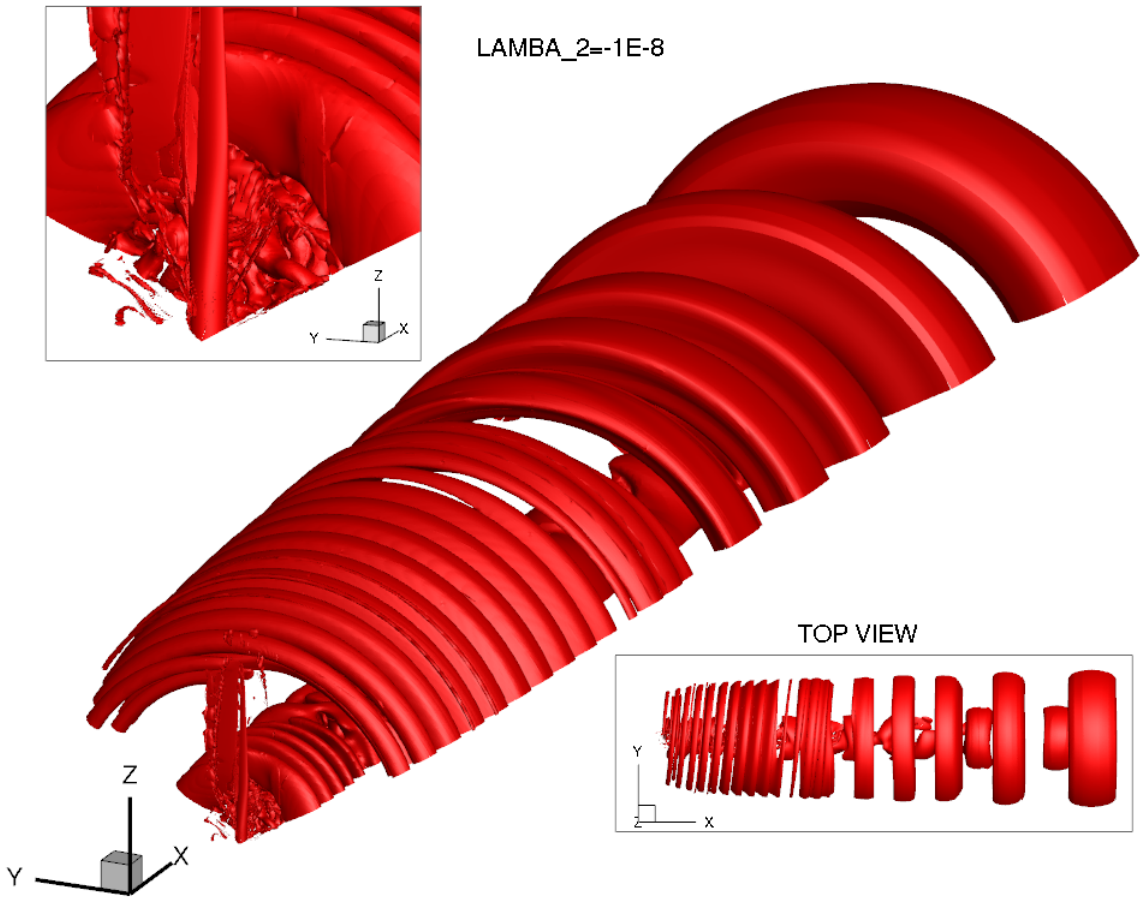

Figure 5.30: Vortex core structures around the blade

From the main and the top view we can recognise the vortex generated by the tip of the blade. This kind of vortices start on a diagonal direction and became perpendicular to the flow direction along the wake.
The tip vortices also dissipate their energy along the make dividing themself in smaller one that increase the overall size of the vortex region.
On the left side of the top a focus on the inner part of the blade is made.
This is done because some smaller turbulent structures are also generated in the zone and explain what we have seen before on the root region from the streamlines plot.

5.3.5 Full wind turbine CFD model

In order to better understand the interaction between the tower and the blade and between the blades, a full CFD model have been developed [77].
This full model permits to consider also the ground effect and the tilt angle and is a composition of the mesh of the tower and the one from the 1/3 model repeated for each of the tree blades.
It was necessary to connect this parts through the nacelle that has been modelled as a cylinder and whose mesh looks like:

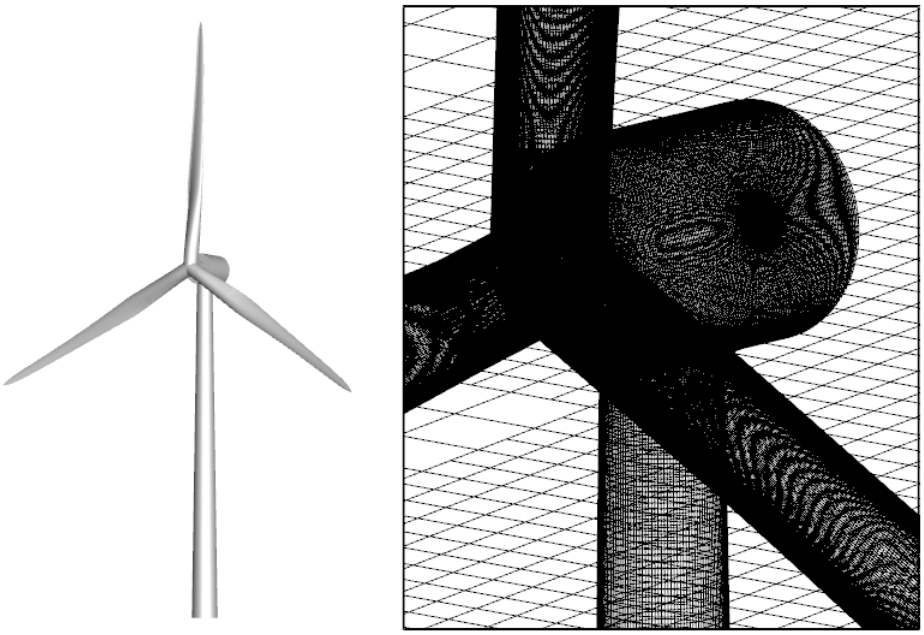

Figure 5.31: Full model wind turbine, nacelle and hub mesh

Another important aspect of the CFD model is the new background whose properties are:

Height of the domain	$12 \cdot$ *Rotor diameter*
Length of the domain	$24 \cdot$ *Rotor diameter*
Width of the domain	$24 \cdot$ *Rotor diameter*
Minimum spacing (CHIMERA region)	0.25 m
Growth rate	1.17
Boundary condition on the surface	Far-field
Number of cells	58894336

Table 5.16: Mesh settings for the full model background

Let's give a closer look at some CFD results.

5.3.6 Full wind turbine CFD settings and results

For this kind of simulation the same CFD settings and solution strategy has been used because for the future aeroelastic analysis the coupling between FEM and CFD code will happen every single degree during the revolution.

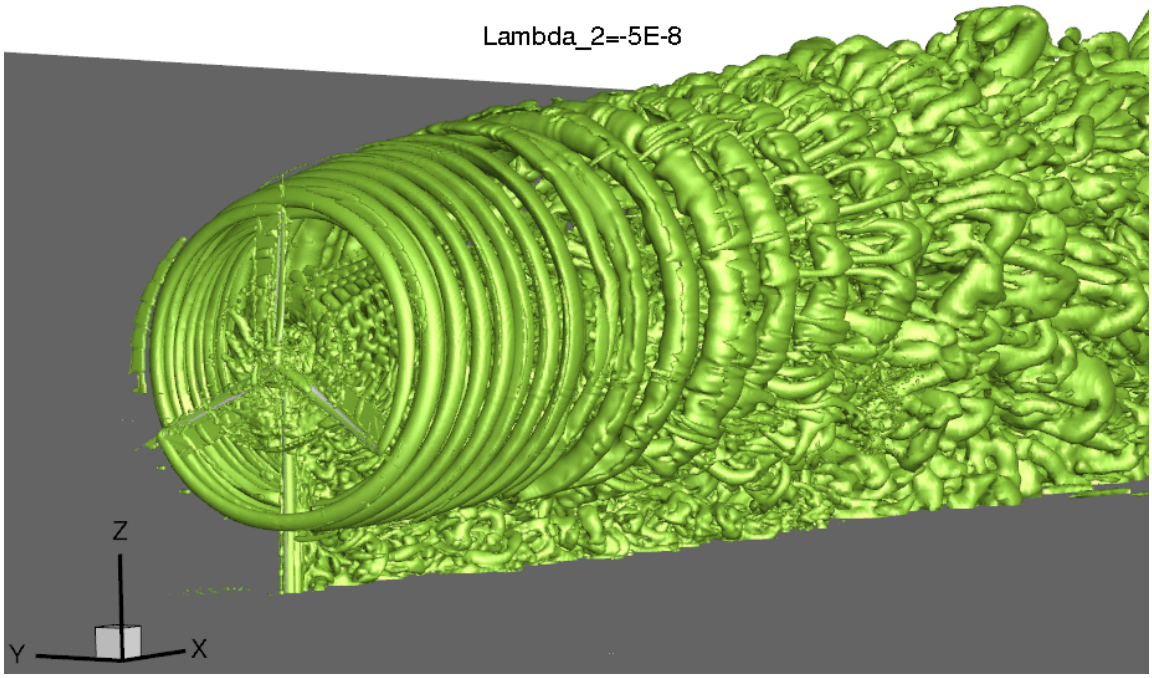

Figure 5.32: Full model wind turbine vortex surfaces

As we did for the 1/3 model, we have analysed the flow around the whole wind turbine through the $lambda_2$ criterion.
By thinking about what it was discovered in the simulations of every single element of the wind turbine, we can imagine that the result could be a superposition of the different flow fields.
From the image above the different turbulent structures are not easy to recognise.
The tip vortex generated by the blades are present until a certain length after the turbine while the vortex shedding from the tower mixed itself with other structures since its birth.
In the end the result is a complex flow filed governed by the vorticity generated from the rotor and the wake of the tower.

5.3.7 CFD results comparison

As before mentioned this subsection has the aim to allow not only the analysis of the load on the blade itself but also to set them side by side in order to better understand relations and differences.

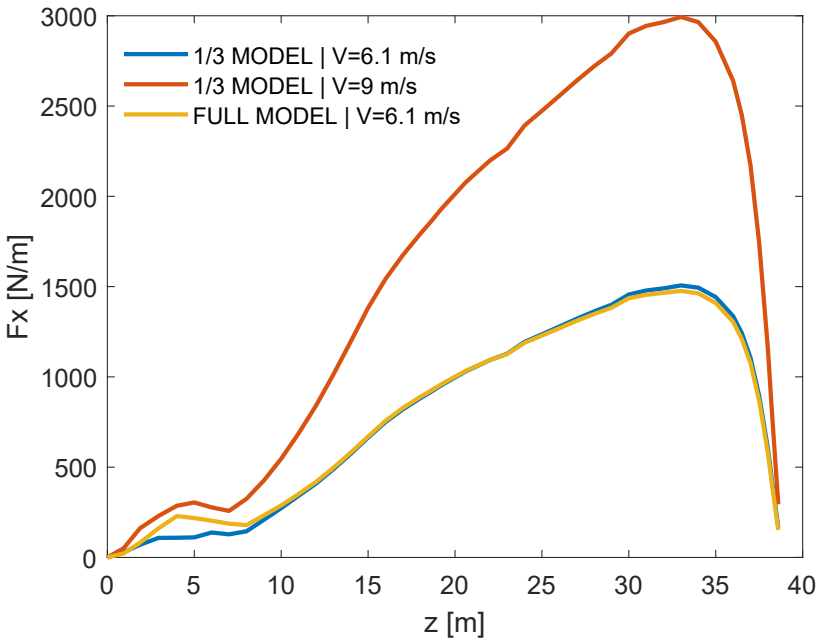

Figure 5.33: Sectional loads along the x-axis from different simulations

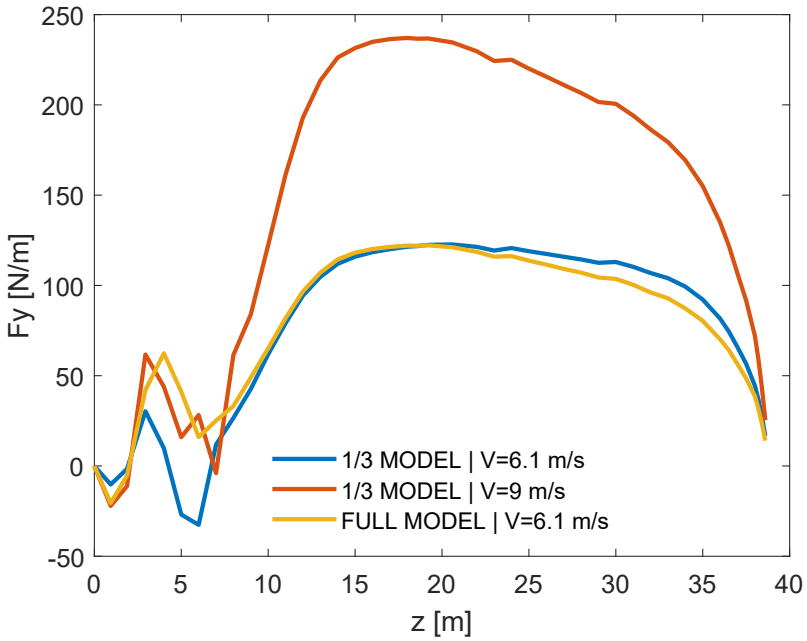

Figure 5.34: Sectional loads along the y-axis from different simulations

First of all we just look at the shapes of the curves inside the plots.
Along the x-direction (flow direction), Fx represents the force that deform the blade against the pre-bend and is not responsible for the power generations.
Fx increases quite linearly from the root until a point where close to the tip the flow restore the same pressure between the sides of the blade.
Instead, Fy is the force that produce power since it acts in the edge-wise directions. This force has a maximum in the center of the blade where the most of the power is generated while on the root the flow is slow, turbulent and arrange itself in vortex structures.

By comparing the forces from two different configurations (V=6.1 m/s and V=9 m/s) of the wind turbine is clear to see the difference between the loads.
On the other side by relating the 1/3 model with the full model on the same configurations (V=6.1 m/s) small differences can bee seen.
The full model presents forces that are generally higher close to the root and lower in the vicinity of the tip.
This can be addressed to the tilt angle, the presence of the tower and the ground effect.
Generally we expect to get less power from the full model rather than from the single blade model because Fy far from the root is smaller then the one from the 1/3 model.

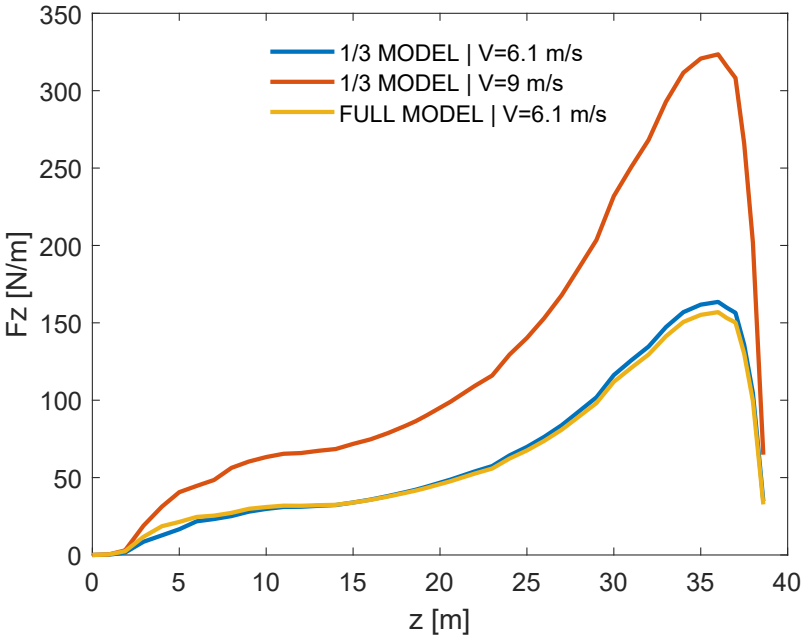

Figure 5.35: Sectional loads along the z-axis from different simulations

The forces along the span of the blade Fz are small compared to the others and are therefore not reported and only close to the tip the vortex sheets play an important role and increase significantly the loads.

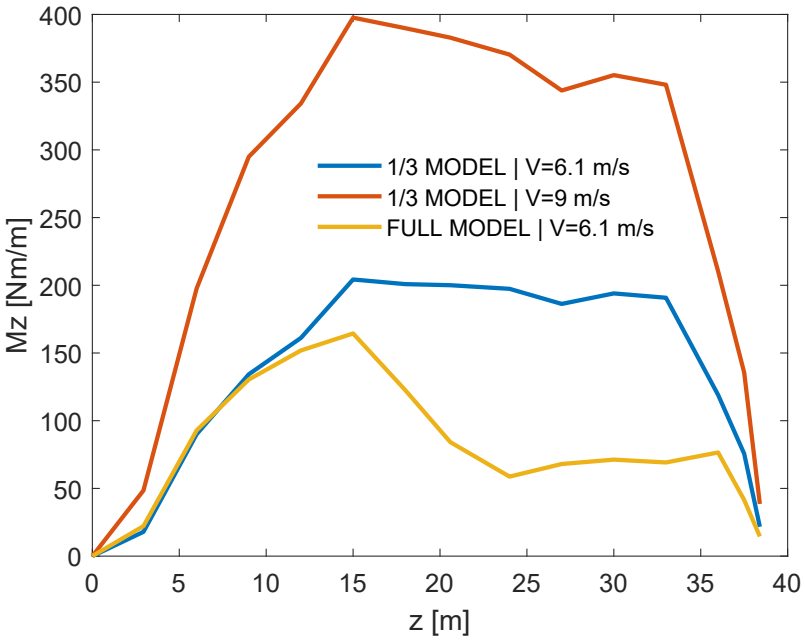

Figure 5.36: Sectional moments around the z-axis from different simulations

The moment around the z-axis is positive along the span and forces the angle of attack of the blade to a smaller value then the starting one.
In this case there is a big difference not only between different configurations but on the second half of the blade the full model shows lower moments then the 1/3 model because of the effect of the other blades and of the tower.
Before moving to the structural analysis the power generated by each configuration in different simulations are presented:

CFD model	Configuration	Power [MW]
1/3 model	$V = 6,1m/s$	0.3
Full model	$V = 6,1m/s$	0.29
1/3 model	$V = 9m/s$	1

Table 5.17: Power generation for each simulation

5.3.8 Structural response (1/3 model)

As done previously for the tower, we are going to apply the CFD computed loads on the FEM beam model of the blade.

FEM settings

Let's start with a description of the settings in Kratos.

Code	Kratos Multiphysics
Beam model	Euler-Bernoulli
Beam element	3D2N
Nodes	89
Constitutive relation	Isotropic linear elastic material
Structural data interpolation scheme	forward
Analysis type	linear static

Table 5.18: FEM settings for the TOWER

The converge criterion for the non linear solver are the same used for the tower structure analysis.

Results

The displacements of the blade have been computed for both boundary conditions and with many combinations between aerodynamic loads (FLOWer), gravitational forces (GF) and centrifugal forces (CF).

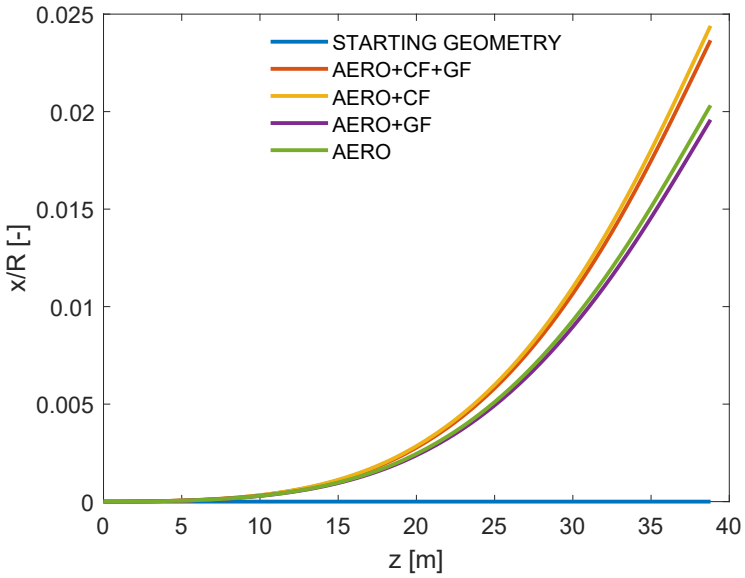

Figure 5.37: Normalized flap-wise displacement of the blade for V=6.1 m/s

We can see that in the flapwise direction when the blade is at $Azimuth = 0°$ the aerodynamic loads have a huge impact deforming the tip of about $4,5\%$ of the radius.

It is important to underline that in those graphs the blue line (STARTING GEOMETRY) represents a reference line from which the relative displacements are computed and not the actual geometry of the blade. On the other side it is necessary to remember that the blade has a pre bend on the flap-wise direction.
The GF doesn't make a great difference while the effect of the centrifugal force is that it acts against the pre-bend.

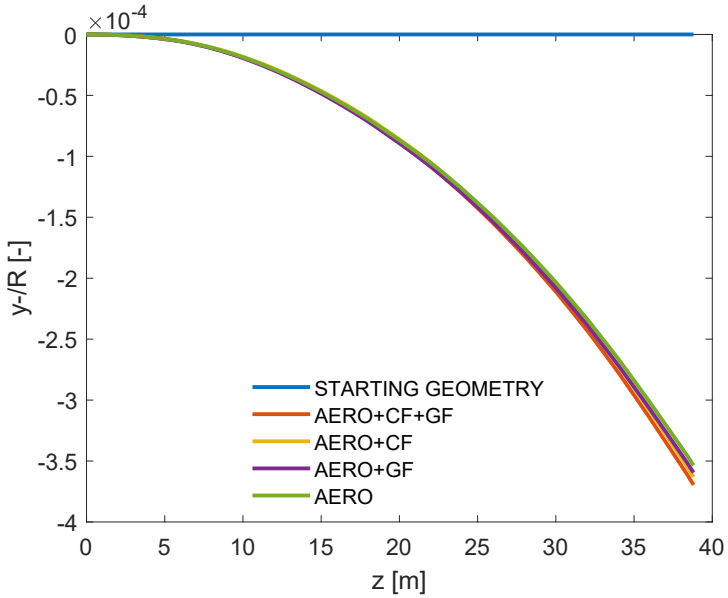

Figure 5.38: Normalized edge-wise displacement of the blade for V=6.1 m/s

Along the edgewise direction only the aerodynamic loads deform the blade in an important way while the other components don't make that much difference.

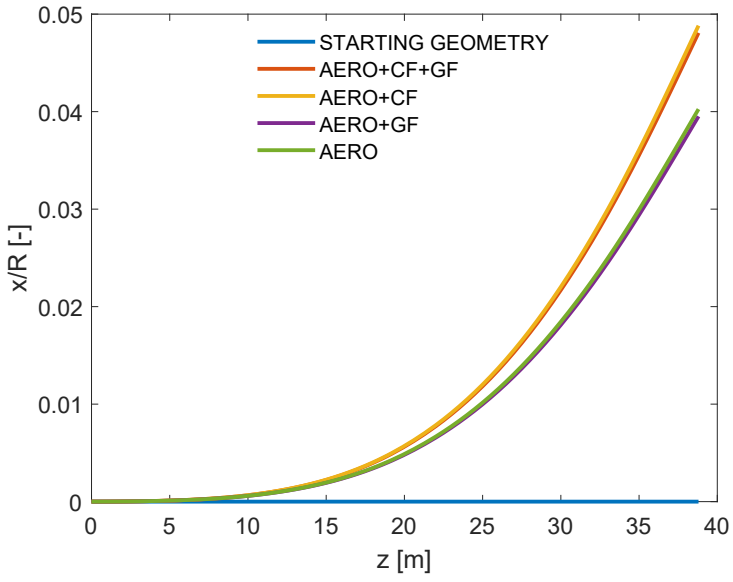

Figure 5.39: Normalized flap-wise displacement of the blade for V=9 m/s

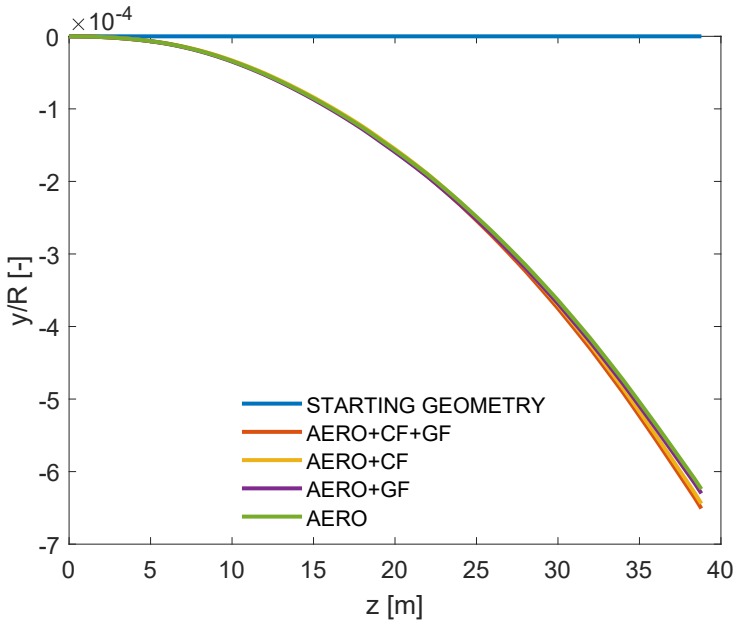

Figure 5.40: Normalized edge-wise displacement of the blade for V=9 m/s

For the second step of boundary conditions, in both directions the blade deforms more.

5.4 Two way coupling (1/3 model)

The last and the most important part of this chapter regards the TWO WAY COUPLING where an apposite software has been used in order to iteratively connect the CFD code (FLOWer) with the FEM code (Kratos).

5.4.1 Settings

The purpose of the two way coupling is to exchange loads and deformations between the codes in order to perform an analysis where in the CFD code the shape of the blade is at every TIME STEP the one obtained at the end of the previous structural dynamic computation.
On the other side the FEM code calculates the deformations at every TIME STEP with the actualised and modified loads on the structure.
The software needed for this exchange operations is EMPIRE and the data transfer happens every 1° during the revolution for a total of 3 revolutions.

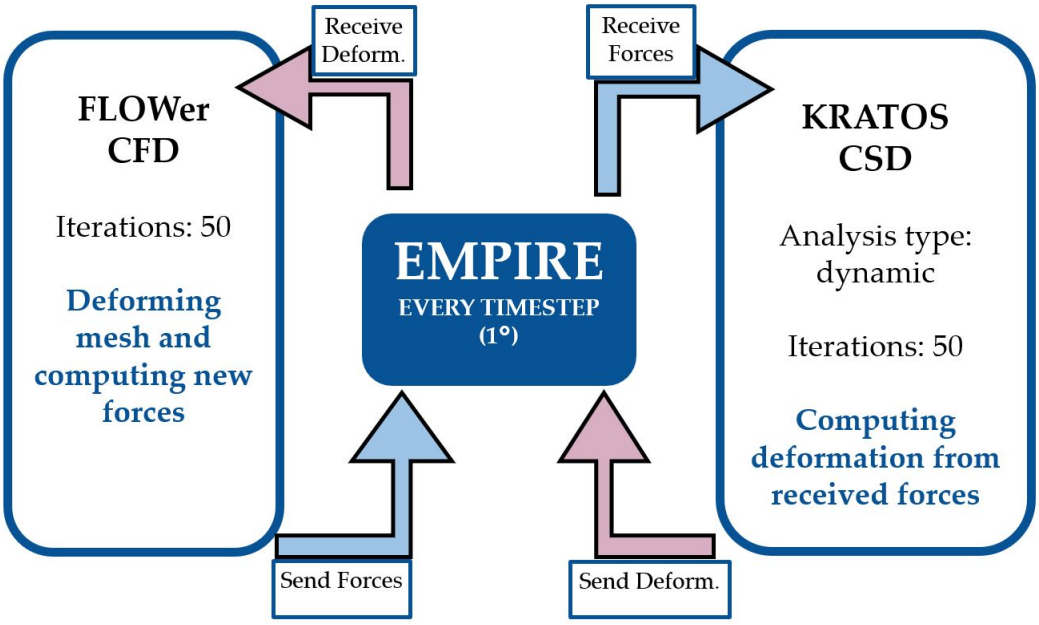

Figure 5.41: FLOWer-Empire-Kratos explicit coupling

For FLOWer the settings remain the same as for the previous simulations while for Kratos here the following changes have been made:

Analysis type	linear dynamic
Damping method	Rayleigh
Numerical method	implicit

Table 5.19: FEM settings for TWO WAY coupling of the blade

5.4.2 Results

The aim of this section is to evaluate the mutual influence between structural deformation and aerodynamic behaviour around the blade.
In order to do that the before explained aeroelastic study has been performed and the explicit coupled simulation has been stopped when the tip displacement, the forces and the residuals doesn't change in time (TIME STEP).
We have seen that after 3 revolutions both simulation have reached convergence.
We will first start this results analysis by looking at the tip displacement of the blade in time.
We have performed two analysis for each boundary condition, one taking into account all the forces and another only with the aerodynamic loads.

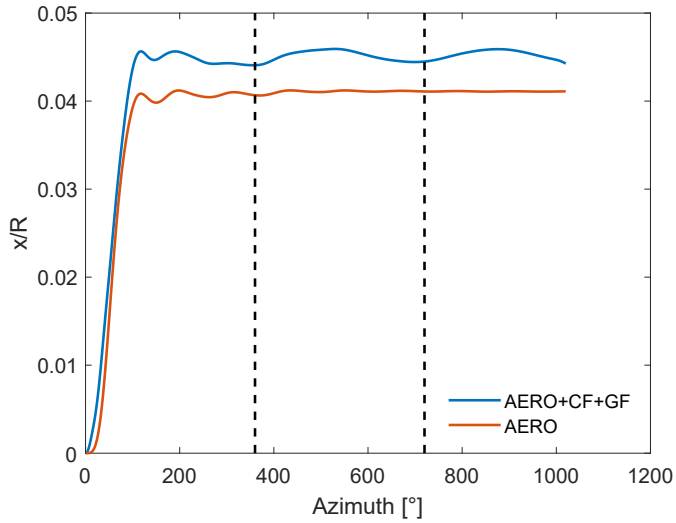

Figure 5.42: Normalized flap-wise tip displacement/coupled analysis at V=6.1 m/s

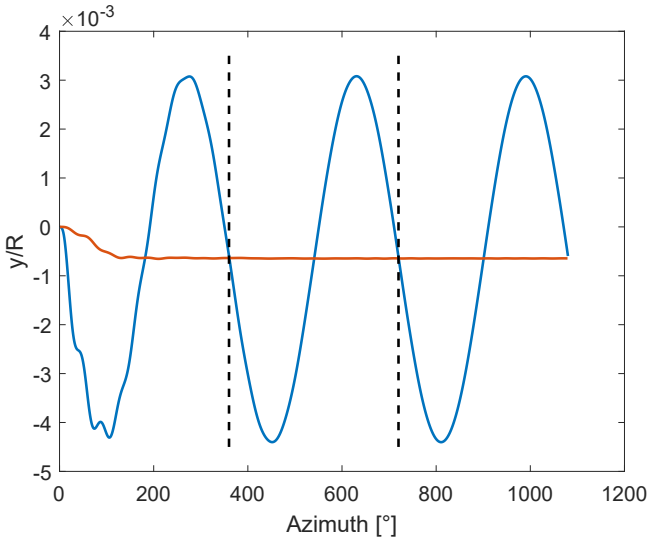

Figure 5.43: Normalized edge-wise tip displacement/coupled analysis at V=6.1 m/s

In both direction it can been stated that after the first revolution both configurations achieve a steady state.
In the case where all forces are considered there is for the flap and edgewise motion an oscillating behaviour due to the periodical change of the direction of the gravitational force relative to the blade.
In the flapwise motion the difference between the displacements of the two curves is generated by the centrifugal force that can't be neglected for our purposes.

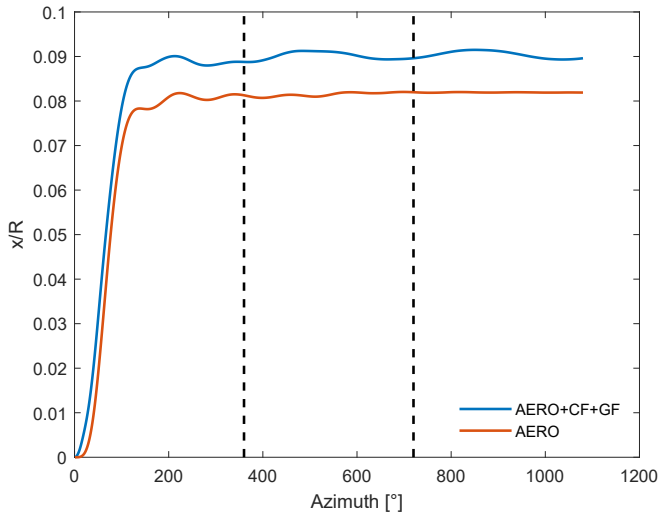

Figure 5.44: Normalized flap-wise tip displacement/coupled analysis at V=9 m/s

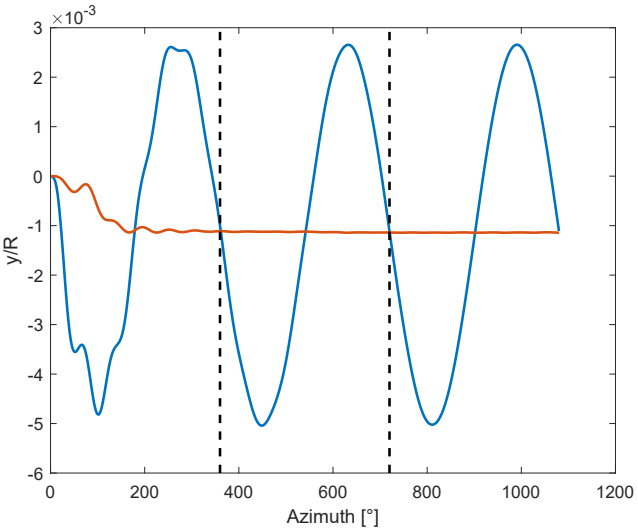

Figure 5.45: Normalized edge-wise tip displacement/coupled analysis at V=9 m/s

The same behaviour can be seen for the case of a faster inflow condition.

The second stage of the coupled analysis is to compare the deformation of the blade between the one way and the two way coupling.

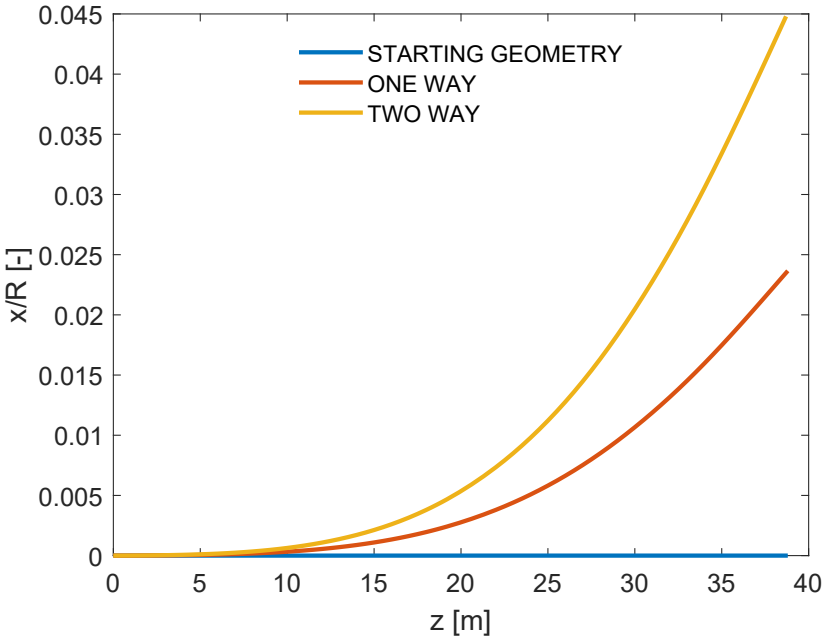

Figure 5.46: Comparison of flap-wise displacement along the span for V=6.1 m/s

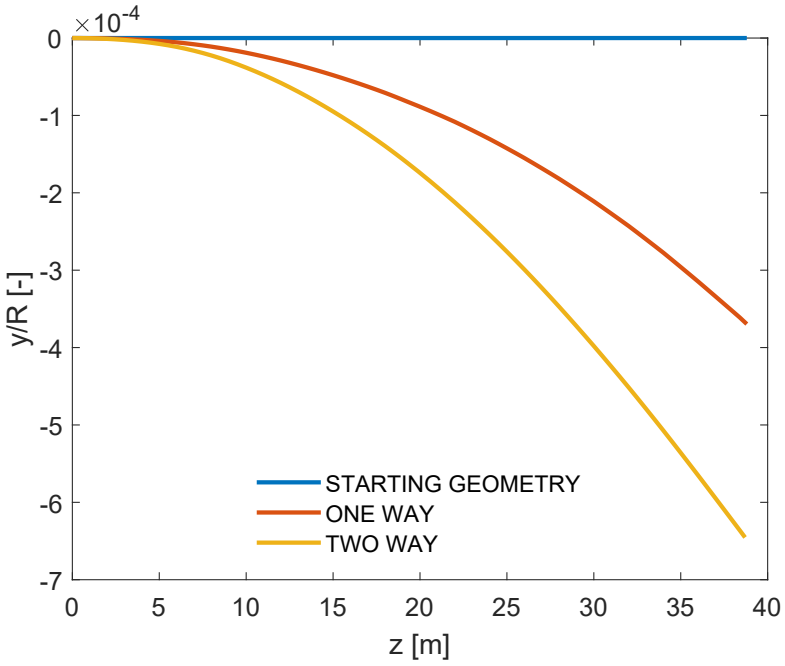

Figure 5.47: Comparison of edge-wise displacement along the span for V=6.1 m/s

In both plots a big difference between one way and two way coupling can be seen. The same amplified behaviour is characteristic also for the other boundary condition.

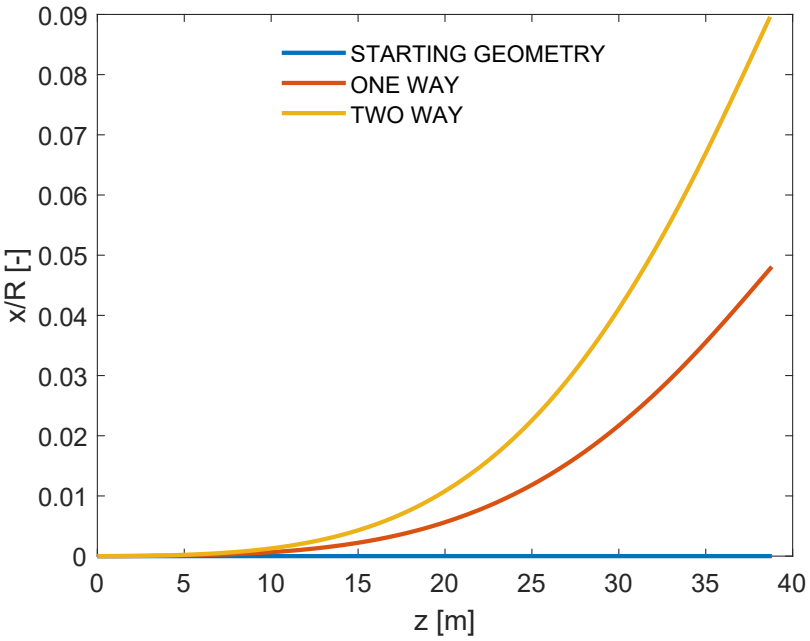

Figure 5.48: Comparison of flap-wise displacement along the span for V=9 m/s

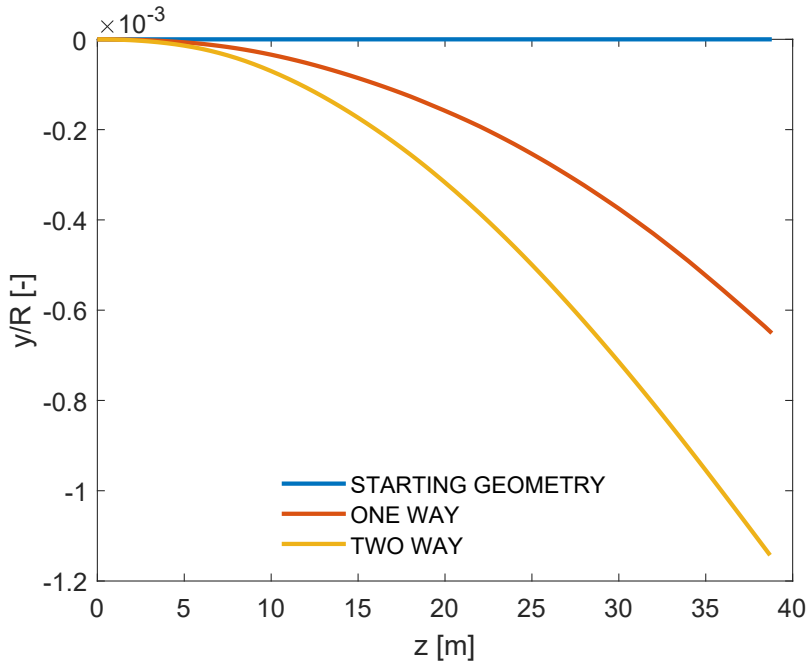

Figure 5.49: Comparison of edge-wise displacement along the span for V=9 m/s

It is now interesting to investigate why there is this difference among the two coupling methods.
We will focus on the slow velocity case but the following results are also valid for the other test case.
A deep insight in how the forces changes in time while the structure is deforming can give a first answer to the question.

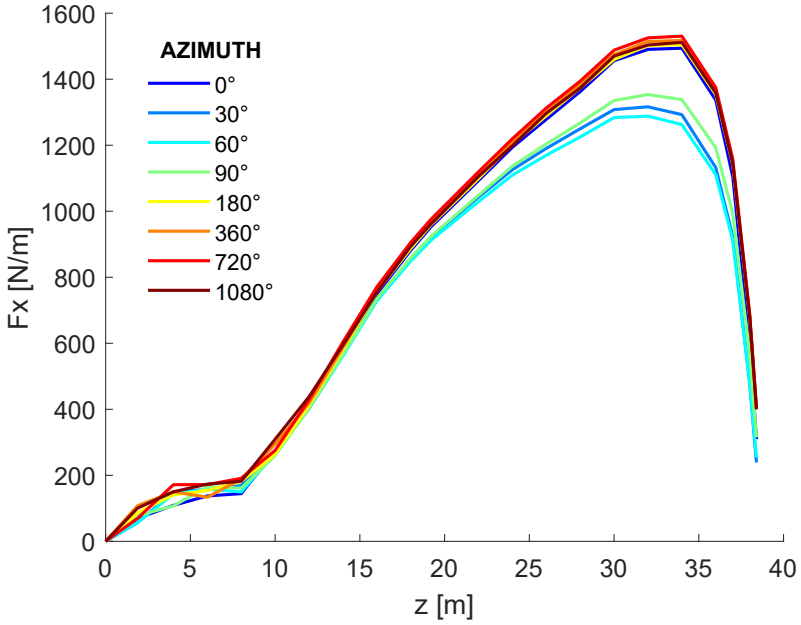

Figure 5.50: Sectional loads in the flap-wise direction in time

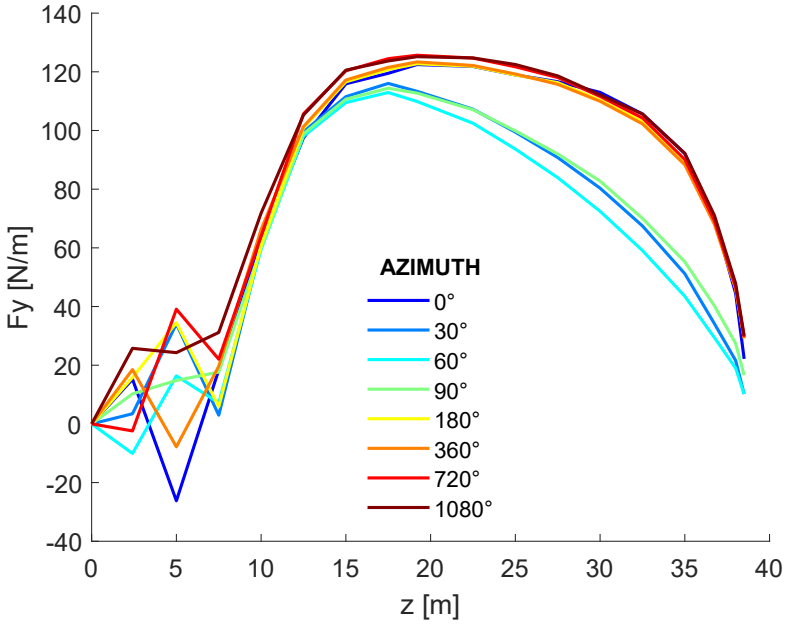

Figure 5.51: Sectional loads in the edgewise direction in time

The graphs give a very interesting information about how the forces change during the 3 revolutions.
At the beginning the blade is moving with the same direction of the wind speed and therefore Fx is smaller and also Fy is smaller along the span because the angle of attack decreases. After a while the situation changes in the opposite direction and only after the first revolution the forces find a steady state.

Now is important to know if there is a difference between the mean value of the last revolution in the case of the rigid or flexible blade (one way or two way coupling).

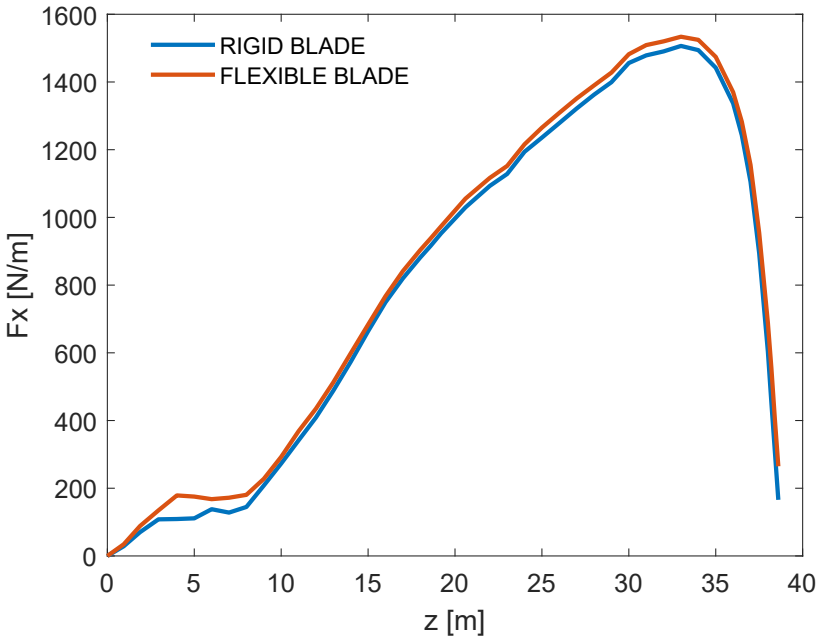

Figure 5.52: Mean values of the forces in the flap-wise direction along the span

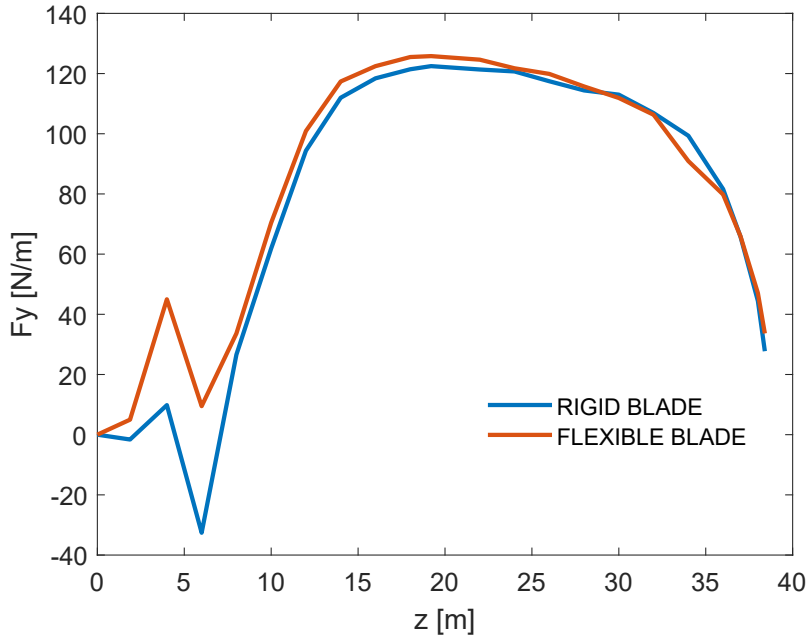

Figure 5.53: Mean values of the forces in the edge-wise direction along the span

Both forces are slightly bigger for the two way coupling and that give us a first reason for having in a state steady bigger deflections for the flexible blade.

Another important detail in order to justify the difference between the study cases is the length of the beam and how it changes while the blade deforms.
Actually there are 3 effects that changes the length of the blade:

- **pre-bend**: the blade is deforming against the pre-bend and therefore when the absolute value of this angle is smaller than the beginning one the beam model stretch itself along the span-wise direction This geometrical effect is taken into account in our linear structural analysis because the pre-bend changes the normal direction to the surface along which the blade deforms.
- **Centrifugal force** acts along the span-wise direction and as a consequence stretch the blade with positive displacement values
- **Aerodynamic force** has also an influence and is present along the z-axis in our reference frame (span-wise direction)

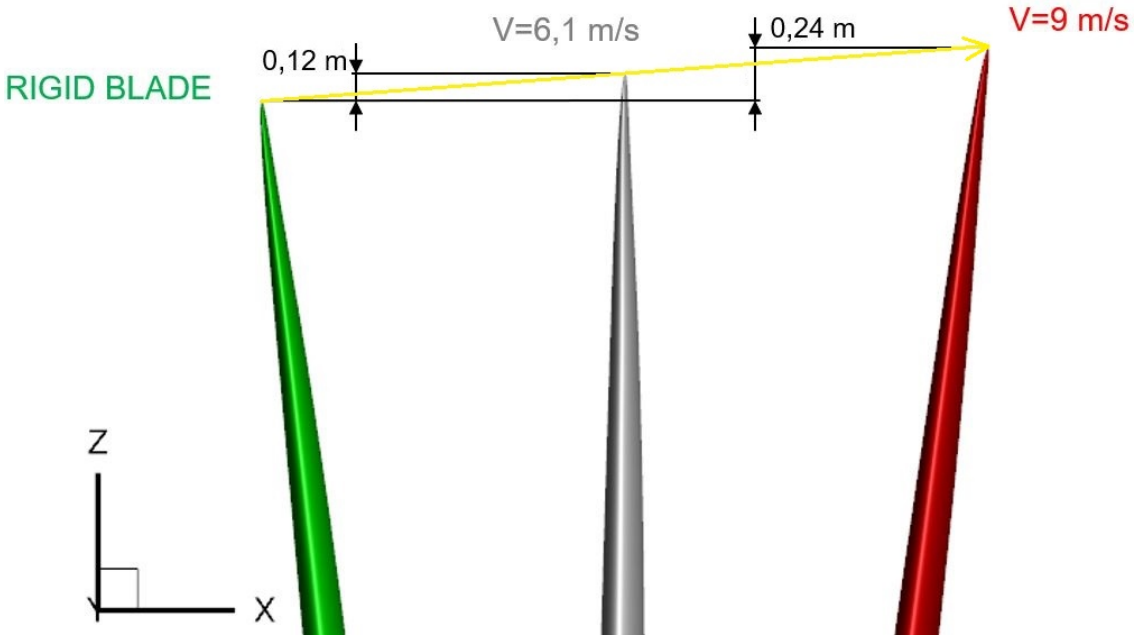

Figure 5.54: Linear analysis - blade tip displacements comparison

The figure 5.55 give us some confirmation and important information.
The first one is that, as mentioned before, the structural linear analysis has displaced the tip of the blade along the normal direction to the surface and therefore the length of the blade has increased linearly for both simulated configurations.
The second one is that the loads acting on our beam model have had a small influence on the changes in the length of the beam and the geometrical effect dominates.
The last and most important comment is that for the two way coupling big forces act on a big surface having as consequence a large deformation.

At the end of this thesis was possible to run a **dynamic non linear simulation** of the 1/3 model of the blade at the LOW SPEED boundary condition and by considering only the aerodynamic loads.
The results are presented in the next figure and allow to do important considerations.

Figure 5.55: Linear/non linear analysis - blade tip displacements comparison

On the flap-wise direction the non linear analysis give smaller displacement due to the increased values in the stiffness matrix.
A lower flap-wise deformation for the non linear analysis is also the consequence of a smaller increase in the length of the blade when compared with the linear one.
In fact by considering the geometrical non linearities we have taken into account the change in the length of the beam in the z-axis due to the pre-bend.

Thereafter we can compare the effect of the pre-bend computed by the non linear simulation with the one calculated analytically:

Reference position	Non linear simulation [m]	Analytical analysis [m]	Relative difference [%]
Blade tip	0.0573	0.055	4.2

Table 5.20: z-axis displacement comparison due to the pre bend

There is a very small relative difference between the results and we can conclude that the geometrical non linear simulation has produced accurate results and allows to include in our analysis the change in the shape and length of the beam caused by the pre bend.
On the other side the results proposed in Table 5.20 suggest that for the deformation along the span of the blade the geometrical effect dominates above the loads.

FFT analysis

In order to prove the stability of the wind turbine an **FFT (Fast Fourier Transformation)** has been made on the forces in the flap- and edge-wise direction. This analysis permits to discover if there is a coupling between the eigenfrequencies of the blade and the forces acting on it.

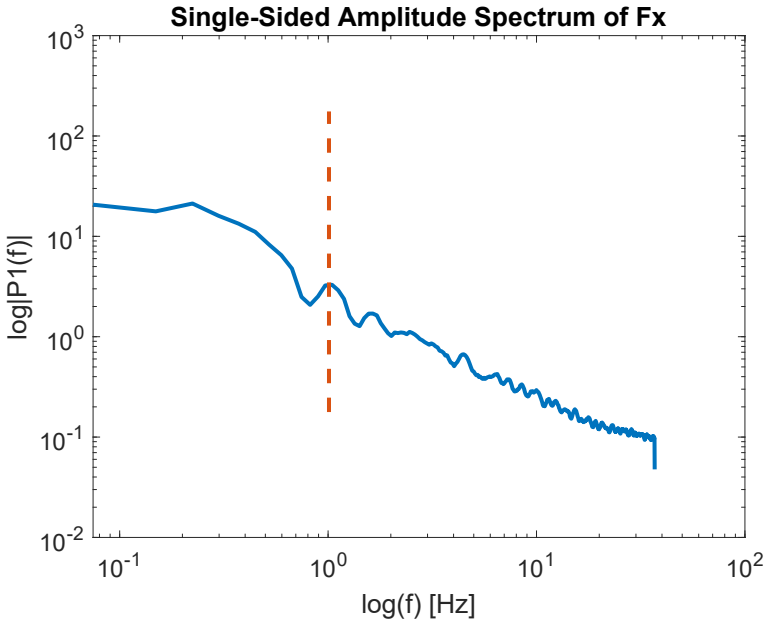

Figure 5.56: FFT analysis along the flap-wise direction

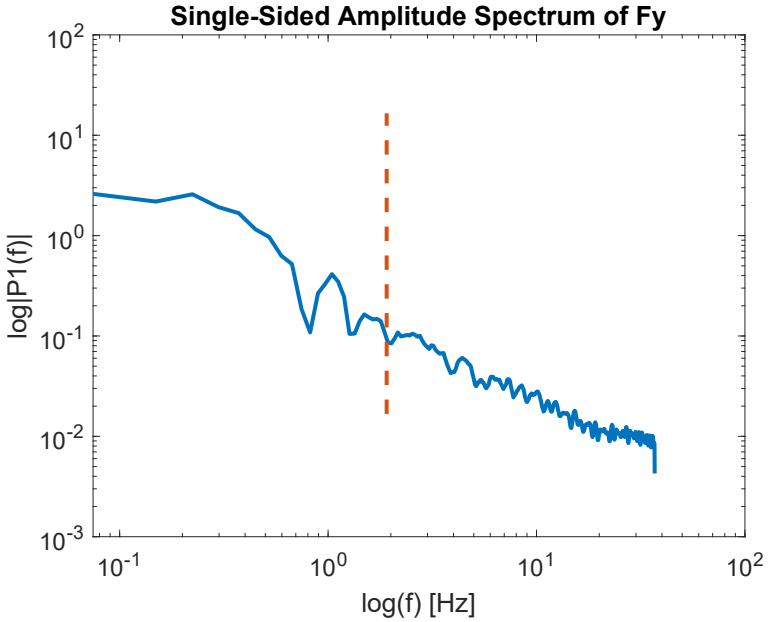

Figure 5.57: FFT analysis along the edge-wise direction

The excitation frequencies are below the eigenfrequencies (orange dashed line) and therefore the blade is stable under an aeroelastic point of view in both configurations.

Generated power

The last thing we are going to analyse is also the most relevant for a wind turbine, the generated power. As mentioned before the wind rotor is rotated through the force in the y-direction, the span-wise one. As we have seen before, the force in the case of the flexible blade is greater than the rigid one so for both boundary conditions we expect more power generated in the two way coupling.

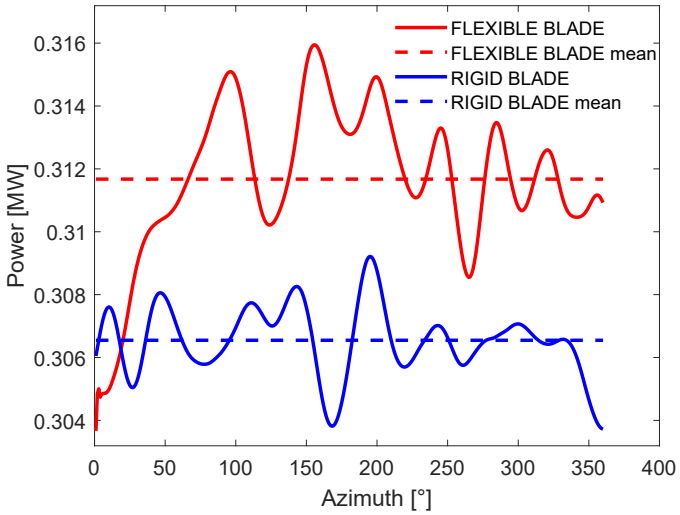

Figure 5.58: Power generation comparison for V=6.1 m/s

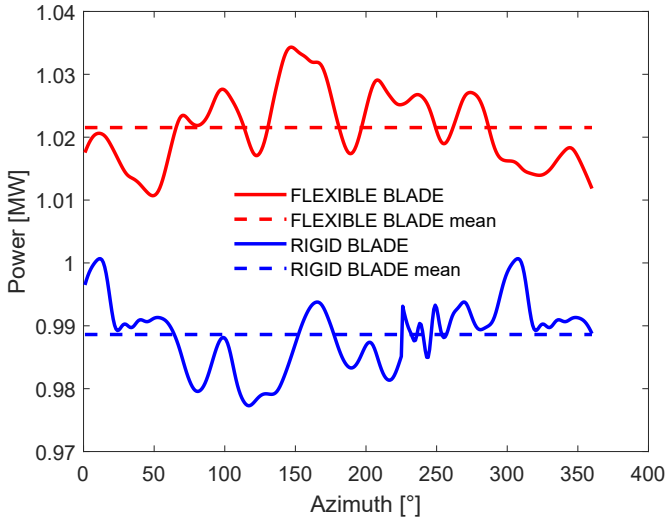

Figure 5.59: Power generation comparison for V=9 m/s

As expected for both cases there is a little increment in the power generation for the flexible blade in the order of the 5/10 kW.

Chapter 6

Conclusions and Outlook

The main goals of this thesis have been fulfilled.
The first obtained result was to get in touch with the open source FEM based code Kratos Multi-physics, validate it and set it up in order to give reasonable and comparable results for the one way and two way coupling.
Kratos has allowed also to run a structural dynamic analysis with the possibility to choose many integration methods and a structural damping matrix.
In the end was possible to run and achieve convergence for all structural simulation.
Another important aspect of this work was to analyse how the data received from the project could be interpolated and adapted to many grid points in order to achieve closer eigenfrequencies to the given one and therefore comparable results in the next steps. Moving to the aeroelastic results, it has been stated that the tower can be modelled as a rigid body since its deformation are in the order of the mm while for the blade a one way coupling methodology is not sufficient.
From the flexible blade analysis (two way coupling) very interesting results has been found because the deformation of the blade changes significantly the loads around it and its surface.
In the end for the CFD analysis considering a flexible blade, bigger forces has been computed along the body and as a consequence more power generated than the rigid case (one way).
By looking at the behaviour of the displacement of the blade tip during the revolutions and the FFT analysis for the acting forces, we can conclude that this wind rotor model is stable from an aeroelastic point of view.

For all the static and dynamic FEM analysis only geometrical linearities has been taken into account but in the end was possible to run a non-linear simulation where smaller flap-wise displacements has been found due to the change in the stiffness matrix and the decrease in the length of the beam.
On the other side an Euler-Bernoulli beam model has been implemented while by computing the shear area through a dedicated software, the Timoshenko model could give more accurate results.
The last outlook regards the possibility to run a two way coupling for the entire wind turbine with 3 flexible blades and see how the blade influence each other, the effect of the tower, the ground and the tilt angle.

Bibliography

[1] Frankfurt School-UNEP Centre/BNEF. Global trends in renewable energy investment 2018. 2018.

[2] GWEC. Global cumulative installed capacity 2001–2016. 2014.

[3] G.Cabrera Dong Energy UK. Nextwind inc. 2017.

[4] LBNL and BNEF.

[5] Inc. 2018 IEA Wind TCP/PWT Communications.

[6] ECN Wind Energy. Final report of iea task 29, mexnext (phase 1): Analysis of mexico wind tunnel measurements. 2012.

[7] ECN Wind Energy. Final report of iea wind task 29 mexnext (phase 3). 2018.

[8] Jason Charles Howison. Aeroelastic analysis of a wind turbine blade using the harmonic balance method. 2015.

[9] J. R. Wright and J. E. Cooper. Introduction to aircraft aeroelasticity and load. 2008.

[10] Prof. Ing. E. Carrera and Ing. M. Petrolo. Ex. 3 - aeroelastic static stability. 2018.

[11] Lin Wang. Nonlinear aeroelastic modelling of large wind turbine composite blades. 2015.

[12] LTI Motion 2019. https://www.lti-motion.com/cn/industry-solutions/wind-energy/pitch-control-systems. 2015.

[13] Madsen H. A. Bjorck A. Enevoldsen Ganander H. Petersen, J. T. and D. Winkelaar. Prediction of dynamic loads and induced vibrations in stall. 1998.

[14] P. Zhang and S. Huang. Review of aeroelasticity for wind turbine: Current status, research focus and future perspectives. 2011.

[15] H. Stiesdal. Extreme wind loads on stall regulated wind turbines. in proceedings of 16th british wind energy association. 1994.

[16] C. Anderson H. Heerkes and R. Yemm. The use of blade-mounted dampers to eliminate edgewise stall vibration. 1999.

[17] Sorensen J. N. Voutsinas S. Sorensen N. Hansen, M. O. L. and H. A. Madsen. State of the art in wind turbine aerodynamics and aeroelasticity. 2006.

[18] S. R. Vatne. Aeroelastic instability and flutter for a 10 mw wind turbine. 2008.

[19] W. Johnson. Dynamics of tilting proprotor aircraft in cruise flight. 1974.

[20] T. Buhl. Parameter variations for active-stall and pitch-regulated turbine, task 6 report. 2005.

[21] K. Thomson J. T. Petersen and H. A. Madsen. Local blade whirl and global rotor whirl interaction. 1998.

[22] M. D. Pavel and T. H. van Holten. A rotor-tower instability associated with the advancing lead/lag mode. 2000.

[23] Athanasios Kolios Lin Wang, Xiongwei Liu. State of the art in the aeroelasticity of wind turbine blades: Aeroelastic modelling. 2016.

[24] the free encyclopedia Wikipedia. Blade element momentum theory. 2019.

[25] Tangler J. Comparison of wind turbine performance prediction and measurement. 1982.

[26] DøssingM GaunaaM, SørensenNN. Prediction of steady aerodynamic performance of rotors with winglets using simple prescribed wake methods. 2011.

[27] LeeI. JeongM-S, YooS-J. Wind turbine aerodynamics prediction using free-wake method in axial flow. 2012.

[28] Chattot J-J. Helicoidal vortex model for wind turbine aeroelastic simulation. 2007.

[29] WJM Rankine. On the mechanical principles of the action of propellers. 1865.

[30] Froude R. On the part played in propulsion by differences of fluid pressure. 1889.

[31] Shen WZ Sørensen JN. Numerical modeling of wind turbine wakes. 2002.

[32] Wind energy handbook. burton. 2015.

[33] Quartapelle L. Numerical solution of the incompressible navier-stokes equations. 2013.

[34] Van Mameren A. Bijl H, VanZuijlen A. Validation of adaptive unstructured hexahedral mesh computations of flow around a wind turbine airfoil. 2005.

[35] Smith DE Byrom TG Huebner KH, Dewhirst DL. The finite element method for engineers. 2008.

[36] Osborne Reynolds. On the dynamical theory of incompressible viscous fluids and the determination of the criterion. 1895.

[37] Kwon OJ. Yu DO. Predicting wind turbine blade loads and aeroelastic response using a coupled cfd–csd method. 2014.

[38] Professor Henryk Stolarski Ariel Dahl. Modeling wind turbine blades for fluid/structure interaction analysis. 2012.

[39] Craig J. Bauchau O. Euler-bernoulli beam theory. structural analysis: with applications to aerospace structures. 2009.

[40] Oñate E. Timoshenko theory. structur alanalysis with the finite element method linear statics: volume 2: beams, plates and shells. 2013.

[41] C. Mergel Roger, A. Sauer. A geometrically exact finite beam element formulation for thin film adhesion and debonding. 2014.

[42] S. Øye. Flex5 user manual. 1999.

[43] Shabana AA. Dynamics of multibody systems. 2013.

[44] A. S. Elliott and A. D. Wright. Adams/wt: an industry-specific interactive modelling interface for wind turbine analysis. 1994.

[45] J. M. Jonkman and M. L. Buhl Jr. Fast user's guide,.

[46] V. A. V. a. S.G.Voutsinas. Gast: A general aerodynamic and structural prediction tool for wind turbines. 1996.

[47] E. Bossanyi. Gh bladed user manual. 2009.

[48] T. Larsen. How 2 hawc2, the user's manual. 2009.

[49] C. Lindenburg. Phatas release'apr-2005'user's manual. 2005.

[50] K. Becker N. Kroll, C.-C. Rossow and F. Thiele. Aerosp. sci. technol. 4, 223–237. 2000.

[51] TU Muenchen Chair of Structural Analysis, Prof. Dr. K.-U. Bletzinger.

[52] CIMNE ©. http://kratos-wiki.cimne.upc.edu/index.php/. 2012.

[53] P.; Thomsen K. Hansen, M.H.; Fuglsang. Aeroelastic modelling of the nm80 turbine with hawc. 2017.

[54] CIMNE ©. https://github.com/kratosmultiphysics/kratos/wiki. 2012.

[55] Miquel Santasusana. Kratos dem, a parallel code for concrete testing simulations using the discrete element method. 2013.

[56] Inc. ©2019 GitHub. https://github.com/kratosmultiphysics/kratos/wiki/overview. 2019.

[57] Marco Petrolo Erasmo Carrera, Gaetano Giunta. Beam structures classical and advanced theories. 2011.

[58] Aashish Ahuja. Corotational formulation for beams. 2015.

[59] Eugenio Oñate Pooyan Dadvand, Riccardo Rossi. An object-oriented environment for developing finite element codes for multi-disciplinary applications. 2010.

[60] https://www.femto.eu/stories/linear-non-linear-analysis-explained/.

[61] https://www.comsol.it/blogs/what-is-geometric-nonlinearity/.

[62] Shambhu P. Dasgupta Indrajit Chowdhury. Computation of rayleigh damping coefficients for large systems.

[63] N.M. Newmark. A method of computation for structural dynamics. 1959.

[64] M. Bossak W.L. Wood and O.C. Zienkiewicz. An alpha modification of newmark's method. 1981.

[65] Prof. Ing. E. Carrera and Ing. M. Petrolo. Ex. 6 - static and free vibration analysis of beams. 2018.

[66] Institut für Aerodynamik und Strömungstechnik Braunschweig F. Le Chuiton. Flower user-guide. 2004.

[67] K. Meister E. Krämer, T. Lutz. Euromech - wind turbine wakes. 2009.

[68] Inc ©Pointwise. https://www.pointwise.com/products/index.html. 2019.

[69] J. L.; DOUGHERTY F. C. BENEK, J.; STEGER. A flexible grid embedding technique with application to the euler equations. 1983.

[70] ©DLR. Flower-2008.1 - installation and user handbook. 2008.

[71] Schmidt W. Jameson, A. and E. Turkel. Numerical solution of the euler equations by finite volume methods using runge-kutta time-stepping schemes. 14th AIAA Fluid and Plasma Dynamic Conference, Palo Alto, Kalifornien, 1984.

[72] G.-S. Jiang and C.-W Shu. Efficient implementation of weighted eno schemes, journal of computational physics, vol. 126, pp. 202–228. 1996.

[73] A. J. Jameson. Time dependent calculation using multigrid, with applications to unsteady flows past airfoils and wings. 1991.

[74] Blevins R. D. Flow induced vibration 2nd ed. 1990.

[75] Hong-Ping Wang Hang-Yu Zhu, Cheng-Yue Wang and Jin-Jun Wang. Tomographic piv investigation on 3d wake structures for flow over a wall-mounted short cylinder. 2017.

[76] Wiley-Interscience. Experimental data from incompressible flow. 1984.

[77] G. Bangga G. Guma, T. Lutz. Aero-elastic analysis of wind turbines in turbulent inflow conditions. 2019.